UTRECHT UNIVERSITY

CO_2 Capture from Steel Gases – using Pressure Swing Adsorption model in Aspen Adsorption™

MASTER THESIS

28 July 2022

Universiteit Utrecht

Saima Wasefi (9943056)

Saima.wasefi@students.uu.nl

Utrecht University
Department of geosciences
Energy Science (Natural Science Track)
Supervisor: Dr. Matteo Gazzani (m.gazzani@uu.nl)
Second reader: Dr. ir. Wina Crijns-Graus (w.h.j.graus@uu.nl)

Tata Steel Nederland
Research and Development
Supervisors:
Güçhan Yapar (Guchan.Yapar@tatasteeleurope.com)
Balan Ramani (B.Ramini@tatasteeleurope.com)

PREFACE

During an intensive period of five months, I researched CO_2 capture with pressure swing adsorption (PSA) from the steel mill gases of Tata steel IJmuiden and wrote my thesis on this. It was a period in which I learned to set up valid and reliable research and evaluate, improve and appreciate my work. I did not do this alone. Therefore, I would like to express my gratitude to the persons who have advised, helped, and supported me during my research. Firstly, I would like to thank my tutor Professor Matteo Gazzani for his invaluable advice and support.

In addition to the help from the university, I would like to sincerely thank the R&D department of Tata steel IJmuiden for providing this exciting and challenging thesis opportunity; their full cooperation with this research and access to all documents was necessary for proper validation of this research. In particular, I would like to thank My two supervisors Guchan Yapar and Balan Ramani, for their weekly help and critical questions, which have helped improve this work. In addition, their compliments gave me the courage to decide that it was time to hand in the thesis. Also, thank you, Peter van den Broeke for his constructive feedback and corrections.

Finally, I would like to thank my husband, Osman, and my family for their emotional support, which provided the necessary boost and motivation to give this research to a successful end. Sharing my findings and setbacks during the research has helped me organise my thoughts better and gain the confidence that I was writing a valuable study. I am very grateful to them for this.

Saima Wasefi

July 2022

ABSTRACT

Industry and Petroleum refineries are among the most significant contributors to anthropogenic CO_2 emissions. Within the industry, the iron and steel industry is the most energy-consuming manufacturing sector. Iron and steel production is still primarily coal-based, thus dependent on fossil fuels responsible for CO_2 emissions. In 2020, the global iron and steel industry has emitted about 2.6 Gt of CO_2, about 8.3% of the world's CO_2 emissions.

Mitigating these total CO_2 emissions while steel production continues to rise is the major challenge for the iron and steel industry. Therefore, carbon capture is essential to enable the use of carbon while reducing CO_2 emissions into the atmosphere. Tata Steel Ijmuiden is exploring various CO_2 capture technologies for their CO_2 emission mitigation, including physical adsorption. As such, this thesis is aimed to establish the benchmark numbers for the performance of a PSA unit capturing CO_2 from a gas mixture of blast furnace gas and basic oxygen furnace gas.

The PSA unit was modelled using aspen adsorption software, where the physical adsorption takes place on selected zeolite 13X particles. The model has been validated with experimental data from the literature and optimised in an extensive parameter study. The system operated between 15bar and 0.1 bar pressure, and the operating temperature was the same as the feed gas temperature, 288 K. To process 24104 kmol of feed gas per hour, 390 trains of two parallel adsorption beds were required with a length of 9 meters and a diameter of 0.75 meters. The PSA system had a specific energy demand of 1,87 GJ per tonne of CO_2 captured for its pressure reduction and increase. Ultimately, 1.9 million tonnes of CO_2 is captured in this system annually, with a recovery rate of 84%. The CO_2 purity, on the other hand, is $94\%_{mols}$.

NOMENCLATURE

Roman symbols

C	Gas phase concentration	kmol m^{-3}
CV	Valve's coefficient	kmol s^{-1} bar^{-1}
d_{bi}	Internal bed diameter	m
D_L	Axial dispersion coefficient	m^2 s^{-1}
D_{mk}	Molecular diffusivity	m^2 s^{-1}
d_p	Particle diameter	m
H_b	Bed height	m
MTC	Mass transfer coefficient	s^{-1}
m_{ads}	Mass of adsorbent/solid	kg
M_w	Molecular weight	kg $kmol^{-1}$
P	Pressure	bar
P_F	Feed gas pressure	bar
$PB\ start$	Bed pressure at the start of the step	bar
$PB\ end$	Bed pressure at the end of the step	bar
$PExt\ start$	External pressure at the start of the step	bar
$PExt\ end$	External pressure at the end of the step	bar
q	The amount adsorbed or Solid loading	mol kg_{ads}^{-1}
R	Ideal gas constant	L atm K^{-1} mol^{-1}
r_p	Particle radius	m
t	Time	s
$Tamb$	Environment temperature	K
T_B	The temperature of the bed	K
T_{feed}	Feed temperature	K
T_g	Gas temperature	K
T_s	Solid temperature	K
$tstep$	Step duration	s
V_B	Volume of the bed	m^3
$Vbulk$	Volume of the bulk	m^3
v_g	Superficial gas velocity	m s^{-1}
W	Working capacity	mol kg_{ads}^{-1}
Y_CO_2	Purity of CO_2 in a gas mixture	%
x	Axial distance coordinate	m

Greek Letters

$\alpha_{i/j}$	Selectivity of component i over component j	
ε_b	Interparticle or bed voidage	-
ε_t	Total voidage	-
ε_p	Intraparticle voidage	-
ΔH	Enthalpy of adsorption	MJ $kmol^{-1}$
ΔP	Pressure drop through the valve	bar
ρ_b	Bed packing density	kg m^{-3}
ρ_g	Gas density	kmol m^{-3}
ρ_p	Particle or solid density	kg m^{-3}

ρ_w	Wall material density	kg m^{-3}
μ_g	Gas mixture viscosity	kg m^{-1} s^{-1}

Acronyms

AC	Activated carbon
ACFs	Activated carbon fibers
BF	Blast furnace
BFG	Blast furnace gas
BOFG	Blast oxygen furnace gas
COG	Coke oven gas
COP	Covalent organic polymers
CMPs	Conjugated microporous polymers
CMS	Carbon Molecular Sieve
CNTs	Carbon nanotubes
CSS	Cyclic Steady State
CTF	Covalent triazine based framework
CV	Valve coefficient
DEA	Diethanolamine
gCSS	Gas Cyclic Steady State
HCPs	Hyper crosslinked polymer
LDF	Linear Driving Force approximation
MEA	Monoethanolamine
MF	Porous melamine–formaldehyde
MOF	Metal organic framework
ODE	Ordinary differential equations
PANI	Polyaniline
PDE	Partial differential equations
PEI	Polyethyleneimine
PEHA	Pentaethylenehexamine
PFA	Porous aromatic frameworks
PIMs	Polymers with intrinsic microporosity
POP's	Porous organic polymers
PSA	Pressure Swing Adsorption
TEPA	Tetraethylenepentamine
TSA	Temperature Swing Adsorption
TrzPOP	Triazine based porous organic polymer
UDS1	First order upwind differencing s.cheme
VSA	Vacuum swing adsorption
WGS	Water gas shift

Subscripts

H	High
L	Low
i	Component
a	Ambient

Superscripts

*	Equilibrium condition

LIST OF FIGURES

LIST OF TABLES

TABLE OF CONTENTS

1 INTRODUCTION

Industry and Petroleum refineries are among the most significant contributors to anthropogenic CO_2 emissions. Within the industry, the iron and steel industry are the most energy-consuming manufacturing sector. The iron and steel production are still primarily coal-based, thus dependent on fossil fuels responsible for CO_2 emissions. In 2020, the global iron and steel industry emitted about 2.6 Gt of CO_2, about 8.3% of the world's anthropogenic CO_2 emissions [1].

During the last ten years, world crude steel production has increased by 30% due to the growing industrialisation of developing countries. Due to increasing urbanisation, this steel demand will likely increase even more in the coming years. (IEA (2021), Iron and Steel, IEA, Paris [1].

Mitigating these total CO_2 emissions while steel production continues to rise is the major challenge for the iron and steel industry. Therefore, carbon capture is essential to enable the use of carbon while reducing CO_2 emissions into the atmosphere.

1.1 Research goal

This research aims to obtain benchmark numbers for the performance of CO_2 capture using adsorption. For this, a PSA model must be constructed to estimate these values. To build the model and determine the required results, the following research questions need to be answered:

1. What are the possible adsorbent materials for CO_2 capture?
2. What are the requirements of an ideal adsorbent material for CO_2 sequestration from steel gases?
3. Which isotherm models can be used for multi-component adsorption from steel gases?
4. What optimal values of the following parameters use the mathematical model for the adsorption-desorption cycle?
    - purity & recovery of CO_2 (key indicators)
    - operating pressure range
    - amount of adsorbent material needed
    - column sizing
    - number of columns required
    - breakthrough times of different components present in the steel gas
    - pressure drop along the column length
    - associated compressor/blower energy required to operate the adsorbent column between the desired pressure range

To achieve these goals, we will work step by step towards a rigorous model using the software Aspen Adsorption™. First, an extensive literature study is performed to investigate which adsorption material is most suitable for the adsorption of CO_2 from steel gases, considering the conditions of the PSA process. Subsequently, a choice will be made for the best descriptive adsorption isothermal model for

the different gas components in the steel gas. Besides the adsorption isothermal model, other models will be studied that are used for the material, momentum, and energy balances.

With this information, the adsorbent bed will be modelled using a dynamic model that will calculate all the kinetics, mass – energy transport between the gas and the adsorbent solid in the bed.

Finally, the model will be validated using experimental data from the literature. The validated model will then be used in a base case, further optimised in a parameter study. The final optimised model will be used to simulate the performance of CO_2 capture.

1.2 Report structure

This thesis is structured based on the following topics:

• Chapter 2: Steelmaking process and CO_2 capture

This chapter starts with a brief description of the steel production process at Tata Steel Ijmuiden. Subsequently, an overview of the possible CO_2 capture technologies will eventually end with physical adsorption. Finally, the various potential adsorbents for CO_2 are listed and compared with each other based on their advantages and disadvantages.

• Chapter 3: Methodology

This chapter contains all information about how the CO_2 capture model is built. First, an overview is given of all the mathematical equations on which the model is based. A simple one-bed adsorption model is built, which is then validated with experimental data from the literature. Next, the validated adsorption model is further extended to a continuous PSA model. This model is further optimised in an extensive parameter study.

• Chapter 4: Results

The optimised model is discussed in detail in this chapter, and the results are presented. In the second part of this chapter, possible further improvements to the model are suggested by adding several steps to the PSA cycle, each of which has its advantages and disadvantages.

• Chapter 5: Discussion

This part of the study begins with a brief description of the critical findings of this study. In addition, the results are compared with those of several other investigated CO_2 capture technology by R&D at Tata Steel Ijmuiden. Furthermore, the limitation of the model and the modelling software used are listed. Finally, several recommendations are made for further research on this research.

2 STEEL MAKING PROCESS AND CO_2 CAPTURE

2.1 Steel-making process

Two main iron - steel production routes are the blast furnace, basic oxygen furnace, and the direct reduction, electric arc furnace. See Figure 1. Worldwide 70% of the steel is produced with the blast furnace-basic oxygen furnace route. Tata Steel Ijmuiden produces steel via the blast furnace route [1].

The main process of iron making via the blast furnace process is the production of hot metal from sinter and pellets. Blast furnace iron making operation receives ferrous and carbonaceous feedstock from the raw materials preparation processes.

Coke as energy and reductant source of the blast furnace ironmaking is produced from coking coal. Coke making is a thermal decomposition of coal into coke. The main products of this process are the coke, tar, benzole and the coke oven gas (COG). This treatment makes the coal more porous and increases physical strength and therefore makes suitable for use in the blast furnaces. Some of the coal is ground into powdered coal. This fine coal (pulverized coal) is injected directly into the blast furnaces with oxygen enriched hot blast to reduce coke rate.

The second process is the 'pre-baking' of fine iron ore into lumps and marbles, which are called sinter and pellets. After that, the actual production of crude iron in the blast furnace starts. Main product of the blast furnace is “pig iron.” Liquid pig iron is produced from reduction and melting of the ferrous burden; i.e., sinter and pellets using the reducing power and thermal energy supplied by gasified cokes. In addition to the coke, sinter, and pellets charged to the top of the furnace, oxygen-enriched hot air is injected with powder (pulverized) coal at the tuyeres. This process results in a partial combustion of the carbon from coke and coal, creating reducing gases (that contains carbon monoxide and hydrogen) that supply heat and reducing gases to the furnace. The produced hot metal is tapped from the blast furnace at a temperature of approximately 1500°C and transported to the basic oxygen furnace (BOF) using hot metal torpedo’s. This crude iron has a high content of carbon (4-5%) and several impurities (e.g., silicon, manganese, phosphorus, etc) that were originally present in the ore. By adding limestone (in the sinter and pellets), a large part of the impurities is bound to the blast furnace slag. The blast furnace slag is used as a raw material in the cement industry [1].

In the BOF, crude steel is produced from pig iron. Converting iron into crude steel mainly means lowering the carbon content and further elimination of the impurities. The pig iron contains a lot of carbon, which means that the solidified material is brittle and cannot be welded, forged, or deformed. In the steel mill, the carbon is burned from the liquid iron by blowing oxygen with great force. The temperature rises to approximately 2000 °C. The product of this process is therefore crude steel that is further processed (in the secondary metallurgy, steel casters, hot strip mill, cold strip mill and downstream processes) according to the wishes of the customers [1].

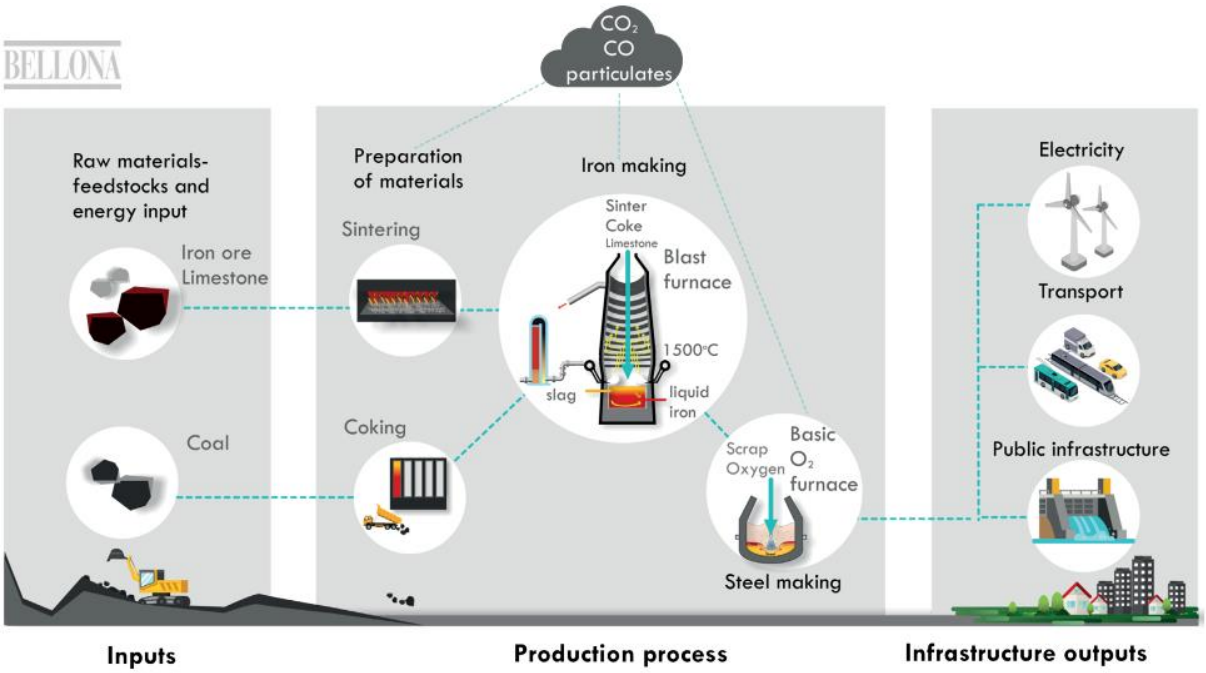

Figure 1 Steelmaking process via the BF-BOF route [1].

2.2 Steel gases

Steel production processes produce substantial amounts of gases. These are gases produced during the processes of coke production (COG), blast furnace (BFG), and basic oxygen furnace (BOFG). The mixture of the furnace gasses is used on site to generate thermal energy and electrical power for the iron and steel works. Part of the BFG, BOFG mix is delivered to near site power plant (Velsen Noord 24/25) for an electricity production that emits CO_2. Alternatively, CO_2 contained in these gases can be captured pre-combustion for (storage and utilisation). In this scheme, CO_2 lean product gas increases its energy content (value), CO_2 rich product can be further compressed for storage and/or used as a feed to CO_2 utilisation process (e.g., synthesis of chemicals, fuels). In this set of work, BFG, BOFG mixture that is currently used as fuel in the VN24/25 power plant will be used as feed to the CO_2 capture process. The feed chemical composition (dry), flow rate, temperature and pressure of this gas mixture is given Table 1.

Table 1 Chemical composition, pressure, temperature, and flow rate of the feed gas (BFG and BOFG mixture).

	Mole fraction (dry)
H_2	0.0525
N_2	0.3687
CO	0.2954
CH_4	0.0109
CO_2	0.2535
H_2O	0
O_2	0.0066
Temperature (K)	288
Pressure (bara)	1
Mass Flows (kg/hr)	734604
Mole Flows (kmol/hr)	24104

2.3 Technological Routes for CO_2 Capture

Carbon capture is a highly active and growing field of research. Some technologies have already been developed and have been applied on a large scale, others are still in the research phase. Most of the carbon capture technologies are expensive and need further improvement in improving efficiency and lowering costs. [2][3]
Based on the location of capture there are two major types of technologies for CO_2 capture systems, namely pre-combustion, post-combustion, and oxyfuel combustion. Pre-combustion capture takes place before the combustion process. Here, CO_2 is captured from a raw synthesis gas or after the CO is converted to CO_2 in a water gas shift reaction. Post-combustion on the other hand is the capture of CO_2 in the exhaust gases after the fuel has been completely burned in the presence of air. Alternatively, CO_2 is captured after an oxyfuel combustion where the fuel is burned in the presence of high purity oxygen instead of air. As a result, the exhaust gases consist primarily of CO_2 and H_2O and lean in N_2 from which the CO_2 can be captured. [4]

The aim of this research is the capture CO_2 from steel gases specifically from furnace gases (BFG+BOFG). No substantial changes should be made to the blast furnace process. Pre-combustion carbon capture can therefore be used, where the raw blast furnace and basic oxygen furnace gasses will go through a carbon capture unit.

2.4 Post-combustion CO_2 capture technologies

Various technologies may be employed for carbon dioxide capture from furnace gasses. Figure 2 illustrates several technologies that have been researched and applied by industry or are under research in academia. The technologies of (chemical/ physical) absorption, adsorption, membrane, biological capture, and cryogenic capture are the main CO_2 capture technologies.

Many of the CO_2 capture technologies have been extensively discussed in the literature, including chemical absorption [5] [6], physical absorption [7] [8], adsorption [9] [10], membrane separations [11], cryogenic-based CO_2 capture [12] [13] and CO_2 capture using microalgae [14] [15] [16]. This work only involves the physical adsorption of CO_2 from steel gasses.

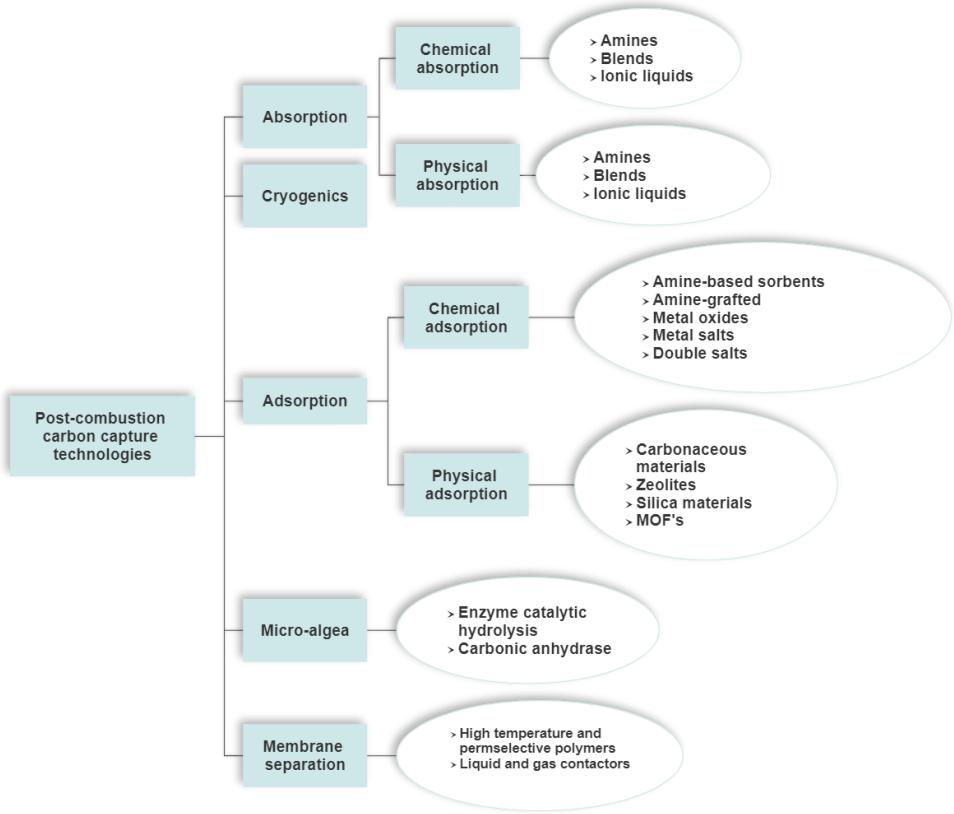

Figure 2 Overview of carbon dioxide capture technologies (modified from [17] and [18])

2.5 Physical adsorption

The working principle of adsorption relies on the attachment of substances (adsorbates) to the surface of a solid called the adsorbent. In principle, adsorption is a physical bond based on Van der Waals forces and not on a chemical bond. To obtain a stronger bond with the substance to be removed, the adsorbent can be treated with chemicals so that a chemical bond is also possible.

Adsorption is a reversible process, i.e. the substance to be removed can both adhere to the surface of the adsorbent. The adsorbent can be regenerated by releasing the adsorbate from its surface. Adsorption is an exothermic process, heat is released during the bonding, but regeneration energy is required. The regeneration of the adsorbent material during the CO_2 capture by a physical process requires less energy than a typical procedure using chemical sorbents. This is due to the absence of newly formed chemical bonds during chemical adsorption, reducing the energy requirement for regeneration.

The equilibrium between the surface adsorbed substance's concentration, and the substance's concentration in the gas or liquid depends on the amount of temperature and pressure. These equilibriums are described with adsorption isotherm.

2.6 Adsorbents for CO2 capture

Capturing CO_2 by adsorption is a mature concept in which various materials have been developed based on the place of adsorption in the system (pre-combustion, post-combustion or oxycombustion). Historically, activated carbons (ACs) and zeolites were the first solid adsorbents used for CO_2 capture [19]. Nevertheless, over the years, it has become clear that these are not the only CO_2 adsorbents. However, many materials have recently been designed, such as metal-organic frameworks (MOFs), polymers, and metal oxides, to improve CO_2 adsorption efficiency, as shown in Figure 3. These adsorption materials will be discussed in more detail in the following chapters. Figure 3 shows that more and more research is being done for these new adsorbents resulting in increased number of publications.

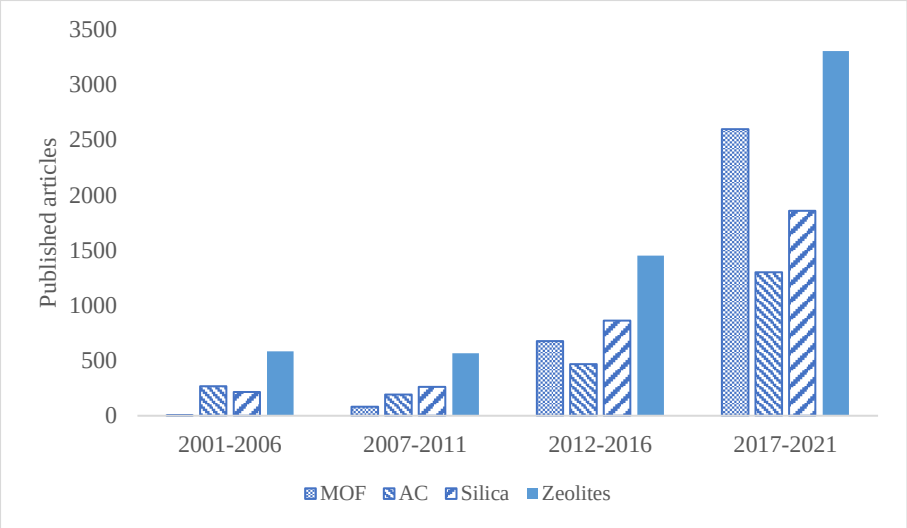

Figure 3: Number of publications on CO_2 capture with various solid materials for the last 2o years. Based on the number of publications in 'ScienceDirect' by searching "CO_2 adsorption" and the type of the adsorbent.

The most important characteristic of an adsorbent material is its high porosity. Thus, physical characterisation is more important than chemical characterisation [19]. The most important physical characteristics of adsorbents are the pore volume, size distribution and surface area. The surface area can be determined by the BET method[1] [19]. The total pore volume and the pore size distribution are needed to characterise the pore volume. According to the International Union of Pure Applied Chemistry (IUPAC) classification [20] the pores are subdivided by diameter (d) into macropores (d > 500 Å), mesopores (20 Å < d < 500 Å), and micropores (d < 20 Å). The pore size distribution is calculated with the kelvin equation, and the total pore volume can be determined for the adsorption and desorption isotherms.

[1] The BET measurement is a term for an analysis method for determining the size of surfaces, in particular porous solids, by means of gas adsorption. A gas, often nitrogen, is passed over the material to be examined. By cooling, usually with liquid nitrogen, the amount adsorbed below the saturation vapor pressure of the sample gas (adsorption) can be determined with a standard manometer [19].

Figure 4 shows the potential porous solid adsorbents for the CO_2 capture and their capacity at the temperature range. From this figure we can deduce that the adsorbents that have a good working capacity and stability in de temperatures between 200 K and 400 K are porous carbonaceous materials, zeolites, MOFs, and porous organic polymers. Mesoporous silica and metal oxide-based adsorbents can also be used as CO_2 adsorbents in this temperature range.

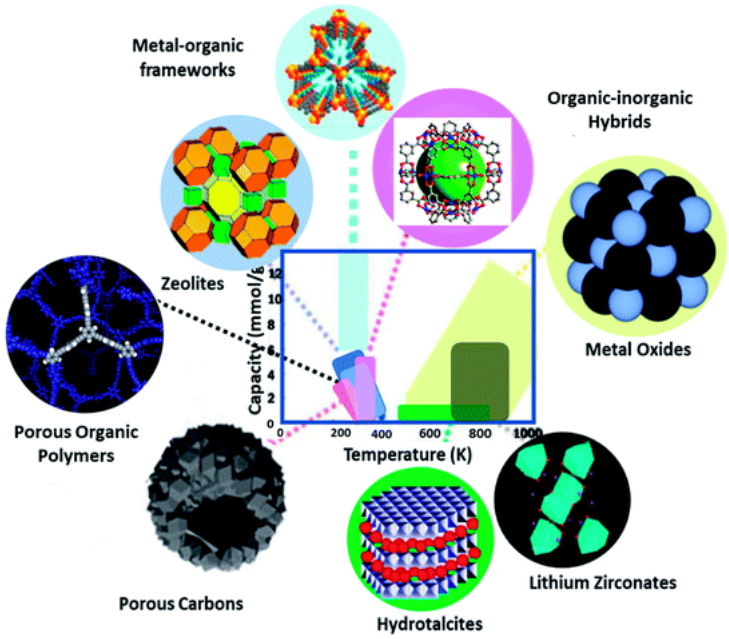

Figure 4 Potential porous solid adsorbents and their capacity at the temperature range [21].

1) Carbon-based adsorbents

Carbon bathed adsorbents are abundant, cheap, easy to make and chemically and hydrothermally stable. The main types of carbon-based adsorbents are activated carbons (AC's), carbon molecular sieves (CMS), activated carbon fibers (ACF's) and graphene [22].

Activated carbon is the most used carbon-based adsorbent. It is produced from carbonaceous raw material such as wood, peat, coals, petroleum cokes etc. Some of these materials are already porous and more pore with the desired size distribution are created in an activation process. The AC can then be used as an adsorbent material. The surface of AC is nonpolar or slightly polar. This means that the adsorption process with AC's does not need any prior stringent moisture removal and it can be used in aqueous processes. The heat of adsorption, or bond strength is generally lower on AC's than on other adsorbent materials. Thus, low energy is required for the regeneration of the adsorbent material. Carbon-based adsorbents have been very popular throughout the history of adsorption and show a high adsorption capacity for CO_2 at ambient pressure and temperature [22].

The surface area of activated carbon varies from 500 to 3000 m^2/g [23]. Activated carbon as a high porous material shows a remarkably high potential for CO_2 capture systems where the CO_2 purity is no

more than 90%. It is not the best adsorptive material when higher purities are asked, because the CO_2 selectivity is relatively low in presence of other gases (e.g., N_2, H_2, CH_4, etc.).

Numerous studies have been done on how to enhance the adsorbate-adsorbent interaction and the selectivity of AC for CO_2. This can be done by modifying and increasing the adsorbent surface by and by tuning the pore structure by using different precursors. The pore size can be easily controlled by varying the preparation and activation conditions [24], [25], [26]. Another possibility is by forming other structures such as carbon nanotubes (CNT's), ordered mesoporous carbon, microporous carbon, etc. Another most used modification method is to increase the alkalinity of the adsorbent surface resulting in an increased CO_2 adsorption capacity [27] [28]. This can be done, for example, by grafting functional groups on the carbon surface, which is achieved by various treatment methods [29] [30] [31] [32].

Nandi et al. [33] overview the possible different surface functional groups that enhance the adsorption characteristics. An essential drawback of this modification method is that despite an increased interaction of CO_2 with the surface, the adsorption capacity is decreased because the additive blocks the porous carbon structure [34] [35].

In this field, modified ACs have been manufactured that consistently show a better CO_2 uptake rate. The primary research and most showed potential are the N-enriched microporous activated carbons. At ambient conditions (298K, 1bar), the adsorption capacity of unmodified AC is about 1.20 mmol/g [36].

Wang et al. [37] synthesised very promising, highly porous carbons with polyaniline (PANI) as a carbon precursor and KOH as an activating agent, for which a remarkably high CO_2 adsorption capacity of 4.50 mmol/g with high selective adsorption of CO_2 over N_2 (0.27 mmol/g) at ambient temperature and pressure, which was the best adsorption capacity ever achieved with a porous carbon until the publication of this article.

Later, Nandi and colleagues [33] fabricated a series of N-dopped highly porous activated carbon monoliths. These monoliths showed an astonishingly high CO_2 adsorption uptake of 5.14 mmol g−1 at ambient pressure and temperature. Another N enriched microporous active carbon was studied by Sultana et al. [38], and they achieved a still high CO_2 adsorption capacity of 6.22 mmol/g at ambient temperature and pressure. This adsorbent also showed high selectivity of CO_2 /N_2 of 33, and good adsorption-desorption recycle stability.

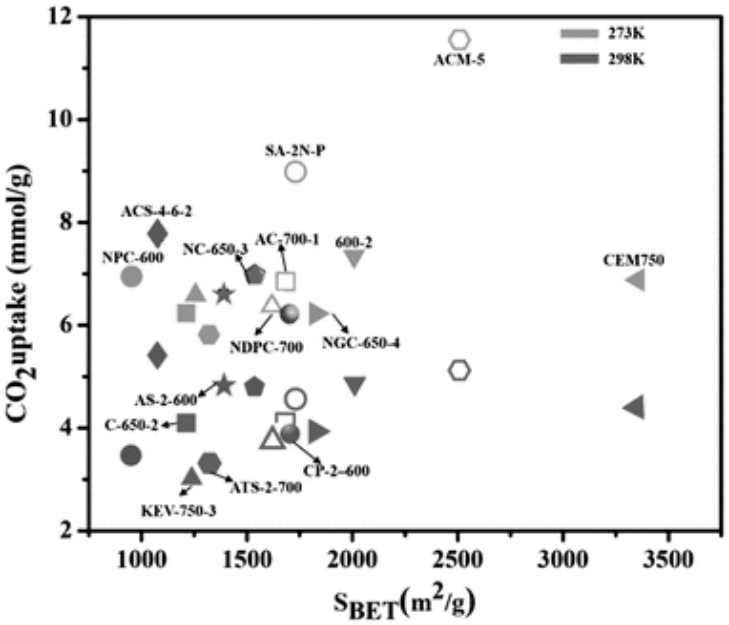

Figure 5: Different porous carbon-based adsorbents for CO_2 captured at different temperatures (273 K, 298 K) for 1 bar pressure [39].

2) Zeolites

Zeolite is an aluminium silicate; this can occur naturally or be made synthetically. A zeolite is made up of silicon, aluminium, and oxygen atoms, combined in a solid crystalline structure. These atoms form tetrahedra, which in turn can form cages. This gives the zeolite a very porous structure. The pore size of the zeolite's frameworks can vary between 5 and 12 Å [40] [22].

However, the structure of a zeolite is very regular, and the concatenated cages form a kind of channel. The cages can contain small molecules (such as water) and ions. The ions are often needed to compensate for the negatively charged structure of Si, Al, and O [40].

Zeolites can adsorb CO_2 in two ways. Separation of CO_2 from the other gases based on the size of the molecules with the Zeolites playing the role of a molecular sieve. However, for CO_2 separation, the separation is based on the polarisation interaction between the gas molecule and the electric field on the charged cations in the zeolite framework. This means that zeolites are an excellent adsorbent for polar substances, and the interaction will be high for the gas molecule with a relatively sizeable energetic dipole and quadrupole [40].

CO_2 removal by zeolites can be controlled by varying the pore size, polarity, and type of the additional framework cations. Due to this enormous flexibility to control their porosity and crystallinity, numerous zeolites have been studied for CO_2 capture using zeolites A, X and Y and various natural zeolites such as Chabazites, clintopiles, ferrierites, modenites, etc.

Two main factors play an essential role in zeolites' adsorption effectiveness: their basicity and the Si/Al ratio [39]. The primary one is the basicity of the zeolite, which is quantified by aluminium content in the silicate framework [41]. The next one is the ratio of the Si/Al that affects the cation exchange capacity. High cation exchange capacity goes together with high CO_2 uptake, which is obtained when the Si/Al ratio is low [39].

Although zeolites have an excellent affinity for CO_2, zeolites have a significant better CO_2 adsorption capacity at room temperature, and the capacity decreases rapidly with increasing temperature above 30 °C and becomes negligible after 200 °C [42] [43]. The capacity will also be deficient in moisture [40].

The most studied zeolite with high crystallinity and, high surface area are studies for the CO_2 capture, including zeolites A [44], X [45] [46] [47], and Y [48] [49] [50], β [51], ZSM [52] [53] [54], CHA [55] [56] and natural zeolites ZAP's, ZNT and ZN-19 [57]. Some of these zeolites are presented in Figure 6.

These zeolites are modified mainly by altering the aluminium content in the frameworks or exchanging the cation (e.g., Li, Na, Al etc.), which changes the zeolite acid-base capacities. Walton et al. [58] studied the adsorption behaviour of zeolites X and Y modified by Li, K, Na, Rb and Cs. The Li-modified zeolites showed the best CO_2 uptake capacity. The same results were obtained by Diaz et al. [59]

Harlick et al. [60] performed an extensive adsorbent screening study into the ideal adsorbent for the PSA for the separation of CO_2 from the gas mixture. The zeolites examined were 13 zeolite-based adsorbents, including 5A, 13X, NaY, NaY-10, HY-5, HY-30, HY-80, HiSiv 1000, H-ZSM-5-30, H-ZSM-5-50, H-ZSM-5-80, H-ZSM-5-280, and HiSiv 3000. This study found that If a low-pressure CO_2 feed and low regeneration pressure are used, then the NaY and 13X adsorbents should be used. At a temperature of 295K and pressure of 1 bar, zeolites 13X and NaY showed a capacity of 4.61 mmol/g and 4.06 mmol/g, respectively.

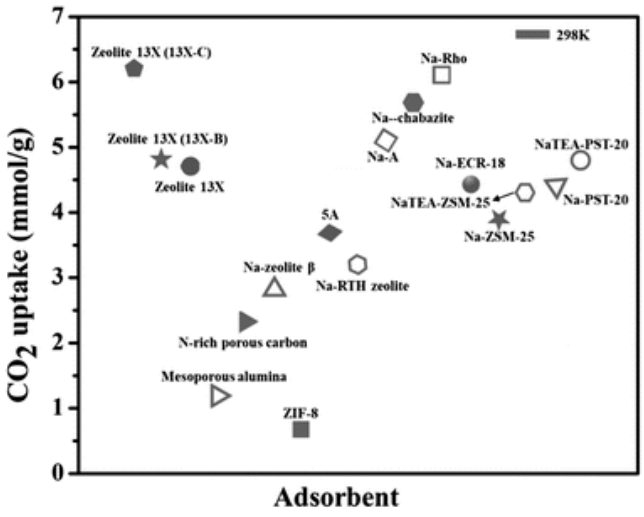

Figure 6: CO_2 adsorption capacities of zeolite-based adsorbents. *[21]*

3) Mesoporous silica

Mesoporous silica has received more attention over the past 20 years, and that is because mesoporous silica has very ordered pores compared to conventional silica. Mesoporous silica can be modified to function as an excellent CO_2 adsorbent by replacing the silanol groups on the surface with other organic groups [22].

The most common is the implementation of amino groups on the mesoporous silica surface. These groups can be applied by impregnation or by post-synthesis methods. For the CO_2 capture, the post-synthetic method is mainly applied, where the CO_2 uptake occurs through chemisorption [61].

The most used amine molecules used for impregnation in the literature are polyethyleneimine (PEI) [62], tetraethylenepentamine (TEPA) [63], monoethanolamine (MEA) [64], diethanolamine (DEA) [64], pentaethylenehexamine (PEHA) [65]. Most of the studies about CO_2 capture with mesoporous silicas include MCM-41 [66] [67] [68] [69], MCM-48 [70] [71], SBA-15 [68] [71] [72] [73]. Thanks to the high specific surface area and the high pore volume, these supports can provide more active sites for the reaction of amines with CO_2.

Among the adsorbents, organic amine-modified SBA-15 solid adsorbent has become one of the research hotspots in CO_2 capture. Zhao et al. [74] studied CO_2 adsorption on 60 wt% TEPA functionalised Mesoporous SBA-15. All the impregnated SBA-15 sorbents showed reversible CO_2 adsorption behaviours with fast adsorption kinetics in the ambient pressure and temperature. It was also found that the CO_2 uptake increased significantly in the presence of moisture. The adsorbent showed the highest CO_2 adsorption capacity of 5.22 mmol/g in pure and humid CO_2 at 75 °C.

Fheng et al. [75] studied the CO_2 adsorption on EDA-SBA-15. The sorbent adsorbs around 20 mg/g of CO_2 from 15% CO_2 in N_2 at 25 °C and 1 total atm pressure and 86 mg/g from pure CO_2.

4) Metal-organic frameworks (MOFs)

Metal-organic frameworks (MOFs) are microporous materials consisting of inorganic building units (metal clusters) and organic molecules as connecting elements (ligands) between the inorganic building blocks. MOFs are so-called coordination polymers with an open framework, which may contain pores [22].

There specific are rages from 1000 to 10,000 m^2/g [76] [77]. The affinity of the MOFs can be tuned towards CO_2 by functionalising the pores with nitrogen-containing organic groups, adding strongly polarising organic functional groups and exposing the metal cation sites on the surface of the pores.

In the case of adding polarising functional groups for better CO_2 capture, the addition of basic nitrogen-containing organic compounds has been widely investigated. These modified adsorbents are classified in classes of heterocycle derivatives [78] [79] [80], aromatic amino derivatives [81] [82] [83] [84] [85] and alkylamine bearing frameworks [86] [87]. The addition of other strongly polarising organic compounds (e.g., hydroxyl, cyano, thio, halide, and nitro groups) to the MOF is also investigated for CO_2 adsorption. With this, the CO_2 adsorption is improved by the polarising strength of the functional groups [88] [89] [90] [91].

The second modification is by generating of structure where the pore structure consists of exposed metal cation sites. With this, the selectivity and the affinity of the MOF for CO_2 are improved [92] [93] [94] [95].

In the field of adsorption for gasses separation, MOFs are famous for their high adsorption capacity, particularly for H_2 adsorption [96] [97], and CH_4 adsorption [98] [99]. A series of MOFs are studied in the literature that can be used for CO_2 capture at ambient temperature.

Among all the studies of MOF, Mg-MOF-74 has shown the highest CO_2 capacity in ambient conditions. Wu et al. [100] studied two isosteric M-MOF-74 (M = Ni, Mg) and obtained that the BET surface areas of Mg-MOF-74 have been increased by 242 m^2/g and Mg-MOF-74 showed a CO_2 adsorption capacity of 9.95 mmol/g at 1 bar, 298 K.

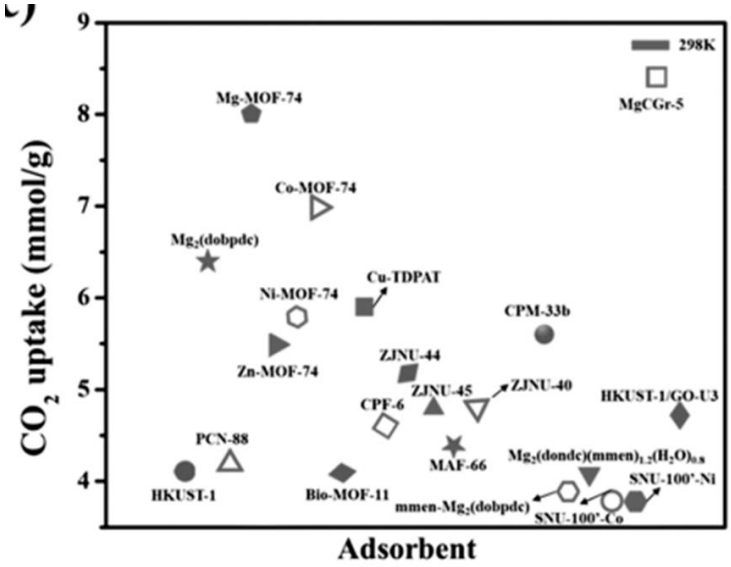

Figure 7 Different MOF-based adsorbents for CO_2 uptake at 298K [21].

5) Polymer-based adsorbents

Porous organic polymers (POPs) are crosslinked networks of polymers built from various organic building blocks. For the last few decades, polymers have been recognised as promising for carbon dioxide capture due to their low density, high thermal and chemical stability, large surface area, tuneable pore size and structure by introducing specific functional building blocks [101]

To date, diverse types of POPs has been studied for CO_2 capture; these are hyper crosslinked polymers (HCPs), polymer with porous aromatic frameworks (PFA), porous melamine–formaldehyde (MF), covalent organic polymers (COP), polymers with intrinsic microporosity (PIMs), conjugated microporous polymers (CMPs) and polymer with covalent triazine based framework (CTF) [102].

In each of these groups, several promising adsorbents with high potential for CO_2 capture have been studied. However, the POPs with the highest CO_2 uptake capacity are the triazine-based porous organic polymers that have shown the highest CO_2 uptake capacity among all porous polymers reported to date. Das et al. [103] studied the CO_2 uptake by TrzPOP-1, -2, and -3 with a BET surface area of 995, 868, and 772 m^2/g, respectively. At 298 K, TrzPOP-1, -2, and -3 displayed CO_2 uptake capacities of 3.53, 4.52 and 5.09 mmol/g, respectively, up to 1 bar pressure.

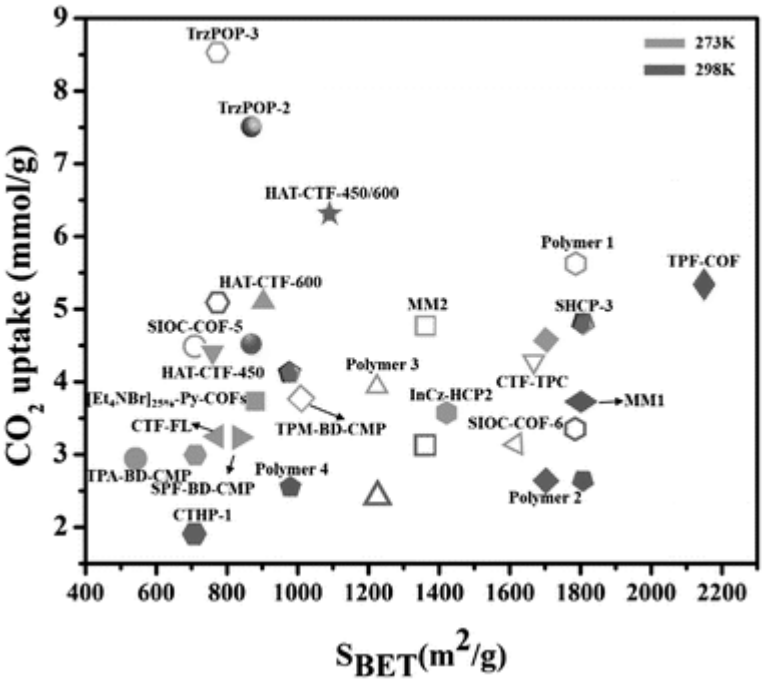

Figure 8: Different porous organic polymers for CO_2 captured at different temperatures (273 K, 298 K) for 1 bar pressure [21].

6) Porous metal oxides

Metal oxides have been a potential candidate for CO_2 capture for the past ten years. In the desorption process, these porous oxides blend with CO_2 and form carbonates in a chemical reaction. The metal oxide got the addition because of its low cost and low toxicity, mainly MgO. However, the CO_2 sorption capacity of these low-cost materials is too low under ambient conditions. The sorption capacity is higher at higher temperatures [104].

Han et al. [105] studied the adsorption of CO_2 in flue gas by a MgO-based porous adsorbent. It was concluded that with the microcrystalline MgO existing in the alumina framework, one could capture 77 and 131 mg/g of CO_2 at 200 °C in the absence or presence of water vapour, respectively the regeneration is performed at 600 °C.

These metal oxides can also be dopped to enhance their CO_2 capture capacity and lower the operating temperature. Liu et al. [106] dopped the MgO sorbent with alkali-metal carbonates, which enhanced CO_2 sorption capacities at low and moderate operating temperatures compared with pure MgO sorbents. MgO-doped Cs_2CO_3 had a maximum CO_2 sorption capacity greater than 8.36 wt.% at 573 K.

Another drawback besides the high regeneration temperature is the rate of the chemical reaction, which is too slow and requires high energy consumption [107].

Table 2: A summary table for the possible adsorbents for PSA from CO_2 at ambient conditions. The advantages and disadvantages referred to in [108] are supplemented by [109]and [110]. The studied best-performing adsorbents of all groups are shown with their conditions and performance.

Adsorbents	*Advantages*	*Disadvantages*	*Examples*	*T [°C]*	*P [bar]*	*Capacity [mmol/g]*	*Selectivity (CO_2/N_2)*	*Ref*
AC	Low production cost (obtained from a wide range of low-cost precursors. Considerable variation in textural properties, leading to a wide variation in performance between adsorbents Good adsorption capacity at high-pressure (> 4bar) and low temperature (< 50 °C) Competitive kinetics with zeolites High cyclic stability	Sorption capacity decreases dramatically with an increase in temperature The presence of impurities in the gas stream significantly reduces sorption capacity The presence of moisture in the gas stream significantly reduces sorption capacity	AC PANI-KOH-AC N-dopped AC	25 25 25	1 1 1	2.8 4.5 6.22	- 16.7 33	[36] [37] [33]
Zeolites	Large micropores/mesopores Medium CO_2 adsorption (at 298 K and 1 bar) Fastest adsorption kinetics (equilibrium capacity within few minutes) High CO_2 selectivity (5 - 10 times higher CO_2/N_2 selectivity compared with carbonaceous materials) High cyclic stability High mechanical stability	Expensive Poor performance in the presence of moisture Heavy energy consumption during CO_2 desorption (poor economic feasibility) The presence of impurities and moisture in the gas stream significantly reduces sorption capacity,	13X NaY	22 22	1 1	4.61 4.06		[60] [60]
Mesoporous silica	Low production costs low regeneration energy Large and accessible pore volume high surface area, high pore volume Tunable pore size, High working capacity Fast kinetics High CO_2 selectivity over CH_4 and N_2 Good cyclic stability Good mechanical stability Good tolerance to impurities and moisture (some have enhanced adsorbing capacity in the presence of water)	High energy requirement (high sorption capacity at high pressure (~45 bar) and ambient temperature) Low hydrothermal stability	TEPA-SBA-15 EDA-SBA-15	75 25	1 1	5.22 1.95	- -	[74] [75]
Metal-organic frameworks (MOFs)	Large specific surface area Extra high porosity Regular pore distributions Easily tunable pore characteristics Adjustable chemical functionality High thermal stability	High production costs results in poor economic efficiency Complicated synthetic process Mostly VSA process (poor economic feasibility) Compared with zeolites and AC, poor performance at low CO_2 partial pressure (0.1–0.2 bar). Unsuitable for use at high temperatures. Low CO_2/N_2 selectivity Moisture-sensitive (Water molecules cause structure failure by destroying the crystal lattice of MOFs by displacing the ligands Impurities cause a significant reduction in capacity.	Mg-MOF-74	25	1	9.95	192	[100]

Polymer-based adsorbents	low density		TrzPOP-1	25	1	3.53	43	[103]
	tunable pore structure and functionality		TrzPOP-2	25	1	4.52	75	[103]
	large specific surface area		TrzPOP-3	25	1	5.09	94	[103]
	physicochemical stability							
	porosity at the nanoscale level							
Porous metal oxides	Easily available	High consumption of energy due to adsorption/desorption at medium to high temperatures (>673 K)	MgO (absence of water)	600	1	1.7	-	[105]
	Dry chemical absorbents		MgO (presence of water)	600	1	3.0	-	
	Adsorption/desorption at medium to high temperatures (>673 K)	High cost for regeneration	Cs_2CO_3 dopped MgO	573	1	1.9	-	[105]
	Popular as a pre-combustion absorbent	Demand for continuous addition of absorbents						[106]
		Low reaction rate						

Since this study is about capturing CO_2 from the BFG and BOFG using the PSA technology, there are many possibilities for the type of adsorbent, as seen in Table 2. In this table, the CO_2 capture capacities for all the examples are given based on the adsorption of pure CO_2 gas.

Zeolites and AC are two classical adsorbents for CO_2 capture already widely used. However, the literature shows a range of other adsorbents in the research phase that can also perform well in CO_2 capture.

For a large-scale industrial process such as steel production at Tata Steel Ijmuiden, processes must be economically profitable and highly efficient.

A porous metal oxide is a very promising adsorbent in the field of carbon capture. However, it requires a very high regeneration temperature and high energy consumption.

MOFs show promising CO_2 adsorption capacities with the largest surface area in the ambient temperature and pressure range. Their structure can be easily indicated by taking into account the composition of the feed gas. However, for MOFs, many important issues need to be addressed to make them suitable for a large-scale PSA process, including the effect of impurity components in the feed gas. The most important drawback is the high price of the MOFs.

Similarly, mesoporous silica with additional amine functionalisation shows improved CO_2 adsorption because the CO_2 has a high affinity for amine. Although this high affinity for CO_2, the amine has a low CO_2 adsorption capacity at ambient and high temperatures, so there is a risk for possible amine degradation. These adsorbents are not yet applicable to performing in a standard PSA-based system.

Polymer-based adsorbents exhibit very good physical properties essential for the adsorption-desorption process and show an high affinity for CO_2. However, there is not enough research about the polymer-based adsorbents for a PSA for CO_2 capture in the literature. Therefore, using these adsorbents is a very new idea and thus needs much research before it can be used in a large-scale process.

The two promising options for the PSA are the remaining two adsorbents AC and zeolites. Both have large adsorption capacities at low pressures and moderate temperatures, but zeolites offer CO_2 /N_2 selectivity 5 to 10 times greater than carbonaceous materials due to their large specific surface area. Both have fast kinetics and can exhibit the cyclic stability required in a PSA process. The main drawback of both adsorbents is that they are sensitive to impurities and moisture in the feed stream, reducing their active surface area availability. To avoid this, one can remove water in the feed stream before entering the PSA column, increasing the system's energy demand.

Zeolite 13X has been chosen as an adsorbent in the further analyses in this study.

2.7 Cyclic adsorption and regeneration methods

According to the International Adsorption Society, there are two main types of adsorption gas separation processes: bulk separation and purification [111]. The central industrial purification systems are dehydration of olefin-containing cracked gas, natural gas, air, synthesis gas, etc., air purification, solvents removal from air, organics and sulfur from vent streams and other petrochemical streams.

On the other hand, gas separation has its main applications in producing hydrogen and nitrogen from the air and separating a gas component from industrial gasses. Which CMS, zeolites and ACs are still the dominating used adsorbents in the industry [111]

Based on the process, the adsorptive separation systems are divided into cyclic batch adsorption and continuous flow systems. In cyclic systems, the adsorbent bed is alternately saturated and regenerated cyclically. However, there is a continuous counter-current contact between feed and adsorbent in the continuous flow systems.

Cyclic batch adsorption processes differ mainly in how the adsorbent is regenerated during the desorption cycle.

There are four primary methods to regenerate the adsorbent:

- Pressure swing, where the desorption is accomplished by reducing the pressure (see Figure 9). This results in a decrease of the adsorption enthalpy of the adsorbed gas molecules, followed by desorption. The pressure reduction can be realised quickly; that is why the PSA cycle time is short, usually minutes or even seconds.
- Thermal swing where the bed is regenerated by raising the temperature (see Figure 9). For this, usually, a preheated gas is purged through the bed. The cycle time is more significant than for the PSA because increasing the temperature is a slow process, which can take several hours to a day.
- Inert purge stripping where the bed with the adsorbed gas is purged with a non-heated inert gas.
- Displacement gas purge where the purge gas is also adsorbed in the bed. Thus, the cause of the regeneration of the adsorbate is competence and partial pressure reduction of the adsorbate.

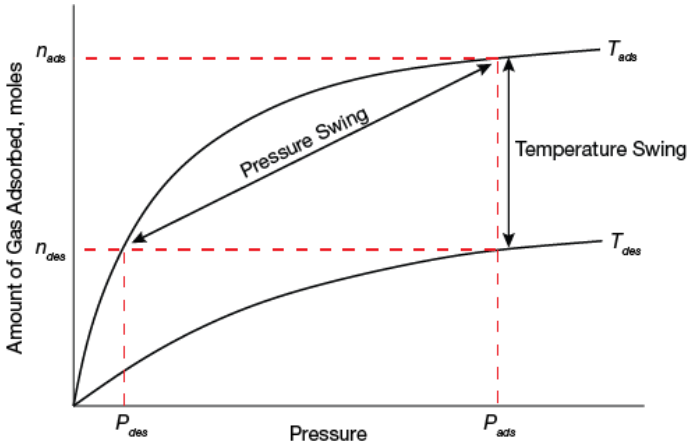

Figure 9 Schematic isotherms show pressure and thermal swing operation for an adsorption process.

3 METHODOLOGY

Dynamic process simulators can be used to build a PSA cycle to capture the CO_2 from BFG. In this study, the dynamic simulation of the carbon dioxide capture from steel gases in a multi-bed PSA system was performed using the process simulator Aspen Adsorption™.

First, choices are made for the sub-models on which the adsorption and desorption behaviour of the model is based. This mathematical behaviour of the fashion is validated with experimental data to check whether the assumptions made in the model are acceptable. Once the model has been validated, a base case can be drawn upon which an extensive parameter study is performed. This involves investigating the effect of several essential parameters on the functioning of the adsorption model and determining the optimal values of these parameters. This optimises the model.

3.1 Mathematics of the adsorbing bed

The PSA model consists of a combination of the mass, momentum, and energy equations, adsorption equilibrium and kinetics models, together with the input of the initial and boundary conditions to define the adsorption and desorption behaviours in the PSA cycle.

For modelling the PSA process in Aspen Adsorption™, aspen properties, with property methods PENG-ROB (the equation of state is expressed by the Peng-Robinson model) is used. The adsorption is performed in an adsorption bed with one layer of adsorbent material zeolite 13X. The first-order upwind differencing scheme (UDS1) is used to solve the differential equations, and the adsorbent packed bed is discretised into 20 vertical nodes along its length.

In the development of the mathematical model for the PSA model, the following main assumptions are made:

- A gas behaves as an ideal gas.
- The plug-flow model describes the flow pattern through the adsorption bed, where the radial dispersion is neglected.
- The properties of the adsorbent throughout the bed remain constant.
- The porosity of the bed throughout the bed is constant.
- The Langmuir isotherm states the adsorption equilibrium relations for all the components in the feed gas.
- The rate of mass transfer is presented by the linear driving force (LDF) relations, where the diffusion only describes the mass transfer coefficient in macropores.
- The mass transfer coefficient is constant.
- The adsorption process is non-isothermal with no conduction.
- Ergun's equation calculates pressure drop along the bed.

The different models used in this study and the calculated constants are discussed below.

3.1.1 Material and momentum models

The material balance describes the configuration of the adsorbent material bed. The complete material balance for the adsorption bed is given in equation (3-1). This Material balance contains four essential concepts: the radial dispersion contribution, the convection, the gas phase accumulation, and the adsorbed phase accumulation.

$$-D_{Li}\varepsilon_b \frac{\partial^2 C_i}{\partial x^2} + \frac{\partial (v_g C_i)}{\partial x} + \varepsilon_t \frac{\partial C_i}{\partial t} + \rho_b \frac{\partial Q_i}{\partial t} = 0 \tag{3-1}$$

The axially dispersed plug-flow model describes the flow pattern in the bed, and the dispersion coefficient of component i (D_{Li}) varies along the length of the bed. These values are estimated during the simulation using the correlation of Kant, as given in equation (3-2).

$$D_L = 0.73 D_{mk} + \frac{v_g r_p}{\varepsilon_b \left(1 + 9.49 \frac{\varepsilon_b D_{mk}}{2 v_g r_p}\right)} \tag{3-2}$$

It was considered a uniform empty fraction in the entire column.

The momentum balance in the adsorption bed is pressure drive which means that the velocity is related to the pressure gradient in the bed. The Ergun equation (3-3) describes this pressure drop along the bed(3-3), which is valid for both laminar and turbulent flows.

$$\frac{\partial P}{\partial x} = -\left(\frac{150 \times 10^{-5} \mu_g (1-\varepsilon_b)^2}{\left(2 r_p \Psi\right)^2 \varepsilon_b^3} v_g + \frac{1.75 \times 10^{-5} M_W \rho_g (1-\varepsilon_b)}{2 r_p \Psi \varepsilon_b^3} v_g^2 \right) \tag{3-3}$$

3.1.2 Adsorption kinetics model

Several mass transfer resistances determine the kinetics of adsorption in the adsorbent bed in the gas phase adsorption process. The main types of resistances are the resistances between the bulk gas phase and gas-solid interface and the resistances due to the porous structure of the adsorbent; for the kinetic model, the Lumped Resistance model is chosen, where the separate resistances to mass transfer are lumped as a single overall factor (MTC). The linear driving force expression (LDF), as given in equation (3-4), describes the solid Lumped resistance model.

$$\frac{dQ_i}{dt} = MTC_i (Q_i - Q_i^*) \tag{3-4}$$

The mass transfer coefficient $k_{S,i}$ is assumed constant along the bed. Only macropores are considered for calculating the lumped mass transfer coefficient, and equation (3-5) is used. The effective diffusivity equation (3-6) is determined from the molecular diffusivity and the Knudsen diffusivity.

$$MTC_i = \frac{15 D_{e,i}}{r_p^2} \tag{3-5}$$

$$D_{e,i} = \frac{\varepsilon_p}{\tau} \frac{1}{\left(\frac{1}{D_{k,i}} + \frac{1}{D_{m,i}}\right)} \tag{3-6}$$

The Knudsen diffusivity is calculated using equation (3-7), and the molecular diffusivity is calculated using the Chapman-Enskog equation (3-8).

$$D_{k,i} = 9700\, r_p \sqrt{\frac{T}{M_{w,i}}} \tag{3-7}$$

$$D_{m,i} = 0.0018583 \frac{\sqrt{T^3 \left(\frac{1}{M_{w,i}}\right)}}{P \sigma^2 \Omega} \tag{3-8}$$

The dimensionless quantity Ω is the collisional integral for diffusion, which is in the function of the dimensionless temperature $\kappa T/\xi$. The parameters σ and ξ originate from the intermolecular potential energy function of Lennard-Jones, where σ represents the characteristic diameter of collision diameter and ξ represents the characteristic energy, the maximum energy of attraction between the molecules in a gas mixture. For a gas mixture of n components, the values of these parameters can be estimated using equations (3-9) and (3-10). Table E.1 and table E.2 from [112]were used to calculate σ and Ω needed for the molecular diffusivity.

$$\sigma = \frac{\sigma_1 + \sigma_2 + \cdots + \sigma_n}{n} \tag{3-9}$$

$$\xi = \sqrt{\xi_1 \xi_2 \ldots \xi_n} \tag{3-10}$$

Table 3 Mass transfer coefficient of all gas components in feed gas where the particles have a diameter of 2 mm.

	Unit	*CO_2*	*CO*	*H_2*	*N_2*	*CH_4*	*O_2*
MTC	s^{-1}	0.0137	0.0172	0.0641	0.0172	0.0227	0.0228

3.1.3 Adsorption isotherm model

To describe the adsorption behaviour of all gases in the gas mixture on zeolite 13X, an adsorption isotherm model should be chosen that best describes experimental adsorption data.

For zeolite 13X, the adsorption equilibrium data were taken from the literature. Adsorption isotherm of CO_2, CO, N_2, CH_4 and H_2 were taken from Park et al. [113]. For oxygen, there was not enough data available in the literature, so for oxygen, the isothermal constants were taken from the study by Javadi et al. [114].

The experimental adsorption data is fitted with five pure-species equilibrium models using MATLAB® [115]. For this non-linear data-fitting, the non-linear least squares approach is used as given in equation (3-11). The models used for this fitting are given in Table 4. The best fit model for the adsorption isotherm was the Sips and Toth model, see Figure 10. For further analyses, the Sips model was chosen for the adsorption equilibrium for Zeolite 13X.

$$\text{MIN} \sum_i \left|\left|\mathrm{F}(x_i) - y_i\right|\right|^2 \tag{3-11}$$

where $F(x_i)$ is a non-linear function as given in Table 4 and y_i is the adsorption isotherm data (blue dots in Figure 10).

Table 4: An overview of the five different adsorption isotherm models used to fit the experimental adsorption isotherm data [116]

Isotherm	*Non-linear form*	*Linear form*	*Plot*	*Constants*
Linear		$q_e = K_L P$	$q_e vs\ P$	K_L
Langmuir	$q_e = \frac{q_m K_{LM} P}{1 + K_{LM} P}$	$\frac{P}{q_e} = \frac{1}{q_m K_{LM}} + \frac{P}{q_m}$	$\frac{P}{q_e}\ vs\ P$	$q_m\ and\ K_{LM}$
Freundlich	$q_e = K_F P^{1/n}$	$\ln q_e = \ln K_F + \frac{1}{n} \ln P$	$\ln q_e\ vs\ \ln P$	$K_F\ and\ n$
Sips	$q_e = \frac{q_m K_S P^{1/n}}{1 + K_s P^{1/n}}$	$\ln \frac{q_e}{q_m - q_e} = \frac{1}{n} \ln P + \ln K_s$	$\ln \frac{q_e}{q_m - q_e}\ vs\ \ln K_s$	$q_m, K_S\ and\ n$
Toth	$q_e = \frac{q_m K_T P}{(1 + K_T P^n)^{1/n}}$	$\ln \frac{{q_e}^n}{{q_m}^n - {q_e}^n} = n \ln P + n \ln K_T$	$\ln \frac{{q_e}^n}{{q_m}^n - {q_e}^n}\ vs\ \ln P$	$q_m, K_T\ and\ n$

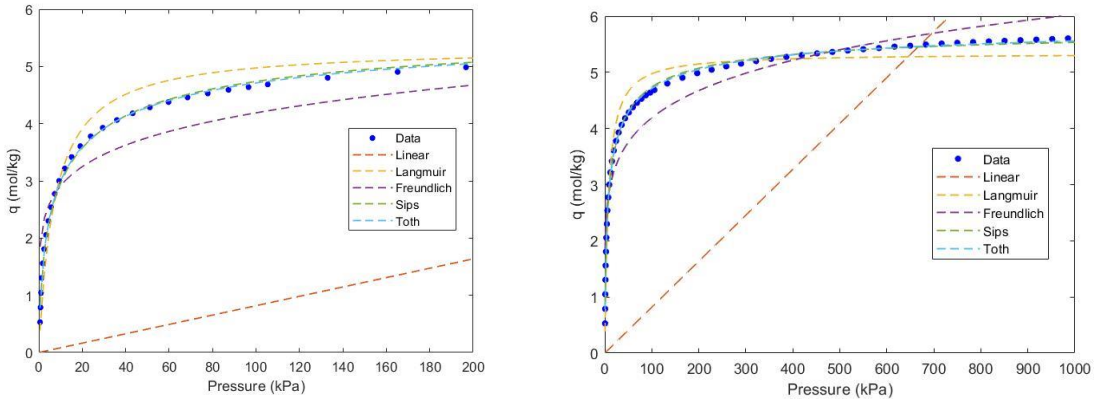

Figure 10 The fitting of experimental adsorption isothermal data of CO_2 with five different adsorption isothermal models.

The Sips isotherm is a combined form of Langmuir and Freundlich models and is used to predict the adsorption in heterogeneous systems. At low adsorbate concentrations, it reduces to the Freundlich isotherm, while at high concentrations, it predicts monolayer adsorption similarly to the Langmuir isotherm. The equation for the Sips isotherm model is given in (3-13), where $_{he}$ is the amount of gas adsorbed in mol/kg, P is the pressure in kPa, q_m is the saturated adsorption quantity, K_s is the adsorption

affinity, and n is a dimensionless parameter that qualitatively characterises the heterogeneity of the adsorbate-adsorbent system.

The Langmuir isotherm model is a good description of the adsorption and desorption process, especially at high partial pressures. Since we are interested in the components that are the main component of the feed gas, the Langmuir model gives a good description of the isotherm. The equation for the Langmuir isotherm model is given in (3-12), where q_e is the amount of gas adsorbed in mol/kg, P is the pressure in kPa, q_m is the saturated adsorption quantity, K_L is the adsorption affinity. The isotherm parameters for the Sips and Langmuir isotherm model for the pure gas adsorption of Zeolites 13X are presented in Table 5.

$$q_e = \frac{q_m * K_s * P_e^{1/n}}{1 + K_s * P_e^{1/n}} \qquad (3\text{-}12)$$

$$q_e = \frac{q_m * K_L * P_e}{1 + K_L * P_e} \qquad (3\text{-}13)$$

Table 5 Isotherm parameters of Sips and Langmuir model on zeolite 13X.

		293 K					**308K**					**323 K**				
		CO_2	*CO*	*H_2*	*N_2*	*CH_4*	*CO_2*	*CO*	*H_2*	*N_2*	*CH_4*	*CO_2*	*CO*	*H_2*	*N_2*	*CH_4*
SIPS	sq_m	5.81	3.87	3.10	3.35	4.34	5.94	3.65	3.25	3.19	4.06	5.80	3.39	2.36	3.04	3.47
	K_s x 10^4	2443.89	73.49	0.65	13.27	15.06	2160.89	44.60	0.55	9.31	12.00	1513.99	27.62	0.59	6.87	8.83
	n	1.59	1.22	0.98	1.03	0.99	1.84	1.17	0.99	1.02	1.00	1.77	1.11	0.97	1.01	0.97
LANGMUIR	sq_m	5.34	3.19	4.30	3.16	4.42	5.14	3.04	3.04	3.02	4.07	4.96	2.90	2.78	2.93	3.71
	K_s x 10^4	1371.10	40.47	0.51	12.04	15.32	3.41	901.76	28.19	0.62	8.89	12.02	3.80	543.49	20.29	0.59

Since the adsorption equilibrium and parameters are temperature dependent, the temperature-dependent form of the Sips and Langmuir isotherm models was studied to be able to estimate the equilibrium for different operating temperatures. Equations (3-14), (3-16) and (3-20) show the temperature dependence of the Sims model parameters, K_S, q_m and n. Equations (3-15) and (3-14) (3-17) show the temperature dependence of the Langmuir model parameters, K_L and q_m.

Equations (3-21) and (3-22) describe the complete temperature-dependent form of the Sips and Langmuir isotherms. The values of the parameters are shown in Table 6.

$$q_m = K_1 + K_2 T \qquad (3\text{-}14)$$

$$q_m = -aT + b \qquad (3\text{-}15)$$

$$K_s^n = K_3 \exp\left(K_4/T\right) \qquad (3\text{-}16)$$

$$K_L = c \exp\left(d/T\right) \qquad (3\text{-}17)$$

$$K_4 = \frac{-\Delta H}{R} \qquad (3\text{-}18)$$

$$d = \frac{-\Delta H}{R} \qquad (3\text{-}19)$$

$$n = K_5 + K_6/T \quad (3\text{-}20)$$

$$q_e = \frac{(K_1 + K_2T) * (K_3 \exp(K_4/T))^{1/(K_5+\frac{K_6}{T})} * P_e^{1/(K_5+\frac{K_6}{T})}}{1 + (K_3 \exp(K_4/T))^{1/(K_5+\frac{K_6}{T})} * P_e^{1/(K_5+\frac{K_6}{T})}} \quad (3\text{-}21)$$

$$q_e = \frac{(-aT + b) * (c \exp(d/T)) * P_e}{1 + (c \exp(d/T)) * P_e} \quad (3\text{-}22)$$

Table 6 Temperature-dependent parameters of Sips and Langmuir model on zeolite 13X.

		Unit	*CO_2*	*CO*	*H_2*	*N_2*	*CH_4*	*O_2*
SIPS	K_1	Mol/kg	6.002	8.609	10.484	6.463	12.914	0.007
	K_2 x 10^4	Mol/ kg K	-4.948	-161.517	-246.211	-106.141	-290.868	-0.1435
	K_3 x 10^6	kPa	0.781	7.974	67.340	3.863	29.625	325.000
	K_4	K	3463.56	1675.44	13.50	1646.03	1158.69	1428.00
	K_5 x 10^3	-	3608.753	5.203	895.646	797.973	752.162	-316.900
	K_6	K	-576.78	357.32	26.85	68.82	72.09	387.80
	DH	kJ/mol	-28.80	-13.93	-0.11	-13.69	-9.63	-11.87
LANGMUIR	a x 10^3	Mol/ kg K	12,47	9,69	50,72	7,57	23,61	38,81
	b	Mol/ kg	8,99	6,03	19,00	5,37	11,34	15,70
	c x 10^7	kPa ^--1	67,50	23,94	2649,90	22,98	110,43	0,22
	d	K	2912,40	2177,89	-469,53	1834,79	1444,93	2876,24
	DH	kJ/mol	-24,20	-18,10	3,90	-15,25	-12,01	-23,90

The feed gas of BFG+BOFG is a mixture of different gas components, which results in competition and interaction during the adsorption process. Therefore, the models used for single component systems are insufficient for multi-component adsorption systems. The single-component Sips isotherm model is modified to a multi-component adsorption model called the extended sips isotherm model as given in equation (3-23), describing the adsorption capacity of component i in a gas mixture.

$$q_{e,i} = \frac{q_{m,i} * K_{s,i} * P_{e,i}^{1/n_i}}{1 + \sum_{j=1}^{m} K_{s,j} * P_{e,j}^{1/n_j}} \quad (3\text{-}23)$$

$$q_e = \frac{q_{m,i} * K_{L,i} * P_{e,i}}{1 + \sum_{j=1}^{m} K_{L,j} * P_{e,j}} \quad (3\text{-}24)$$

Considering the pure multiple component Sips adsorption models and the composition and temperature of the feed gas, an extended sips isotherm model was developed. Figure 11a represents the adsorption isotherm model for the pure gas components at 288K, while Figure 11b represents the model of a gas mixture (feed gas) at 288K, which is significantly different.

(a) **(b)**

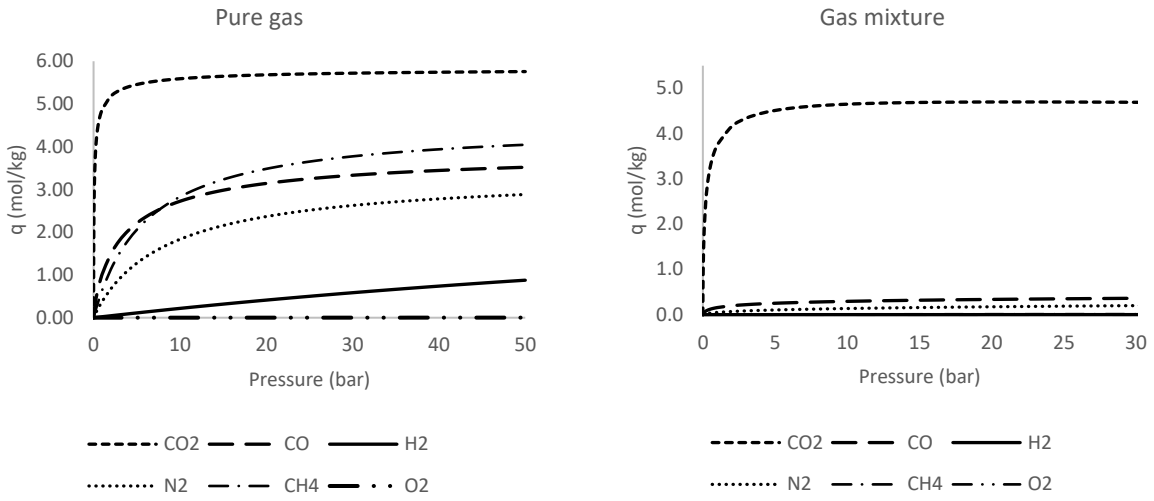

Figure 11: Adsorption equilibria of the pure gasses and gas mixture of BFG+BOFG at 288K.

Although the sips and the Langmuir isotherm models have been studied and their parameters determined, this study only continued with the Langmuir isotherm model because the Sips isotherm model was found not to work in Aspen Adsorption™. Also, the Langmuir isothermal model is considered in its simplest, temperature-independent form, as shown in equation (3-13).

Based on this equilibrium model, some important design factors of the PSA process can be estimated. These parameters are the working capacity of the adsorbent in the operating temperature and pressure range, the selectivity of component i over other components and the purity of the desired gas component.

Equation (3-25) describes the working capacity of component i in a gas mixture, where $q_{i,HP}$ represents the adsorbed amount (mol/kg) of component i at equilibrium at high pressure and $q_{i,LP}$ represents the adsorbed amount (mol/kg) of i at equilibrium at low pressure. Equation (3-26) described the selectivity of gas component i over gas component j, which is the ratio of the working capacities of the two gas components. Equation (3-27) describes the purity of the desired component (CO_2) in the product stream with m components at the equilibrium. Table 7 presents the product stream's working capacities, selectivity, and purity at a pressure range of 1- 15 bar based on Figure 11 b.

$$W_i = \Delta q_i = q_{i,HP} - q_{i,LP} \tag{3-25}$$

$$\alpha_{i/j} = \frac{W_i}{W_j} \tag{3-26}$$

$$Y_{CO_2} = \frac{n_{CO2}}{\sum_i^m n_i} \tag{3-27}$$

Table 7 The working capacity, selectivity, and purity of the product stream at a pressure range of 1-15 bar.

	CO_2	CO	H_2	N_2	CH_4	O_2
Working capacity	0.934	0.162	0.001	0.108	0.006	3.24E-07
Selectivity of CO_2 over component	1.0	5.7	1035.6	8.7	150.9	2.9E+06
Purity of CO_2	77%					

3.1.4 Energy Balance

The energy balance is non-isothermal, and three factors affect the energy balance. These are the gas-phase energy balance, the solid phase energy balance, and the wall energy balance, described in equations (3-28), (3-29) and (3-30), respectively.

As for the mass balance, for the energy balance, the axial energy transfers are neglected. The non-isothermal with no conduction model describes the energy changes in the adsorbing bed. These are the energy balance equations' axial thermal conduction for the fluid and solid phases.

The complete gas phase energy balance, as given in equation (3-28), consists of 6 terms: axial thermal conduction (this is neglected) , convection, Compression, thermal accumulation in the gas phase, heat transfer between gas and solid and heat transfer between gas and the internal wall of the bed.

$$-k_g\varepsilon_b\frac{\P^2T_g}{\P x^2}+C_{vg}v_g\rho_g\frac{\P T_g}{\P x}+P\frac{\P v_g}{\P x}+C_{vg}\rho_g\varepsilon_t\frac{\P T_g}{\P t}+H_sa_p(T_g-T_s)+\frac{A_{Hi}}{V_{Hi}}(T_g-T_w)=0 \tag{3-28}$$

Solid phase energy balance consists of 4 terms: axial thermal conduction, solid phase thermal accumulation, thermal accumulation by the heat of adsorption and heat transfer between gas and solid. The energy balance is given in equation (3-29), where k_s is the solid thermal conductivity, C_{ps} is the solid heat capacity, and ΔH_i is the heat of adsorption of gas component i.

$$-k_s\frac{\P^2T_s}{\P x^2}+C_{Ps}\rho_b\frac{\P T_s}{\P t}+\rho_b\sum_i\left(\Delta H_i\frac{\P Q_i}{\P t}\right)-H_sa_p(T_g-T_s)=0 \tag{3-29}$$

The last component of the energy model is the wall energy balance of 4 terms, given in equation (3-30).

$$-k_w\frac{\P^2T_w}{\P x^2}+C_{Pw}\rho_w\frac{\P T_w}{\P t}-H_w\frac{A_{Hi}}{V_{Ho}}(T_g-T_w)+H_{amb}\frac{A_{Ho}}{V_{Ho}}(T_w-T_{amb})=0 \tag{3-30}$$

In the above described three energy balances, Here k_g, k_s and $k_w$represent respectively the gas, solid and wall thermal conductivity, T_g, T_s, and T_w are respectively the temperatures of the gas, solid and wall, C_{vg}, C_{ps}, and C_{pw} are the gas, solid and wall material heat capacity, H_s, H_w and H_{amb} are respectively the gas to solid and gas to wall and wall to environment heat transfer coefficients, a_p

represents the specific external area of the particles and A_{Hi} and V_{Hi} are the wall internal area and volume, and A_{Ho} and V_{Ho} are the wall external area and volume where the heat transfer takes place.

3.1.5 Flow implementation

To model the flows in the flowsheet in Aspen Adsorption™, the flowrate through the control valves is modelled using the linear CV valve model, where the flowrate is linearly determined by the valve coefficient (CV) and the pressure drop through the valve. See equation (3-31). Using the control valves, the flow rate changes with the change in the pressure drop. These pressure changes are significant to simulate the PSA cycle so that the flow rate is not kept constant.

$$Q = CV\ \Delta P = CV(P_{in} - P_{out}) \tag{3-31}$$

3.2 Model validation

The model described in chapter 3.1 is verified for its correctness by validation against two separate systems that studied the separation of CO_2 from a multi-component gas mixture. The two systems used for this validation are the separation of CO_2 from a multi-component gas mixture. The gas mixture was led through an adsorbent bed of zeolite 13X by Cavenati et al. [117] and hydrogen purification from a five-component gas using a layered bed packed with activated carbon and zeolite 5A by Xiao et al. [118]. These studies include a wide range of operation boundaries, such as feed gas composition, including CH_4, CO, CO_2, H_2 and N_2. The pressure range of both systems varied between 2.5 and 6.5 bar, and both systems considered ambient temperatures.

3.2.1 Carbon dioxide separation using zeolite 13X

For the first validation of the model, the experimental breakthrough data from Cavenati et al. [117] [117] is used. This study includes a gas mixture with 70 mol % CH_4, 20 mol % CO_2, and 10 mol % N_2. The gas mixture was led through an adsorbent zeolite bed 13X by Cavenati et al. The experimental breakthrough curves from that study were simulated using the model in chapter 3.1. Breakthrough curves of the gas mixture were simulated to reproduce the data obtained from the experiment by Cavenati et al. Since the study of Cavenati et al. also uses zeolite 13X as adsorbed material in the packed bed, the adsorption isotherm data (Table 6 of this study) and adsorption kinetics (Table 3 of this study) were used. The column dimensions and properties of the adsorbent zeolite 13X were used as described by Cavenati et al. These inputs are summarised in

Table 8.

Table 8: Model inputs (CH_4-CO_2-N_2-zeolite13X system)

Description	*Unit*	*Value*
Pressure	Bar	2.5
Temperature	K	300
Height of the adsorbent layer	m	0.2
The internal diameter of the bed	m	0.019
Inter-particle voidage		0.33
Intra-particle voidage		0.54
Adsorbent bulk density	Kg/m^3	756
Particle radius	m	$0.8' 10^{-3}$

To run the simulation in Aspen Adsorption™, the adsorbent bed must be initialised for the gas content. It is impossible to set the column to be empty at the initial conditions; it was assumed that the bed was utterly filled with N_2 at $t = 0$. This is also done in the work of Cavenati et al. By doing this, Breakthrough curves similar to the experimental data were obtained. A comparison of the literature and model results for the breakthrough profiles of concentration for the three gases at the end of the adsorption bed is shown in Figure 12.

The curves obtained from the model have an excessive slope compared to the experimental curves, which means that they reach their equilibrium state more quickly. This effect is visible with the curve of methane and CO_2 and is less noticeable with N_2 because the curve of N_2 shows less variation in the direction of the y-axis. This is because the slope of the curve changes due to the adsorption limit (kinetic effect) of the adsorbent and the temperature rise during the adsorption step (temperature effect). This second effect is not included in the model because there is the isothermal version of the Langmuir adsorption isotherm model used, although the energy balance is non-isothermal. Which means that the adsorption behaviour of the bed does not change with the temperature change in the bed. In reality, the increased temperature during the adsorption process affects the kinetics of the gas particles in the adsorber band. Namely, the diffusion is accelerated, resulting in a steeper curve due to a faster diffusion. A second reason for quickly reaching equilibrium is that in the kinetic model, only the diffusion through macropores has been included, and the diffusion in the micropores has been neglected. This makes the kinetics faster in the model than it is in reality.

(a)

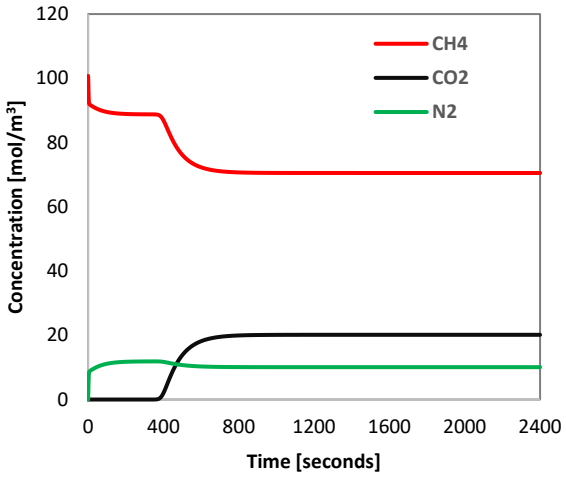

(b)

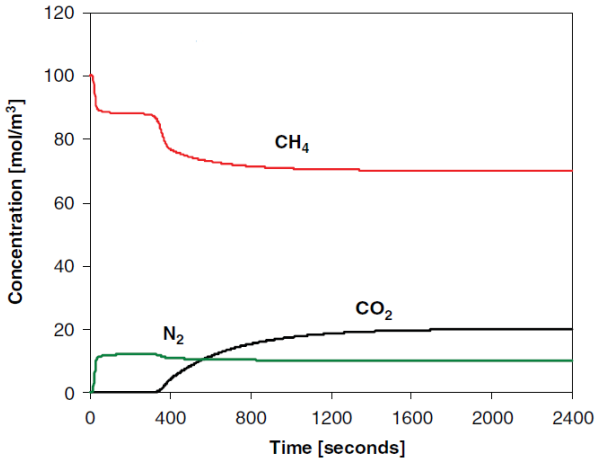

Figure 12: Breakthrough curves for zeolite 13X obtained with Aspen Adsorption™ (a) compared with the experimental data (b) of Cavenati et al. [117] for the gas mixture of CH_4, CO_2 and N_2 with molar fractions of 70%, 20% and 10% respectively.

3.2.2 Hydrogen purification using activated carbon and zeolite 5A

For the second validation of the model from this study, the model was used to simulate the breakthrough curves as obtained by Xiao et al. [118], where the five component feed gas containing H_2, CO_2, CH_4, CO and N_2 (38, 50, 1, 1, 10 vol.%) was adsorbed in a packed bed under the pressure of 6,5bar. The breakthrough curves for two beds using activated carbon and zeolite 5A were obtained.

The experimental breakthrough curves from that study were simulated using the model in chapter 3.1. Breakthrough curves of the gas mixture were simulated to reproduce the data obtained from the experiment by Xiao et al. Since the study of Xiao et al. does not use zeolite 13X, the adsorption isotherm data and mass transfer coefficients from the article were used for both activated carbon and zeolite 5A simulations (see Table 9).

*Table **9** Extended Langmuir adsorption parameters and mass transfer coefficients for the (CH_4-CO-CO_2-H_2-N_2-AC-zeolite 5A system).*

		k_1, [mol/kg]	k_2, [mol/kg/K]	k_3, [1/bar]	k_4, [K]	ΔH_i, [cal/mol]	MTC, [1/s]
Activated carbon	H_2	16.943	−0.021	6.248E−5	1229	2880	0.7
	CH_4	23.86	−0.05621	3.478E−3	1159	4290	0.195
	CO	33.85	−0.09072	2.311E−4	1751	4300	0.15
	N_2	1.6441	−0.00073	0.0545	326	1660	0.261
	CO_2	28.7973	−0.07	0.01	1030	5240	0.0355
Zeolite 5A	H_2	4.314	−0.0106	0.002515	458	2800	0.7
	CH_4	5.833	−0.01192	6.0507E−4	1731	5400	0.147
	CO	11.8454	−0.0313	0.0202	763	5300	0.063
	N_2	4.8133	−0.00668	5.695E−4	1531	5470	0.099
	CO_2	10.03	−0.01858	1.5781	207	9330	0.0135

The adsorption behaviour of the gasses was described by the extended Langmuir isotherm. The column dimensions and properties of both adsorbents were used as described in the article. These inputs are summarised in Table 10.

Table 10 Model inputs for (CH_4-CO-CO_2-H_2-N_2-AC-zeolite 5A system)

Description	*Unit*	*Value*	
		Activated carbon	Zeolite 5A
Pressure	Bar	6.5	
Temperature	K	398	
Height of the adsorbent layer	m	1	
The internal diameter of the bed	m	0.0371	
Inter-particle voidage	-	0.433	0,357
Bed density	kg/m^3	482	764
Adsorbent bulk density	kg/m^3	850	1160

Figure 13 compares the literature and model results for the breakthrough profiles of concentration for the five gases at the end of the adsorption bed existing activated carbon, and Figure 14 compares the curves for zeolite 5A. The CO, CO_2 and CH_4 curves agree well with each other. The main difference is that the curve of H_2 starts to fall faster in the simulation, and the curve of N_2 rises faster. The last part of the H_2 and N_2 curves are similar. This effect is more visible with the activated carbon than with the zeolite.

A explanation of this effect is that the radial material dispersion has been neglected in the model, which is present in reality. Due to the neglect of this dispersion, the gas components that appear first in the breakthrough curves leave the bed more quickly. This effect will be negligible if the feed flow rate is reduced.

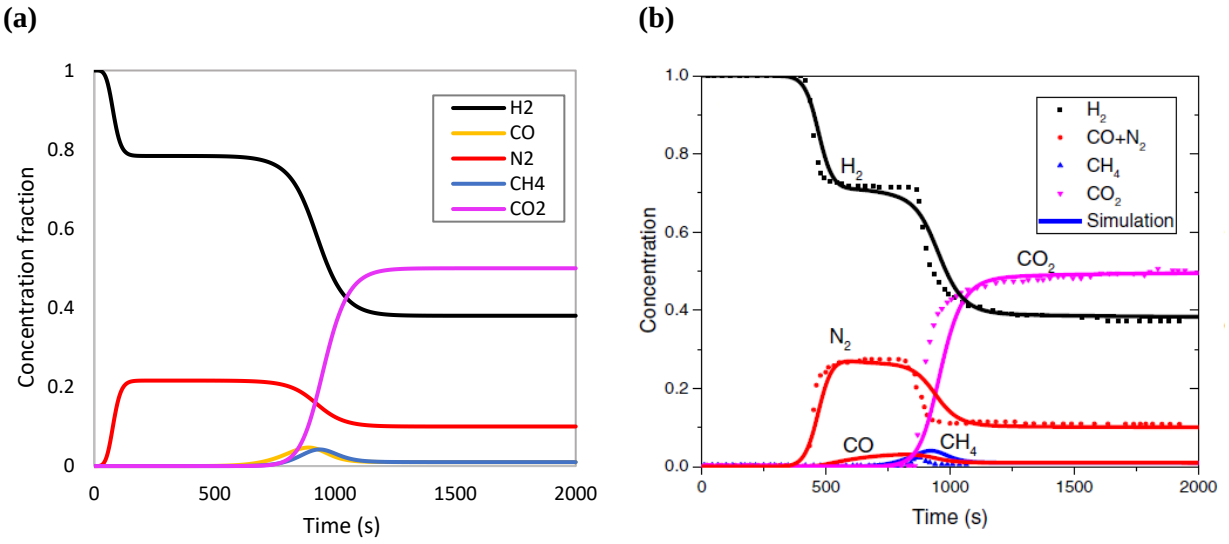

Figure 13 Breakthrough curves for activated carbon obtained with Aspen Adsorption™ (a) compared with the experimental data (b) of Xiao et al. [118] for the gas mixture of CH_4, CO, CO_2, H_2 and N_2.

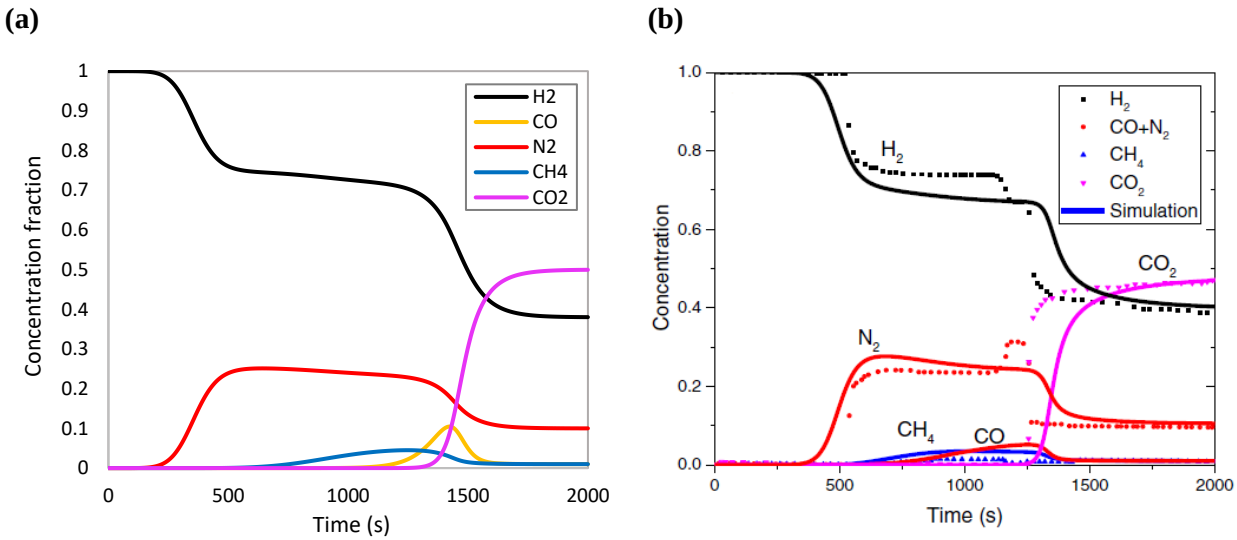

Figure 14 Breakthrough curves for zeolite 5A obtained with Aspen Adsorption™ (a) compared with the experimental data (b) of Xiao et al. [118] for the gas mixture of CH_4, CO, CO_2, H_2 and N_2.

For the adsorption process, a PSA cycle is how much of a particular gas is finally adsorbed in each time interval at breakthrough point. Although there are minor differences in the shape of the breakthrough curve, the final molar fraction of the gasses at the end of its breakthrough curves are almost the same in the model and in the experimental breakthrough experiments. Looking at this aspect, the final breakthrough concentrations of the model correspond to the experimental concentrations, confirming the validity of the model developed in this study.

3.3 Adsorption-desorption cycle design and dynamic simulation for the base case

Using the above validated sub-models to simulate the PSA, a simple adsorption-desorption cycle is constructed that consists of only two steps, namely adsorption and desorption.

- Step 1: During this step, the feed gas is fed to the adsorbing bed, which increases the bed's pressure to P_H. Adsorption happens in de bed at this temperature; CO_2 adsorbs more effectively than the other gas components, according to the multi-component gas adsorption isotherm model.
- Step 2: The pressure is decreased in the adsorbing bed, which results in desorption of the gas components. Since the heat of adsorption is highest for CO_2, CO_2 desorbs not easily compared to the other components. The amount of desorbed CO_2 depends on the pressure of this desorption step.

This single bed two steps model is the base case model that will be further optimised in the subsequent parameter study.

3.3.1 Base case

The base case model processes the raw BFG into a gas mixture of 25% CO_2. In The rough, the BFG is first pressurised to 15 bar, and a temperature of 288K is maintained. With This, the feed gas is fed to the adsorption bed, consisting of Zeolite 13X; the dimensions and other column properties are summarised in Table 11. The bed is divided into 50 discretisation volumes. The adsorbing bed uses the temperature independent Langmuir adsorption isotherm model, which is insensitive to temperature change. Although in the mathematical description of the model, the temperature dependent sips model was suggested as the most suitable model followed by the Langmuir, in the base case the temperature independent Langmuir model was continued. Because the other two models failed to work in the Aspen Adsorption™ software. This is one of the limitations of the software which is discussed further in the discussion chapter.

The base case model has a two steps cycle, where during the adsorption the bed is fed with feed gas till it is fully saturated with CO_2. The duration of the desorption step is the same as the adsorption step. Other mass transfer and heat transfer properties to be used for the adsorbing bed are summarised in Table 11.

Table 11 Parameters used in PSA simulation of the base case.

PARAMETER	VALUE
Column properties	
Length, L [m]	12
Internal bed diameter, d_{bi} [m]	1.0
Particle radius, r_p [m]	1.0 ×10-3
Bed voidage, ε_b [–]	0.33
Particle voidage, ε_p [–]	0.54
Adsorbent bulk density, ρ_p [kg m^{-3}]	756.00
Bed wall thickness [m]	0.0024
Wall density [kg m^{-3}]	7830.0
Thermo-physical properties	
Universal gas constant, R [m^3 Pa mol^{-1} K^{-1}]	8.314
Adsorbent-specific heat capacity[MJ/kg/K]	0.0487
Wall-specific heat capacity [J/kg/K]	502.8
Wall thermal conductivity [W/m/K]	16.0
Heat transfer coefficient (wall to ambient) [MW/m2/K]	1.0 ×10-9
Heat transfer coefficient (gas to solid) [MW/m2/K]	1
Heat transfer coefficient (gas to the wall) [MW/m2/K]	1.0 ×10-6
The heat of adsorption CO_2, $\Delta H_C O_2$ [kJ mol^{-1}]	-24.20
The heat of adsorption CO, ΔH_{CO} [kJ mol^{-1}]	-18.10
The heat of adsorption N_2, ΔHN_2 [kJ mol^{-1}]	-15.25
The heat of adsorption H_2, ΔHH_2 [kJ mol^{-1}]	-0.11
The heat of adsorption O_2, ΔHO_2 [kJ mol^{-1}]	-11.87
The heat of adsorption CH_4, ΔHCH_4 [kJ mol^{-1}]	-12.01
Mass transfer coefficient, CO_2, MTC_{CO2} [s^{-1}]	0.0137
Mass transfer coefficient, CO, MTC_{co} [s^{-1}]	0.0172
Mass transfer coefficient, N_2, MTC_{N2} [s^{-1}]	0.0172
Mass transfer coefficient, H_2, MTC_{H2} [s^{-1}]	0.0641
Mass transfer coefficient, O_2, MTC_{O2} [s^{-1}]	0.0228
Mass transfer coefficient, CH_4, MTC_{CH4} [s^{-1}]	0.0227
Operating conditions	
Feed gas pressure P_{ferd} [bar]	1
High-pressure P_H [bar]	15
Low pressure [bar]	0.1
Feed composition (CO_2/ CO/ N_2/ H_2/O_2/CH_4)	0.2535/ 0.2954/ 0.3687/ 0.0525/ 0.0066/ 0.0109
Feed temperature, T_{feed} [K]	288
Ambiant temperature [K]	298.15
Duration of steps	
Adsorption time [s]	1600
Desorption time [s]	1600

The breakthrough curves of the different gas components during the adsorption step are presented in Figure 15. At the start of the adsorption step, the bed is filled with 100% N_2 gas. Therefore, this is the first gas that comes out of the bed. The curve of N_2 gas then falls as there is an N_2 adsorption plate in the bed. For the other components, there is no breakthrough at the start of the adsorption step, and the components appear one by one at the level of the end of the bed. The breakthrough time of each gas component depends on the fraction of the gas in the feed gas and its adsorption properties.

The adsorption bed is stopped ideally at the point when the bed is completely saturated with CO_2 gas; this time is called the breakthrough time for CO_2. In the next desorption step, the adsorbed CO_2 is recovered because the pressure in the bed is reduced to 0.1 bar.

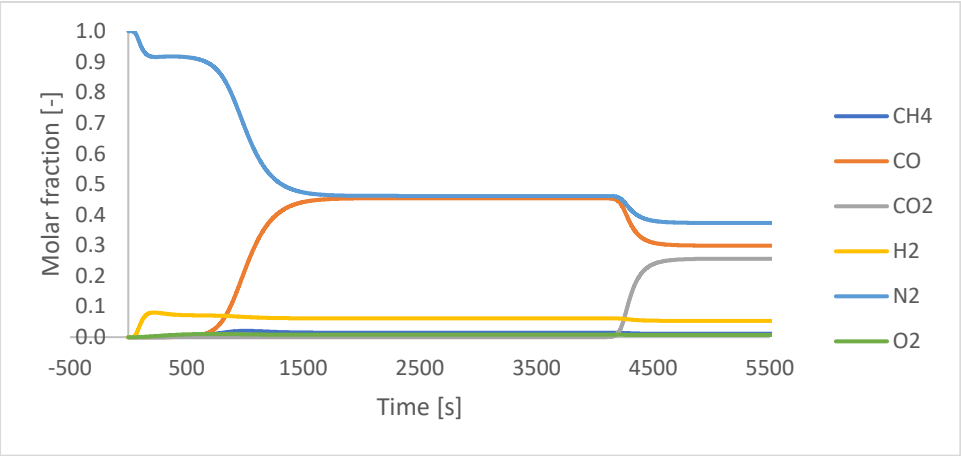

Figure 15 Breakthrough curves of the different gas components in the feed gas in the base case.

3.3.2 Performance indicators of the PSA cycle

The dynamic results of the bed are converted into performance indicators of the steady state.

1) Purity

Purity is one of the key performance indicators of the carbon capture process. The excellent separation of CO_2 from other gas components results in a higher purity of the CO_2 in the CO_2-rich stream. The purity of CO_2 was calculated in the CO_2-rich stream, which is the end of the blowdown step, using equation (3-32).

$$CO_2\ purity = \frac{Amount\ of\ CO_2\ in\ product\ stream}{amount\ of\ \ all\ gas\ components\ in\ product\ stream} = \frac{\dot{n}_{CO2}[kmol/s]}{\sum_i \dot{n}_i\ [kmol/s]} \quad (3\text{-}32)$$

2) Recovery

Recovery is another important performance indicator of a carbon capture process. A high recovery during a PSA means that all CO_2 present in the gas mixtures to be separated has ended up in the CO_2-rich stream. The recovery of CO_2 of the PSA was calculated by considering the amount of CO_2 in the feed, CO_2 lean and CO_2 rich streams (see Figure 37) in one PSA cycle when the steady state is reached, using equation (3-33). Since the recovery is not 100%, there is some CO_2 lost in the CO_2 lean stream(s); this amount is calculated using equation (3-34). The sum of the recovery and losses should be 100%.

$$CO_2\ recovery = \frac{Amount\ of\ CO_2\ produced\ (1\ cycle)}{Amount\ of\ CO_2\ imput\ (1\ cycle)} = \frac{n_{CO2\ ,product}\ [kmol]}{n_{CO2\ ,feed}\ [kmol]} \quad (3\text{-}33)$$

$$CO_2\ lost = \frac{Amount\ of\ CO_2\ lost\ (1\ cycle)}{Amount\ of\ CO_2\ imput\ (1\ cycle)} = \frac{n_{CO2\ ,waste}\ [kmol]}{n_{CO2\ ,feed}\ [kmol]} \quad (3\text{-}34)$$

3.4 Parametric study and model optimisation

A parameter study is a crucial part of model optimisation. Therefore, the following parameter study was carried out to investigate the effect of each parameter on the performance of the PSA cycle and to find the correct values that lead to maximum purity and recovery of CO_2. The effect of each parameter has been investigated independently of the other parameters, i.e. the other parameters are kept constant while one parameter is varied.

In this parameter study, the following parameters and their effect were investigated: the number of discretisation volumes, feed pressure, adsorption bed dimension, adsorption bed length and diameter, particle size, duration of different steps, and feed temperature.

3.4.1 Nr of discretisation volumes variation

The accuracy of the differentiation during the simulation is increased by increasing the nr of discretisation volumes (nr of nodes in the adsorption bed). This accurate differentiation can result in accurate results of the PSA cycle, so it can directly affect the purity and recovery of CO_2.

To investigate the sensitivity of the performance indicators for the number of discretisation volumes, different simulations were performed with different numbers of discretisation volumes.
From Figure 16, we can deduce that the CO_2 purity and the CO_2 recovery remain almost constant in the chosen range of the discretisation volumes. The purity is $94.4 \mp 0.2\ \%_{mols}$, and the recovery is $66.1 \mp 0.5\ \%$. Since this variation is minimal, 50 was chosen for the number of discretisation volumes.

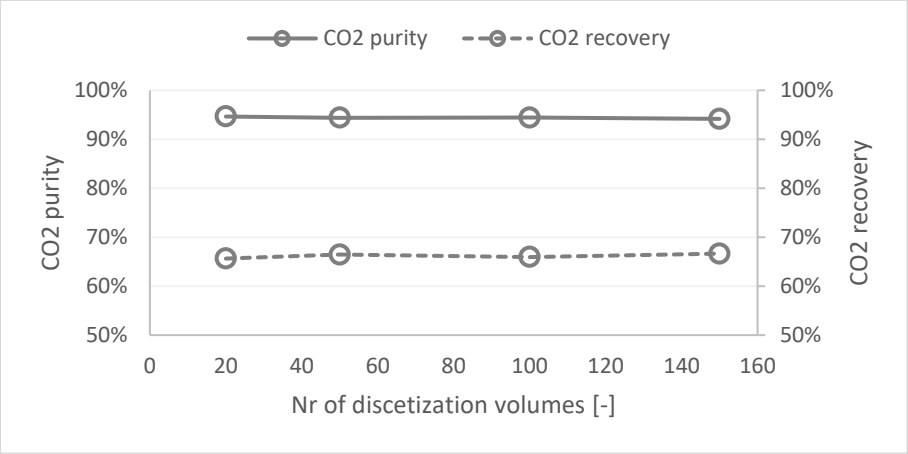

Figure 16 The CO_2 purity and recovery change with the changing number of discretisation volumes of the adsorption bed.

Table 12 The values of the parameters used for the parametric study of the discretisation volumes.

Bed division	*Pressure*		*Temperature*	*Bed size*		*Particle size*	*Time*	
DV	PH	PL	T	Length	Diameter	Diameter	Ads	Des
[-]	[bar]	[bar]	[K]	[m]	[m]	[mm]	[s]	[s]
20	15	0.1	288	12	1	2	1600	1600
50	15	0.1	288	12	1	2	1600	1600
70	15	0.1	288	12	1	2	1600	1600
100	15	0.1	288	12	1	2	1600	1600
150	15	0.1	288	12	1	2	1600	1600

3.4.2 Pressure range variation

The shape of the adsorption equilibrium isotherm shows that the PSA adsorption cycle produces different results when the pressure range of the PSA cycle is varied. The maximum amount of CO_2 adsorbed at a pressure of about 15 bar. The lowest pressure in the cycle means that the two values are chosen: 1 bar to 0.1 bar, which is the atmospheric pressure and the vacuum representation.

Two simulations were performed for the pressure range's effect on the (V)PSA cycle's performance indicators, the results of which are shown in Figure 17. This figure shows that both the purity and the recovery are high when the pressure range is more extensive and if the P_L is low because, at lower pressures, more desorption takes place. As a result, the bed's capacity for the adsorption of CO_2 is high in the case of the 15 bar to 0.1 bar range. Which means that there is more CO_2 adsorbed and desorbed in the bed compared to other gas components resulting higher CO_2 purity. In Figure 18 are several cycles showing the total amount of CO_2 adsorbed in the bed during the Steady State. This figure clarifies that the bed capacity is small in the case of desorption up to 1 bar, so both the purity and the recovery are lower. For this reason, 15 and 0.1 bar are chosen as the pressure range.

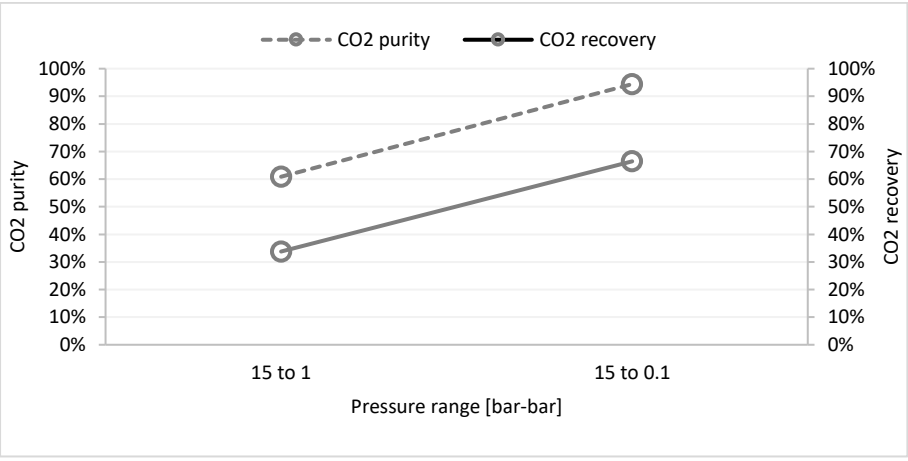

Figure 17 The CO_2 purity and recovery change with the changing pressure range of the PSA cycle.

There is a remarkable difference between the adsorption and desorption patterns of CO_2 for these two different pressure ranges. In the case of the pressure range of 15 to 0.1 bar, insufficient desorption has taken place. This is because in the base case it is assumed that the adsorption and desorption time is the same. Further optimization takes place for this adsorption and desorption time.

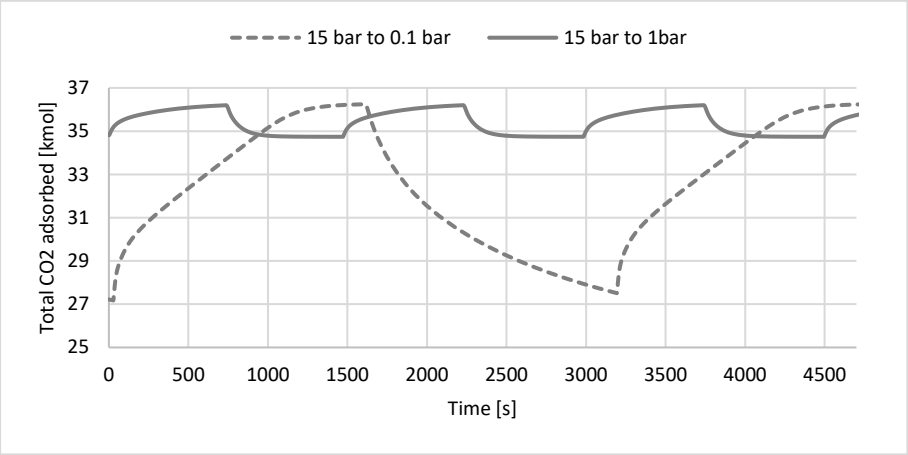

Figure 18 Several cycles showing the total amount of CO_2 adsorbed in the bed during the SteadyState for the different pressure ranges during the PSA cycle.

Table 13 The values of the parameters used for the parametric study of the pressure range of the PSA cycle.

Pressure		*Temperature*	*Bed size*		*Particle size*	*Time*		*Bed division*
PH	PL	T	Length	Diameter	Diameter	Ads	Des	DV
[bar]	[bar]	[K]	[m]	[m]	[mm]	[s]	[s]	[-]
15	1	288	12	1	2	754	754	50
15	0.1	288	5	0.81	1.5	1600	1600	50

3.4.3 Particle size variation

The particle size has an essential function in adsorption and desorption kinetics. Following the linear driving force (equation (3-4)) principle for the adsorption kinetics in the mass transfer coefficient (equation (3-5)) is inversely proportional to the square of the particle radius. Therefore, the kinetics expressed in the mass transfer coefficient is more prominent for smaller particles. In addition, smaller particles also have a larger specific surface area and a high surface area is often seen as an essential characteristic of improving the adsorption capacity.

The effect of the particle size on the performance indicator has been analysed and shown in Figure 19. The figure shows that the CO_2 purity increases with the size of the particles.

Since the surface area is more significant for smaller particles, the adsorption capacity of the bed is also larger for smaller particles. Figure 20 shows the difference in the bed CO_2 adsorption capacity for the

different particles. Due to a large CO_2 adsorption capacity, the CO_2 purity is also greater with small particles and decreases as the particles become larger. In contrast, the CO_2 recovery is greater with large particles because the pressure drop is smaller in a bed filled with large particles. The pressure drop for the different particle sizes is shown in Figure 21.

Because the purity does not increase much $(+0.75\%_{mols})$ when the particle diameter of 2 mm descreases to 4 mm and the recovery increases sharply (-14.1%) when the particle diameter increases to 1 mm, this particle size has been chosen as the optimal value.

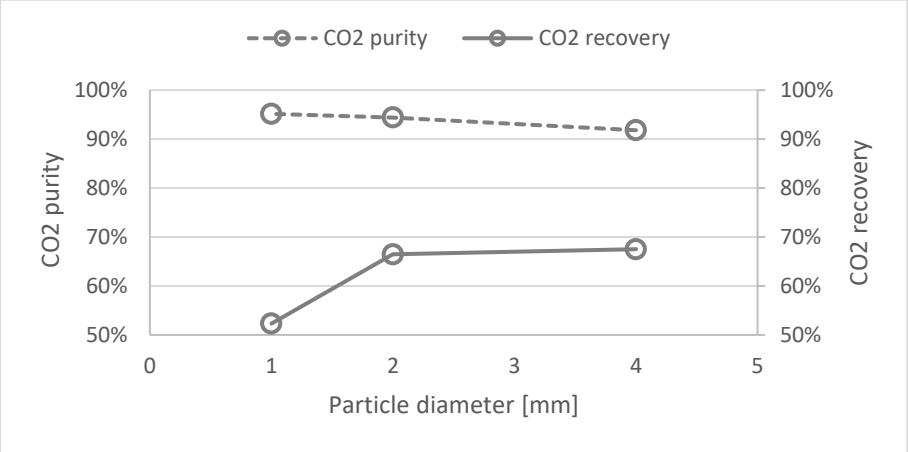

Figure 19 The CO_2 purity and recovery change with the particle radius change.

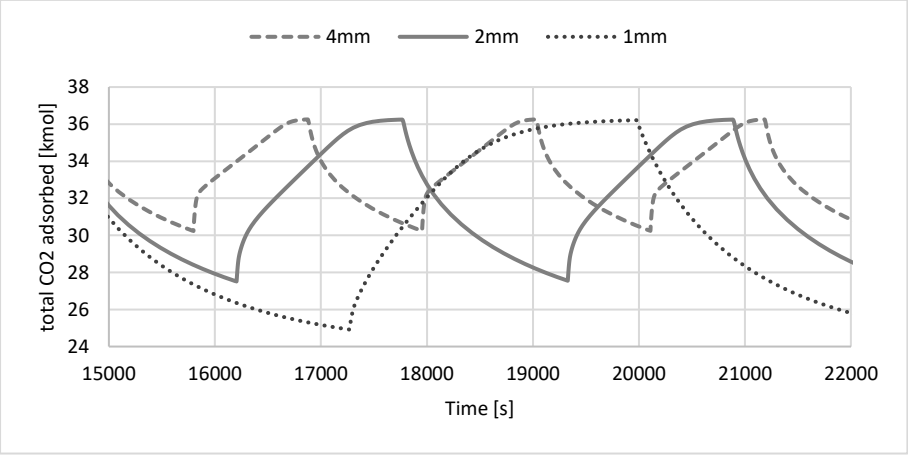

Figure 20 Several cycles showing the total amount of CO_2 adsorbed in the bed during the SteadyState for the varied sizes of the particles.

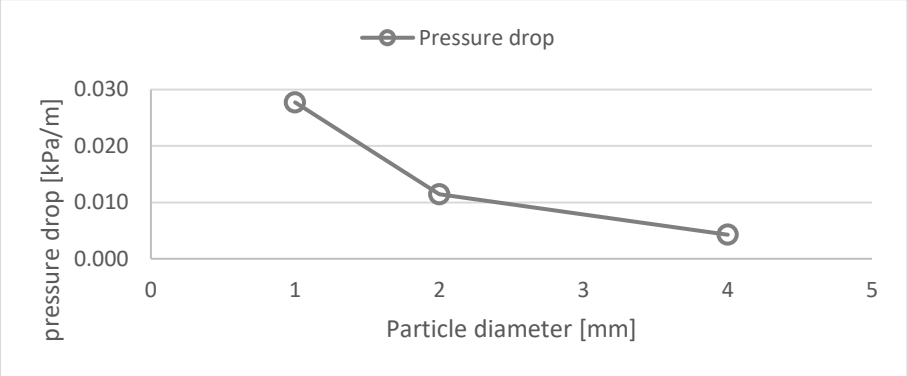

Figure 21 The pressure drop in the adsorption column when the adsorbing bed is filled with varied sizes of adsorbing particles.

Table 14 The values of the parameters used for the parametric study of the particle size.

Particle size	*Pressure*		*Temperature*	*Bed size*		*Time*		*Bed division*
Diameter	PH	PL	T	Length	Diameter	Ads	Des	DV
[mm]	[bar]	[bar]	[K]	[m]	[m]	[s]	[s]	[-]
1.0	15	0.1	288	12	1	2690	2690	50
2.0	15	0.1	288	12	1	1600	1600	50
4.0	15	0.1	288	12	1	1074	1074	50

3.4.4 Adsorption bed size variation

The total bed volume is very important parameter for the performance of the adsorption and desorption behavior of a bed. For this parameter study it was previously chosen to keep the ratio of the length of the bed to its diameter constant, in this case it is equal to 12. Figure 22 illustrates that the CO_2 purity undergoes small change with a change in the bed dimension. The CO_2 purity increases with decreasing bed length and diameter. The CO_2 recovery also increases when a smaller and thinner bed is used. A large bed dimension also means that the void volume in the bed is larger. As a result, more of the unwanted gas components remain in this void bed volume. The gases in this void bed volume end up in the CO_2 rich stream during the desorption step and in this way lower the CO_2 purity.

Also the recovery is low for larger beds because more and more CO_2 from the bed slips during the adsorption step. The slippage of CO_2 out of the bed starts when the last layers in the bed are filled and if the volume of these layers is larger (as a result of the size diameter of the bed), it takes longer to fill these layers. In the same time, more CO_2 has slipped out of the bed and is lost, resulting in a reduction in recovery.

The purity and recovery are highest in the case of a 6 m long bed with a diameter of 0.5 m, but in that case 1474 beds are required to be able to process the entire feed gas (see Figure 23). This quantity is much larger than in the case of 9 m long bed. That is why the second best option was chosen, namely a bed of 9 m long and 0.75 m wide.

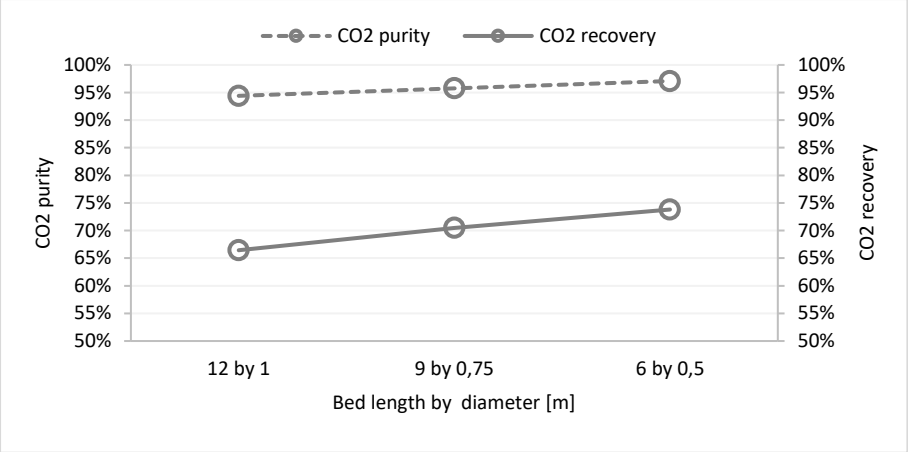

Figure 22 The CO_2 purity and recovery change with the changing bed size.

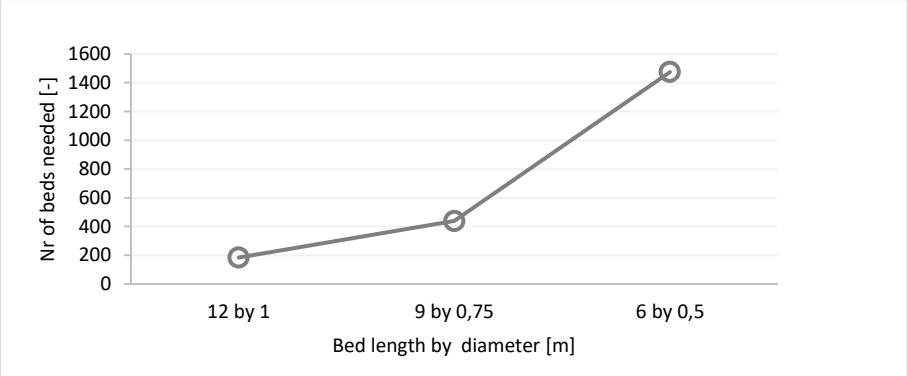

Figure 23 The nr of adsorbing beds needed to process the total feed gas using the different adsorption bed sizes.

Table 15 The values of the parameters used for the parametric study of the bed size.

Bed size		*Pressure*		*Temperature*	*Particle size*	*Time*		*Bed division*
Length	Diameter	PH	PL	T	Diameter	Ads	Des	DV
[m]	[m]	[bar]	[bar]	[K]	[mm]	[s]	[s]	[-]
12.0	1.0	15	0.1	288	2	1600	1660	50
9.0	0.75	15	0.1	288	2	1665	1665	50
6.0	0.5	15	0.1	288	2	1791	1791	50

3.4.5 Adsorption time variation

During the adsorption time, CO_2 and other gas components are adsorbed in the bed. The adsorbed amount of CO_2 reaches a maximum value ($5.1\ \text{kmol kg}^{-1}\text{of adsorbant}$) at an adsorption time of 1660 seconds. When the adsorption time is decreased, more of the upper layers in the bed does not reach this maximum amount of CO_2 adsorbed, which results in a decreasing bed CO_2 capacity. Figure 24 illustrates the decreasing CO_2 purity due to decreasing bed CO_2 capacity and decreasing adsorption time. The CO_2 recovery, on the other hand, decreases with the increasing adsorption time because more

CO_2 is lost to the CO_2 lean stream. This happens because when filling the highest layers of beds, more CO_2 slips out of bed and can no longer be recovered.

Because the CO_2 purity by only (1.6%$_{mols}$) when the maximum adsorption time is decreased by 370 seconds and recovery increases much more (9.1%), the adsorption time is reduced to 1290 seconds instead of the maximum adsorption time of 1660 seconds. By doing this, 22% of the adsorption time is saved.

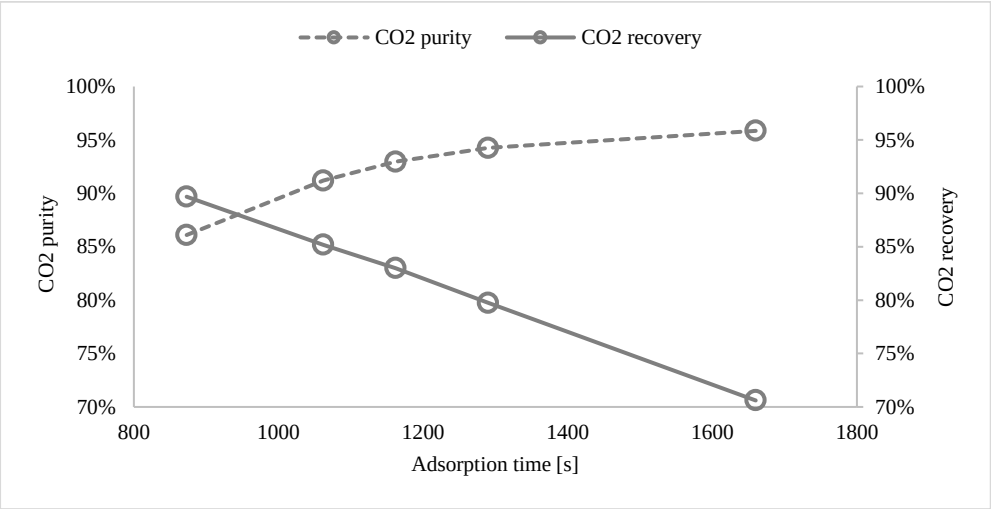

Figure 24 The CO_2 purity and recovery change with the changing adsorption time.

Table 16 The values of the parameters used for the parametric study of the adsorption time.

Time		*Bed size*		*Pressure*		*Temperature*	*Particle size*	*Bed division*
Ads	Des	Length	Diameter	PH	PL	T	Diameter	DV
[s]	[s]	[m]	[m]	[bar]	[bar]	[K]	[mm]	[-]
873	873	12.0	1.0	15	0.1	288	2	50
1062	1062	12.0	1.0	15	0.1	288	2	50
1162	1162	12.0	1.0	15	0.1	288	2	50
1290	1290	12.0	1.0	15	0.1	288	2	50
1660	1660	12.0	1.0	15	0.1	288	2	50

3.4.6 Desorption time variation

The CO_2 which is adsorbed in the adsorption steps is blown down during the desorption step. The length of this step is essential to get all that CO_2 desorbed from the bed. According to the adsorption equilibrium at P_L the desorbed amount cannot decrease further than the amount adsorbed at this pressure. Figure 25 illustrates the effect of adsorption time on performance indicators.

Since the CO_2 adsorption capacity increases with increasing desorption time (see Figure 26), this increases purity. The Higher CO_2 adsorption capacity of the bed also results in higher recovery of CO_2. The maximum value for purity and recovery is reached when no more desorption is possible after 4190

seconds of desorption. The figure also shows that the most increase in purity and recovery is in the adsorption time between 1000 and 1660 seconds, with purity increasing by 2.7%$_{mols}$ and recovery by 4.5%. With a further increase in the desorption time, the increase in purity and recovery is much lower. Namely, with a desorption time increase from 1660 seconds to 4190 seconds, the purity increased by only 2.6%$_{mols}$ and recovery by only 4.4%.

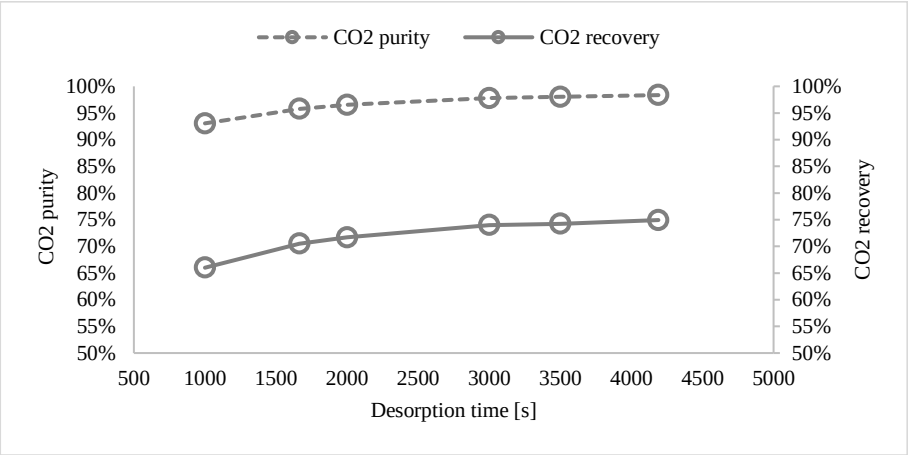

Figure 25 The CO_2 purity and recovery change with the changing desorption time.

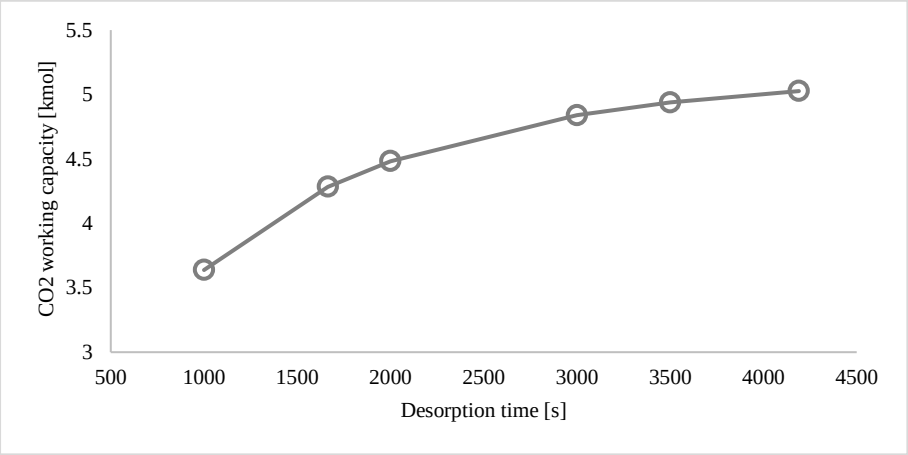

Figure 26 The CO_2 working capacity change with the changing desorption time.

Table 17 The values of the parameters used for the parametric study of the desorption time.

Time		*Bed size*		*Pressure*		*Temperature*	*Particle size*	*Bed division*
Ads	Des	Length	Diameter	PH	PL	T	Diameter	DV
[s]	[s]	[m]	[m]	[bar]	[bar]	[K]	[mm]	[-]
1660	1000	12.0	1.0	15	0.1	288	2	50
1660	1660	12.0	1.0	15	0.1	288	2	50
1660	2000	12.0	1.0	15	0.1	288	2	50
1600	3000	12.0	1.0	15	0.1	288	2	50
1600	3500	12.0	1.0	15	0.1	288	2	50
1660	4190	12.0	1.0	15	0.1	288	2	50

3.5 Optimised base case model

Using the studied parameters, the base case is optimised in the parametric study and the optimised values of the parameters are listed in Table 19. The other model parameters have remained the same as the base case. Some actual results and performance indicators are listed in Table 20. The flowsheet used for this optimised base case is presented in Figure 27.

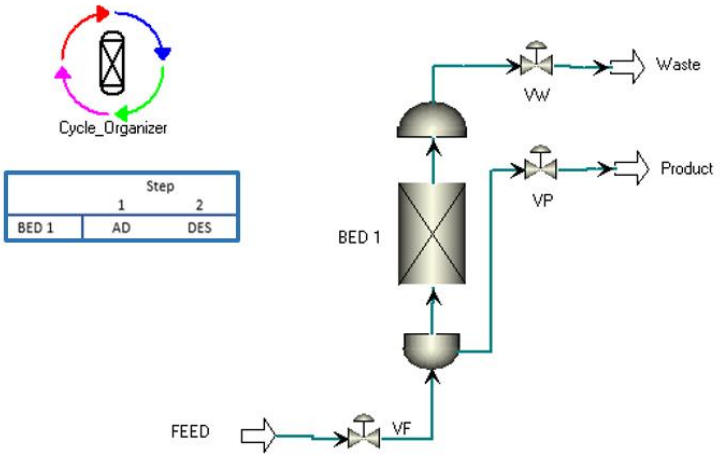

Figure 27 Flowsheet of the single bed adsorption-desorption PSA cycle.

Table 18 The composition and conditions of the feed, CO_2 rich and CO_2 lean stream as shown in the flowsheet of Figure 27.

		FEED	*PRODUCT*	*Waste*
T [K]		288.00	287.76	284.01
P [bar]		15.0	0.1	1.0
Flowrate [kmol/s]		0.0197	0.0050	0.0117
Molar composition	CO_2	0.2535	0.9427	0.0728
	CO	0.2954	0.0403	0.3607
	H_2	0.0525	0.0007	0.0688
	N_2	0.3687	0.0154	0.4753
	O_2	0.0066	0.0002	0.0086
	CH_4	0.0109	0.0007	0.0138

Table 19 The values of the optimised parameters for the PSA cycle of the base case in a single adsorption bed.

Bed size		*Pressure*		*Temperature*	*Particle size*	*Time*		*Bed division*
Length	Diameter	PH	PL	T	Diameter	Ads	Des	DV
[m]	[m]	[bar]	[bar]	[K]	[mm]	[s]	[s]	[-]
9.0	0.75	15	0.1	288	2	1290	1290	50

Table 20 Several performance indicators for the single bed adsorption cycle for the optimised base case.

Purity	*Recovery*	*Pressure drop*	*CO_2 working capacity*
[$\%_{mols}$]	[%]	[kPa]	[kmol]
94.27	84.30	10.23	3.98

The PSA system in its basic form consists of two beds alternately pressurised and depressurised. The optimised one-bed model is further expanded to a two-bed model always to have a constant feed flow to the PSA unit. Here, two beds with the same properties as the optimised base case model were placed next. As shown in the flowsheet in Figure 28. There is continuous flow to the PSA unit because the adsorption and desorption times are the same. As the first bed adsorbs into the other bed, they desorb and alternate, creating a continuous feed and stream. The composition and conditions of the feed stream (FEED), CO_2 rich stream (Product), and CO_2 Lean stream (Waste) are given in Table 21.

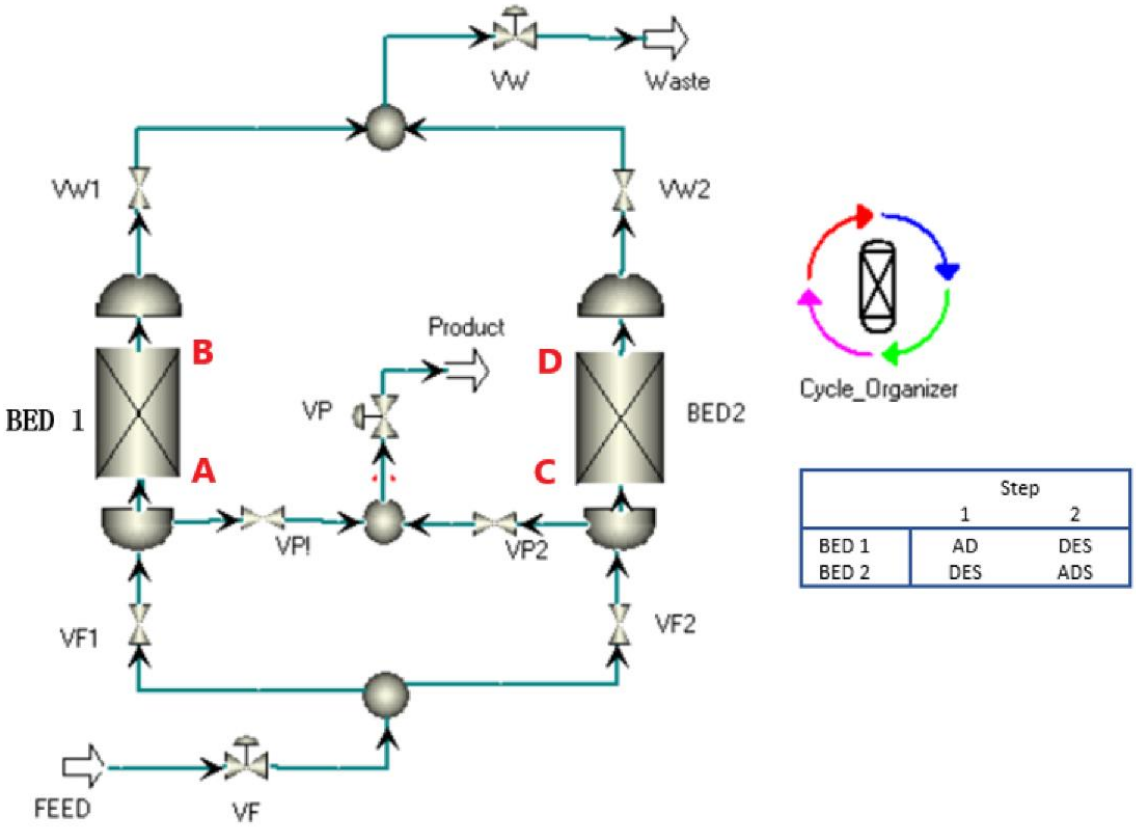

Figure 28 Flowsheet of the two beds' adsorption-desorption PSA cycle.

With this two-bed two steps cycle, a CO_2 purity of 94%$_{mols}$ can be reached, and 84% CO_2 can be recovered.

Table 21 The composition and conditions of the feed, CO_2 rich and CO_2 lean stream as shown in the flowsheet of Figure 28.

		FEED	*Product*	*Waste*
T [K]		288.00	287.76	284.01
P [bar]		15.0	0.1	1.0
Flowrate [kmol/s]		0,0172	0,0055	0,0117
Molar composition	CO_2	0.2535	0,9437	0,0656
	CO	0.2954	0,0383	0,3645
	H_2	0.0525	0,0010	0,0692
	N_2	0.3687	0,0161	0,4781
	O_2	0.0066	0,0002	0,0086
	CH_4	0.0109	0,0007	0,0139

4 RESULTS

4.1 Final optimized 2 bed model

The final optimised model consists of two beds. The parameter values used in the bed configuration are shown in Table 22. The PSA cycle consists of 2 steps, adsorption, and desorption of 1260 seconds.

Table 22 Parameters used to simulate the optimised base case in two beds two steps PSA cycle.

PARAMETER	VALUE
Column properties	
Length, L [m]	12
Internal bed diameter, d_{bi} [m]	1.0
Particle radius, r_p [m]	2.0 ×10-3
Bed voidage, ε_b [–]	0.33
Particle voidage, ε_p [–]	0.54
Adsorbent bulk density, ρ_p [kg m^{-3}]	756.00
Bed wall thickness	0.0024
Wall density [kg m−3]	7830.0
Thermo-physical properties	
Universal gas constant, R [m^3 Pa mol^{-1} K^{-1}]	8.314
Adsorbent specific heat capacity[MJ/kg/K]	0.0487
Wall specific heat capacity [J/kg/K]	502.8
Wall thermal conductivity [W/m/K]	16.0
Heat transfer coefficient (wall to ambient) [MW/m2/K]	1.0 ×10-9
Heat transfer coefficient (gas to solid) [MW/m2/K]	1
Heat transfer coefficient (gas to wall) [MW/m2/K]	1.0 ×10-6
Heat of adsorption CO_2, ΔH_CO_2 [kJ mol^{-1}]	-24.20
Heat of adsorption CO, ΔH_{CO} [kJ mol^{-1}]	-18.10
Heat of adsorption N_2, ΔHN_2 [kJ mol^{-1}]	-15.25
Heat of adsorption H_2, ΔHH_2 [kJ mol^{-1}]	-0.11
Heat of adsorption O_2, ΔHO_2 [kJ mol^{-1}]	-11.87
Heat of adsorption CH_4, ΔHCH_4 [kJ mol^{-1}]	-12.01
Mass transfer coefficient, CO_2, MTC_{CO2} [s^{-1}]	0.0137
Mass transfer coefficient, CO, MTC_{co} [s^{-1}]	0.0172
Mass transfer coefficient, N_2, MTC_{N2} [s^{-1}]	0.0172
Mass transfer coefficient, H_2, MTC_{H2} [s^{-1}]	0.0641
Mass transfer coefficient, O_2, MTC_{O2} [s^{-1}]	0.0228
Mass transfer coefficient, CH_4, MTC_{CH4} [s^{-1}]	0.0227
Operating conditions	
Feed gas pressure P_{feed} [bar]	1
High pressure P_H [bar]	15
Low pressure [bar]	0.1
Feed composition (CO_2/ CO/ N_2/ H_2/O_2/CH_4)	0.2535/ 0.2954/ 0.3687/ 0.0525/ 0.0066/ 0.0109
Feed temperature, T_{feed} [K]	288
Ambiant temperature [K]	298.15
Duration of steps	
Adsorption time [s]	1260
Desorption time [s]	1260

The inlet and outlet pressure profile of two working beds of one cycle when the steady state is reached is presented in Figure 29. The first section of bed 1 is marked as letter A and the last section of bed 1 is market as letter B in **Error! Reference source not found.**.

At zero seconds bed 1 starts to adsorb (at the same time bed 2 starts desorbing). The pressure in the A of bed 1 is 15 bar (see blue line in Figure 29). But there is a pressure drop along the length of bed 1 so the last part of bed 1 (position B) has a lower pressure than first part of bed 1 (see red line in Figure 29). The pressure drops with 10.54 kPa along the length of the bed and the length-specific pressure drop is equal to 0.88 kPa/m.

When the adsorption step is finished (at 1260 seconds), the desorption step for bed 1 where the pressure is reduced to 0.1 bar. The blue and red lines in Figure 29 fall sharply. The blue line descends faster than the red line because the pressure drop begins at position A of bed 1. The desorbed gases are discharged from position A of bed 1 to the CO_2 rich stream. The pressure profile of bed 2 is the same as that of bed 1.

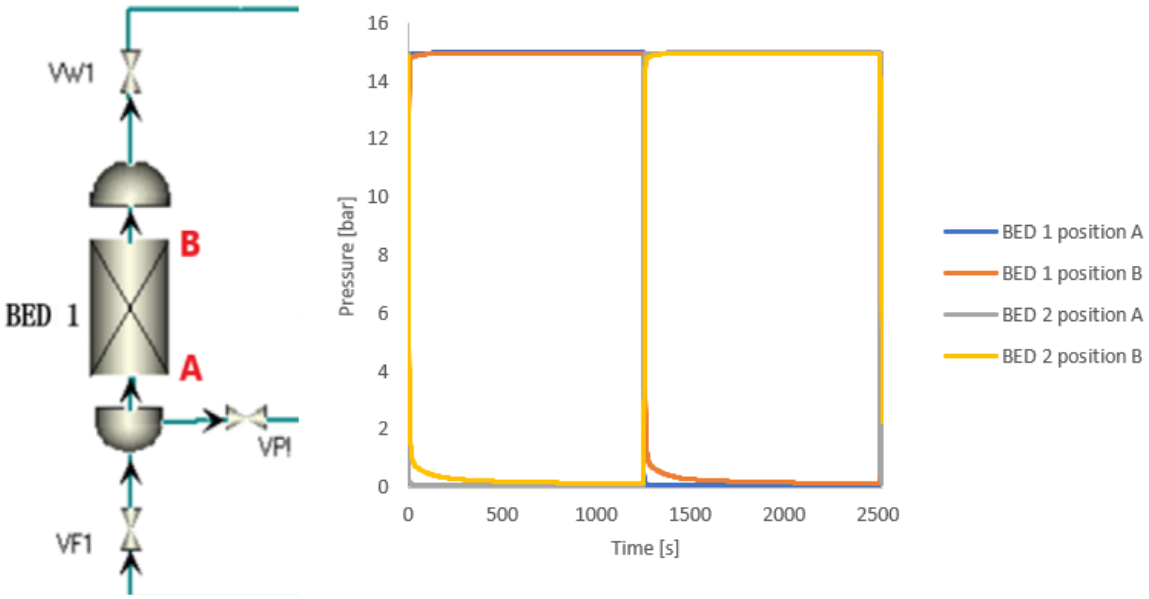

Figure 29: Pressure profiles at inlet (position A) and outlet (position B) of the adsorbing beds for one cycle at the steady state of the PSA.

The adsorption process is an exothermic process and the desorption process is an endothermic process. This results in temperature increase and decrease during the adsorption and desorption steps, respectively. Figure 30 illustrates the temperature profiles at the start and end of these adsorption and desorption steps in the PSA cycle. These temperatures are given for each position of the adsorbing bed starting with the inlet position A of the bed as shown in Figure 29

At the beginning of adsorption the bed is fed with the feed gas (at 288K), this is the temperature of the bed, at 0 m height of the bed where the feed gas enter the bed (see start of blue line in Figure 30. Since there are still some CO_2 adsorbed remained from the previous cycle because during the last desorption step there is still some CO_2 remained in the bed and not desorbed, the temperature of the rest of the bed in not at 288K but at 289.5 K. Initial sections of the bed (at 0 m to 0.75 m height) are a transition zone of temperature from 288K to 289.5 K.

At the end of the adsorption step, many gases are adsorbed in the bed, increasing the temperature of the bed to 290.5 K (red line in Figure 30). At that time, desorption in the bed starts. During the desorption step the temperatures in the bed drops to 289.5 K because of the endothermic desorption process. At the end of desorption, the bed has the same temperature in terms of temperature as the adsorbent had started with. The grey and blue lines in Figure 30 coincide.

As mentioned before, the rising temperature profile in the first part of the bed and the last part of the bed are a temperature transition zones between the temperature of the feed gas with the internal bed temperatures and the outlet gas with the internal bed.

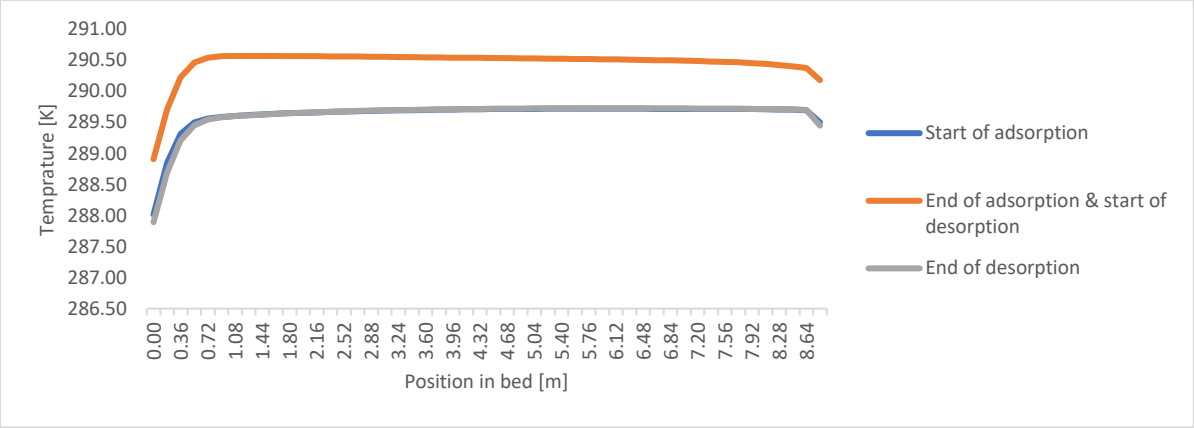

Figure 30: Temperature profiles at the start and end of the different PSA cycle steps at the PSA unit's steady state.

To get a much better view of what happens in each bed layer and timeslot during the adsorption and desorption, Figure 31, Figure 32 and Figure 33 are created.

Figure 31 shows the gas phase molar fractions for the entire length profile of the adsorbing bed of 9 m long. There are 4 different graphs, for the start of adsorption, end of adsorption, start of desorption and end of desorption steps while the PSA cycle has reached a steady state.

The adsorption step starts with feeding the bed with the feed gas composition; this is the molar gas phase composition shown at 0 m height of the bed, as shown in Figure 31a. The gas phase molar fraction is lower toward the end of the bed because in the first second of the adsorption step, some of the CO_2 is already adsorbed in the bed. This is also illustrated in Figure 33a, which shows the adsorbed amount of the gas components along the length of the bed. At the bed's last layer (9m height), the CO_2 molar fraction is decreased to 7 percent because some CO_2 is adsorbed.

During the adsorption step, CO_2 and other gas components are adsorbed in at all height of the bed and at the end of the adsorption steps, the bed has no capacity to adsorb more gases. Which means that all the gas that enter the bed and the gas that leave the bed will have the same composition. See the gas phase composition in all bed layers in Figure 33b. In the last layers of the bed (7m to 9m height) the CO_2 composition is a little narrower than the bed layers below, this is because the adsorptive step stopped slightly earlier than the full adsorption time, so there is still some adsorption of CO_2 takes place in these higher bed layers.

The graph of the gas phase composition at end of adsorption (Figure 31b) and start of desorption (Figure 31c) is the same. Because these represent the same time in the cycle.

During the desorption step, the adsorbed gas components in the bed are desorbed. The gas components with the smallest heat of adsorption are desorbed faster than the components with high heat of adsorption. CO_2 has the highest value for the heat of desorption compared to the other gas component that's why the other gas components are desorbed easier. Which means that at the end of the desorption step mainly CO_2 is desorbed, and CO_2 has a gas phase molar fraction of 100% at the end of the desorption step (see Figure 31d)

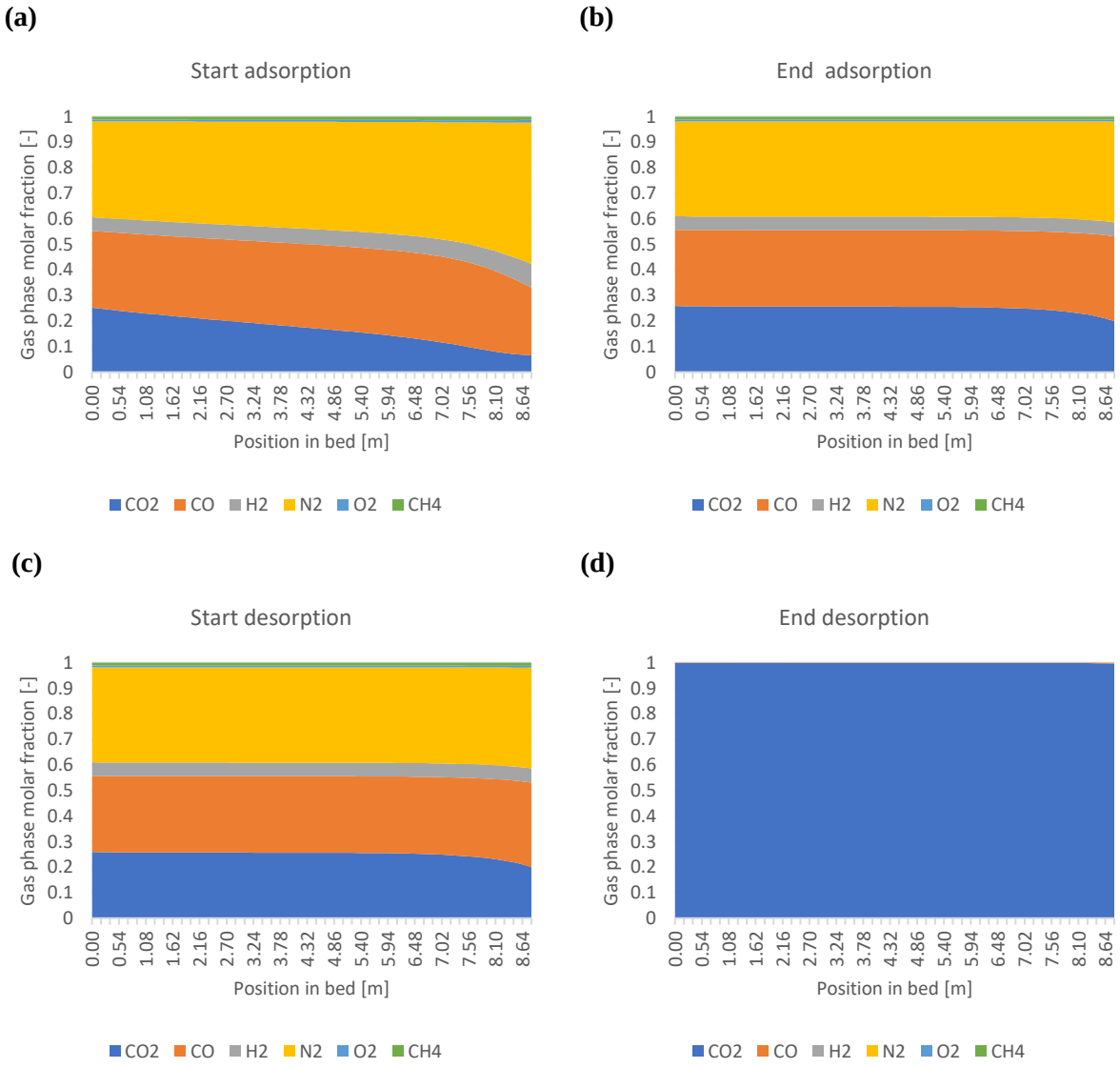

Figure 31 The gas phase molar fractions in the adsorbing beds at the start and end of the adsorption and desorption steps while the PSA cycle has reached a steady state.

Figure 32 illustrates the bed outlet molar fraction of the different gas components during the adsorption and the desorption steps of a PSA at the steady state.

During the adsorption step the bed outlet molar fraction of the different gas components changes as shown in Figure 32a. In the beginning of adsorption, the bed outlet molar fraction of CO_2 is 7%, as explained before for Figure 31a. During the adsorption step, the CO_2, together with the other gas components, is adsorbed, which means that the bed outlet CO_2 fraction is low during the adsorption step. Towards the end of the adsorption step, the CO_2 composition in the bed outlet will increase, because the bed becomes increasingly full of CO_2 and therefore has less capacity to adsorb even more CO_2 that enters the bin via the feed. Therefore, more CO_2 leaves the bed in the last phase of the adsorption step (see gray surface in Figure 32a).

During the desorption step, all desorbed gas components leave the bed through the bed outlet. The composition of this outlet gas changes during the desorption step, see Figure 32b. As already discussed, other gas components are more easily desorbed than CO_2, leaving the bed earlier in the desorption time. This can be seen in Figure 32b, from 0 s to about 800 seconds of the desorption step. After 800 seconds only desorption of CO_2 takes place in the bed and the outlet gas will also have a composition of almost 100% CO_2.

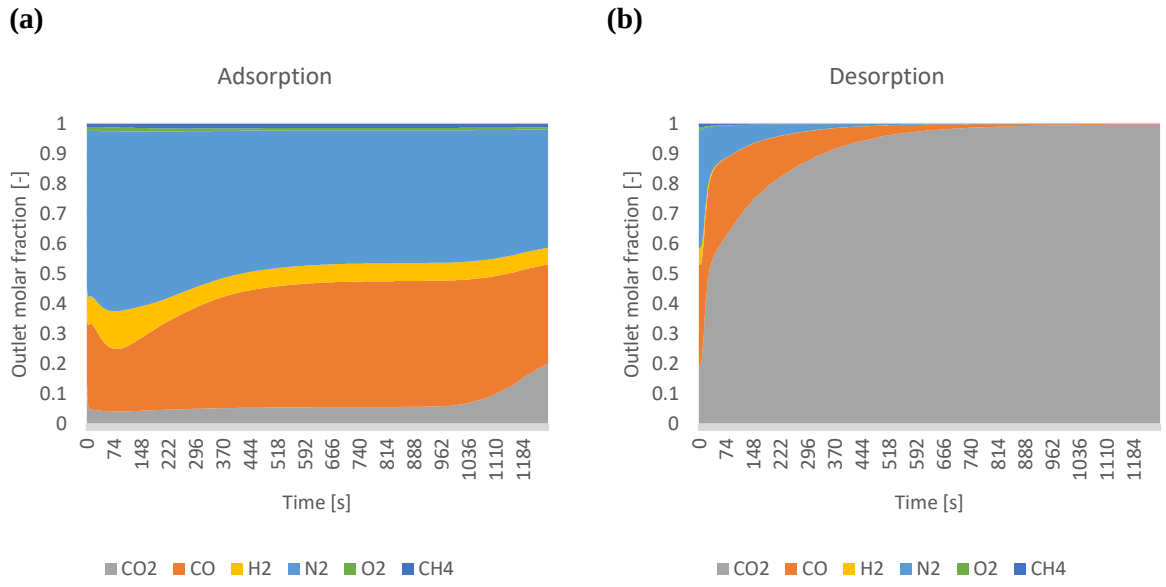

Figure 32 The bed outlet molar fraction of the different gas components during the adsorption and desorption steps.

Figure 33 shows the amount of adsorbed gasses during at the start and end of the adsorption and desorption steps during a PSA cycle in the steady state.

During the desorption, not all bed layers have the same CO_2 working capacity. The amount of CO_2 that can be adsorbed in each bed layer is the same, but not the same amount of CO_2 is desorbed in every layer. More desorption takes place in the lower bed layers (where desorption starts), because during desorption the gases are discharged via the bottom of the bed, so that there is always a constant pressure on the adsorbed gas particle in these layers. Ideally, all layers of the bed should function in the same way, but the longer the bed gets, the greater the difference in the amount of CO_2 that is desorbed in these layers.

For this reason, at the end of the desorption step, the amount of CO_2 remaining in the bed is not the same, as can be seen in Figure 33a. The adsorption step starts with this non-uniform distribution in the bed. During the adsorption step, the amount of adsorbed gases increases even more. The two other best-adsorbed gases after CO_2 are CO and N_2 (see Figure 33b). It was also these two gas components that desorbed and exited the bed more quickly as discussed in Figure 32b.

The uneven pattern in Figure 33b is because, as already mentioned, the adsorption step is stopped slightly earlier than the normal adsorption time, so that the top layers in the bed are not yet saturated with CO_2. The reason for this early stopping of the adsorption step is because more CO_2 is slips from the and is lost during the last few 100 seconds of the adsorption step (see Figure 32a). This results in a reduction of the CO_2 recovery of the PSA cycle. This was also discussed in the parameter study of the adsorption time.

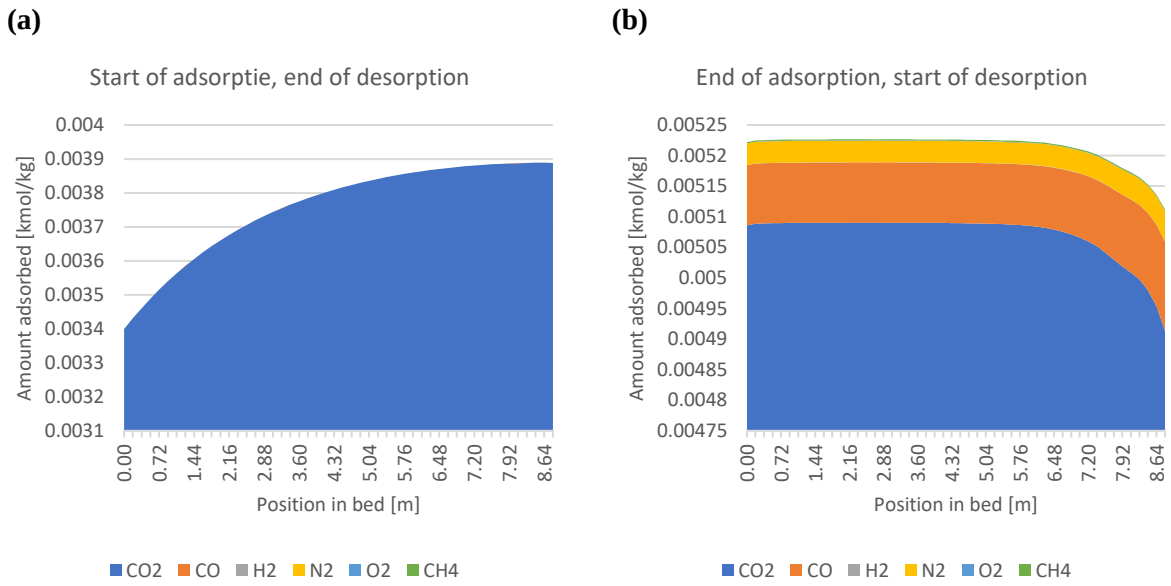

Figure 33 The amount of adsorbed gasses during the beginning and end of the adsorption and desorption steps.

CO_2 dominates the amount of adsorbed gas components in Figure 33b; there are also lesser amounts of CO and N_2. The working capacity of the various gas components can be calculated from this figure. The working capacity of CO_2 is shown in the bar graphs in Figure 34. This capacity is four times smaller for CO and about eight times smaller for N_2 gas. The capacity of other components is almost zero, meaning these gases are not adsorbed and flow through the flux. The red line in Figure 34 represents the selectivity of the bed for CO_2 compared to the other gas components. The bed is four times more selective for CO_2 than CO and eight times more selective than N_2 gas. The selectivity of CO_2 over CH_4 and H_2 is remarkably high; see the data table in Figure 34.

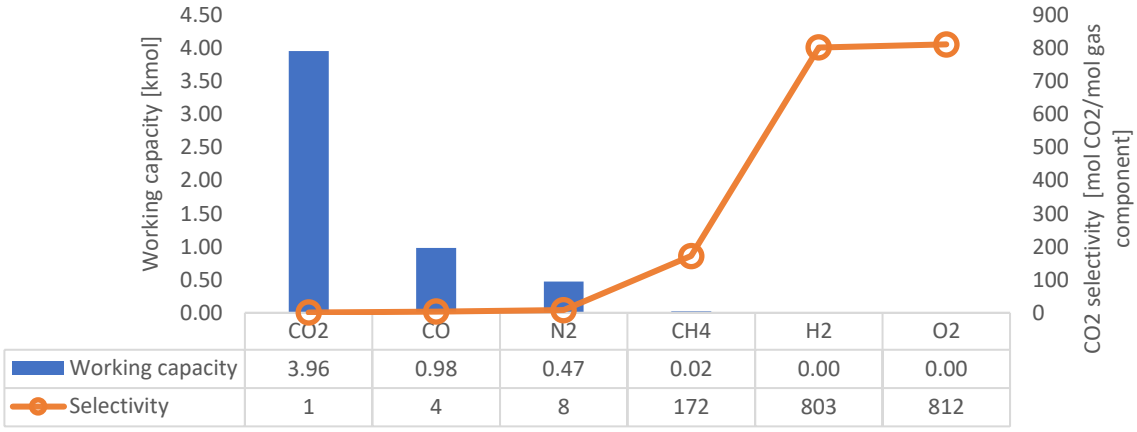

Figure 34 The CO_2 working capacity and the selectivity of CO_2 over the other gas components for the optimised two-bed two steps PSA cycle.

The value of the different performance indicators is listed in Table 23. The high selectivity of the adsorbing bed for CO_2 results in a CO_2 purity of 94%$_{mols}$ in the CO_2-rich stream. Since CO_2 slipped from the bed during adsorption, the CO_2 recovery is 84%. Besides the CO_2-rich stream, there is a CO_2 lean stream consisting of 48% N_2, 36% CO, 7% H_2, 7% CO_2 and 1% CH_4 and 1% O_2 (see Table 21).

Table 23 Several performance indicators for the optimised two-bed PSA cycle.

	Unit	*Value*
Purity	[%$_{mols}$]	94.37
Recovery	[%]	84.37
CO_2 processed	[Mt/y]	2.286
CO_2 captured	[Mt/y]	1.928
CO_2 working capacity	kmol	3.96
Pressure drop	[kPa/m]	0.88
Energy required[2]	[GW_e]	0.118
Net cooling duty[3]	[GW_t]	0.084
Specific energy required	[GJ_e/ tonne CO_2 captured]	1.866
Specific cooling duty required	[GJ_t/ tonne CO_2 captured]	1.328
Nr of trains needed	[-]	390

[2] The amount of energy is determined by modelling the compression and vacuum in ASPEN Plus®. See Appendix B- Compression during PSA for more details on these processes.

[3] The net cooling duty is the duty required for the cooling during the compression and vacuuming during the PSA. See Appendix B- Compression during PSA for more details on these processes.

5 DISCUSSION

5.1 Key findings of the research

This study started with a literature study into the most suitable adsorption material for CO_2 adsorption, which has a high capacity for CO_2 and has the necessary stability to function during a PSA. Among all materials studied, zeolites have large adsorption capacities at low pressures and moderate temperatures and offer significant CO_2 /N_2 selectivity due to their large specific surface area. It also has fast kinetics and can exhibit the cyclic stability required in a PSA process. The main drawback of this adsorbent is that it is sensitive to impurities and moisture in the feed stream, reducing their active surface area availability. This problem is avoided by assuming that waste in the feed gas is removed before entering the PSA column.

For zeolite 13X, by using the adsorption isotherms from the literature, the best fitting isothermal model has been selected, the Sips isothermal model. However, due to certain limitations (which will be discussed further) in the Aspen Adsorption™ software, this isothermal model did not turn out to be an isothermal model. In addition to the Sips isotherm model, the extended Langmuir 3 model was also used, which proved ineffective. Finally, a temperature-independent Langmuir 1 isotherm model was applied.

The complete PSA model has been further optimised in an extensive parameter study, which showed that the optimal pressure range for the PSA is between 15 and 0.1 bar. The optimised bed has a length of 9 m and a diameter of 0.75 m. If the model consists of a train of 2 adsorption beds, 390 trains are needed to process the complete BFG and BOFG mixture. The complete PSA system will require a specific energy demand of 1,866 GJ per tonne of CO_2 captured for its pressure reduction and increase. Ultimately, 1.9 megatons of CO_2 can be captured in this system, with a recovery rate of 84% with a CO_2 purity of $94\%_{mols}$.

5.2 Results validation

The mathematical model was validated with two different experimental breakthrough data. The results of the two steps optimised model in this study are compared in the table with several essential performance indicators from other CO_2 capture studies by the R&D department of Tata Steel Ijmuiden. [119]

The purity recovery and yearly amount of CO_2 captured from this study were compared with two other adsorption and absorption systems.

The only difference between the four systems and the system in this study is that there are minor differences in the feed gas composition, see Table 24. The other four studies process blast furnace top gas (so it does not contain BOFG) with 8500 operating hours a year. There is 2% less CO_2 in the feed gas, and the feed temperature is 328 K instead of 288 K. For this reason, the technologies cannot

be compared, but one can make a presumable comparison in Table 25. The purity of the model in this study is higher than 90%$_{mols}$, which is also the case for three of the compared technologies except for the VPSA with tail gas compression. The CO_2 recovery of the model is in the order of the recoveries achieved in absorption systems and is lower than the recovery achieved in the two adsorptive systems. The low recovery of this model is due to the incomplete desorption of the CO_2 during the desorption step.

Table 24 The composition and condition for the feed gas used in this study and the comparing study [119]

	This study	**Comparing study** [119]
	Mole fraction (dry basis)	Mole fraction (dry basis)
H_2	0.0525	0.05
N_2	0.3687	0.49
CO	0.2954	0.23
CH_4	0.0109	0.0
CO_2	0.2535	0.23
O_2	0.0066	0.0
Temperature (K)	288	328
Pressure (bara)	1	1.5
Mass Flows (kg/hr)	734604	899621
Mole Flows (kmol/hr)	24104	29602

Table 25 A Comparison table for the CO_2 purity, CO_2 recovery and the amount of CO_2 adsorbed using the optimised two beds model in this study and the comparing study [119]

	PSA (this study)	*Amines*	*Physical solvents*	*VPSA with tail gas compression*	*VPSA + cryogenics*
CO_2 Purity (dry basis)	94.37%$_{mols}$	99.8%$_{mols}$	97.0%$_{mols}$	73.6%$_{mols}$	96.1%$_{mols}$
CO_2 recovery	84.37%	89.0%	82.5%	92.2%	91.5%
Total CO_2 captured[4]	1.928Mt/y (220.1 t/h)	2.307 Mt/y (271.4 t/h)	2.138 Mt/y (251.5 t/h)	2.390 Mt/y (281.2 t/h)	2.373 Mt/y (279.2 t/h)

In addition, this study's results were compared with another study on the absorption of CO_2 using MEA [120]. The feed gas composition and conditions of this comparative technology are shown in the

[4] The amount of CO_2 capture is calculated based on the flow rate in

Table 26. Both in this study and in the reference study, it is assumed that the steel plant is running 8500 h/y, corresponding to 97% availability.

Table 26. The gas composition can be assumed to be the same, and the temperature and pressure are almost the same.

Table 26 The composition and condition for the feed gas used in this study and the comparing study [120]

	This study	**Comparing study** [120]
	Mole fraction	Mole fraction
H_2	0.0525	0.05459
N_2	0.3687	0.39293
CO	0.2954	0.27949
CH_4	0.0109	0.0003
CO_2	0.2535	0.25457
O_2	0.0066	0.00712
Temperature (K)	288	285
Pressure (bara)	1	1
Mass Flows (kg/hr)	734604	467394
Mole Flows (kmol/hr)	24104	15284

The comparison of the essential performance indicators of the model in this study and the absorption model are presented in the Table 27. The CO_2 is 2% lower than the purity achieved in chemical absorption, and the recovery is also 6% lower. The cause of the low recovery is the already multiplied incomplete desorption. The low purity is because adsorptive systems are less specific for a particular gas component than the very gas-specific absorption that leads to high purity.

Table 27 Comparison table of important PSA cycle performance indicators using the optimised two beds model of this study and the comparing study [120]

		Physical adsorption (this study)	*Chemical absorption (MEA)*
	Unit	Value	Value
Purity	[$\%_{mols}$]	94.37	96.5
Recovery	[%]	84.37	90.1
CO_2 processed	[Mt/y]	2.286	2.253
CO_2 captured	[Mt/y]	1.928	2.029
Energy required	[GWe]	0.118	0.003
Net cooling duty	[GWt]	0.084	0.205
Specific energy required	[GJ_e/ tonne CO_2 captured]	1.866	0.047
Specific cooling duty required	[GJ_t/ tonne CO_2 captured]	1.328	3.191

5.3 Limitations of the model

The Aspen Adsorption™ software has several limitations, which have had a particular effect on the model's overall performance.

A notable and significant limitation of the software is how it determines the operation of the desorption step based on the adsorption isotherm model. The Sips isotherm model was found to be the best fit from the fitting of the adsorption isotherms. This isotherm model is not in the isotherm model library of |Aspen Adsorption™ V12.0. Therefore, an external code was added to the isothermal model that described the behaviour of the sips isothermal model. This model described the adsorption step as

expected, but not enough desorption occurred in the desorption step (even when using a vacuum during desorption). Subsequently, another isothermal model was chosen that was present in the Aspen Adsorption™ library, namely the extended Langmuir 3 model. This model also proved to work perfectly for the adsorption but failed to model the desorption step.

Ultimately, a non-temperature-dependent Langmuir 1 model was chosen, which worked. Desorption took place, but the ideal and expected desorption (according to the equilibrium isotherm of the gas components) has still not been achieved. In the case of ideal desorption, the CO_2 recovery of the model would be higher.

Since this problem has appeared for two out of the three isotherm model used in this study. All possible adsorption models that may be applicable to this study should be considered. It is noteworthy that both temperature dependent adsorption isothermal models have not worked in this study. So to avoid this problem the isotherm model should be assumed to be temperature independent and other temperature independent adsorption isotherm models should be examined.

5.4 Further research recommendations

Above described limitation has taken a lot of time and research and would therefore have a particular effect on the recovery. However, even with this limitation, very good results for purity and recovery have been achieved by this model. Future work could seek whether there is a more robust method to describe the desorption in Aspen Adsorption™ .

There are some important future search recommendations to further expand this research:

5.4.1 Considering different feed gas

For even better results in terms of CO_2 capture, a different feed gas composition can be considered. There are three options for the sort of feed gas that can be used on the PSA for CO_2 capture.

The first possible is pre-combustion CO_2 capture, where CO_2 from steel gases is capture in their most raw form. This has been investigated in this study.

Post-combustion and oxyfuel combustion are also feasible options; for this, the feed gasses (BFG+BOFG) will first be combusted with air or pure oxygen. Since the CO_2 content of the raw BOF+BOFG is low (~25 mol%), the CO in this gas can be converted into CO_2 by performing a water gas shift reaction (WGS), as shown in Equation 5-1. The WGS reaction is a reversible chemical reaction between carbon monoxide and steam to form carbon dioxide and hydrogen [121]. As a result, the gas will be enriched with CO_2 and H_2. It will be decided during the project and the supervisors whether the carbon capture process will precede a WGS.

Equation 5-1 Water-gas shift reaction

$$CO + H_2O \leftrightarrow CO_2 + H_2 \qquad \Delta H_{298K} = -41.16\ \text{kJ/mol}$$

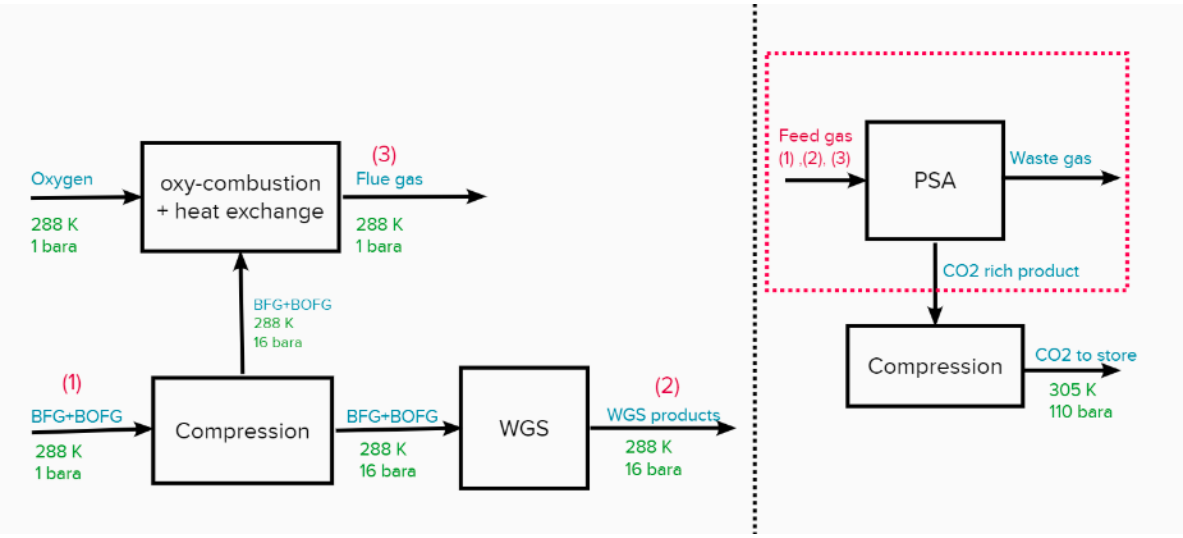

Figure 35: Flowsheet diagram of the possible feed gases starting from the raw BFG+BOFG and the processes that must precede it.

These three options for the feed gas are shown in a flowsheet diagram in Figure 35, together with the processes they must go through to arrive at these feed gas compositions and conditions (see Table 28).

Table 28 The gas composition and conditions of the feed gasses, as shown in Figure 35.

	(1)	(2)	(3)
	Mole fraction	Mole fraction	Mole fraction
H_2	0.0525	0.1566	0
N_2	0.3687	0.3309	0.3465
CO	0.2954	0.1557	0
CH_4	0.0109	0.0098	0
CO_2	0.2535	0.3369	0.5228
H_2O	0	0	0
O_2	0.0066	0.0059	0.0500
Temperature (K)	288	288	288
Pressure (bara)	1	16	1
Mass Flows (kg/hr)	734604	784195	906307
Mole Flows (kmol/hr)	24104	26859	25283

5.4.2 Considering different adsorbent material

Since the adsorption and desorption profile of the different gas components is very important for the performance of the PSA, other types of adsorbent material can be investigated. Which may yield better results. In addition, the soft aspen adsorption also has a very convenient option for the bed specification, namely, the bed can contain more than one kind of adsorption material. this makes it possible, for example, in various parts of the adsorption bed, to target a different gas component. Combining two or more types of adsorption material can also have a significant effect on the functioning of the PSA cycle.

5.4.3 Performing an economic analysis

The costs of the PSA unit are an essential aspect of a large-scale CO_2 capture system, which can best be considered by performing an economic analysis of the system. The economic part of a PSA is also an important parameter in determining the choice for a large-scale CO_2 capture system.

5.4.4 Extension of the study parameter

the parameter study for the optimization of the model was just a part of this study. It can be further expanded by, for example, running more simulations per parameter. The choice of a different pressure range will also significantly affect the further optimisation of the model.

5.4.5 Addition of more steps to the PSA cycle

The two-bed two steps cycle can be further expanded into a Skarstrom cycle. The basic Skarstrom consists of four steps, pressurisation, adsorption, counter-current blowdown, and counter-current purge. During the cycle, both adsorption beds undergo these four steps. This basic cycle is further optimised to reduce the energy consumption of the PSA cycle. For this, two pressure equalisation steps are added to the cycle. The six steps of the Skarstrom cycle are as follows.

At the start of step 1, the pressure in bed 1 is the lowest. In step 1, the pressure in bed one is increased to the highest pressure of the PSA cycle (pressurisation PR). Simultaneously, bed two is blown down to the lowest pressure in the opposite direction, where the adsorbed gas components are withdrawn.

In step 2, bed one is exposed to the high-pressure feed gas, and the adsorption takes place. The gas components that have more affinity for the adsorbent in the bed are adsorbed, and the rest of the gas leaves the bed as effluent via the CO_2 lean stream. Part of this effluent is used as a purge gas to purge bed 2 in the opposite direction. By doing this, the remained gas species in bed two are purged, and bed two is made entirely free of strong adsorbing gas components. At the end of step 2, bed one is still at the highest pressure and bed two is at its lowest pressure. Step 3 opens a connection valve between the two beds, and the pressure is equalised. By doing this, the pressure in bed two is increased using the pressure in bed 1. A drawback of this equalisation step is that because the pressure in bed one drops, desorption takes place in bed two, and the desorbed gases move from bed 1 to bed 2. This small part of the desorbed gases is not recovered in the blowdown step. After the pressure equalisation in steps 4,5 and 6, the same steps as steps 1,2 and 3 are repeated but with the beds interexchanged.

The different steps and their operation is also shown in Figure 36.

To find out whether significant energy savings can be achieved without losing much of the CO_2 purity, the two beds two steps PSA cycle has been extended to the six steps in the Skarstrom cycle, as shown in Figure 36. The only adjustment is that during the purging step, nitrogen gas is used. This is because, for example, a small amount of CO_2 is still present in the effluent gases after the adsorption in bed 1 (the amount depends on the recovery). If this effluent is used to purge bed 2, the purged CO_2 is replaced in bed two again by the small amount of CO_2 in this effluent gas. In other words, the bed is not purged. To avoid this effect, t, inert N_2 gas was used in the purging stream.

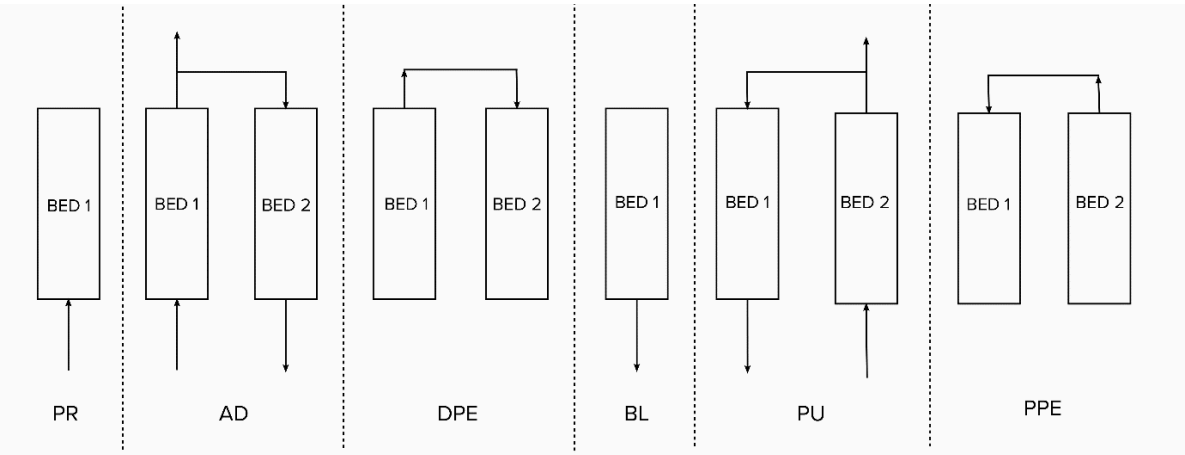

BED	STEP					
1	PR	AD	DPE	BL	PU	PPE
2	BL	PU	PPE	PR	AD	DPE

Figure 36 Schematic representation of the two adsorption beds during the six different steps of a six-step PSA cycle.

The flowsheet used for this two-bed six steps model is shown in Figure 37. The configuration of the beds is identical to the optimised two-bed two steps model. A connection is made between the two beds via a control valve, which is opened during the two pressure equalisation steps. In addition, the flowsheet also shows the separate supply of N_2 gas. This gas purges the bed in counter-current direction and eventually ends up in a second CO_2 lean stream (Waste 2). The composition and conditions of the feed stream (FEED), CO_2 rich stream (Product), CO_2 Lean stream (Waste1), N_2 as purging gas (N_2) and the second CO_2 lean stream, which is the result of the purging step (Waste 2) are given in Table 29.

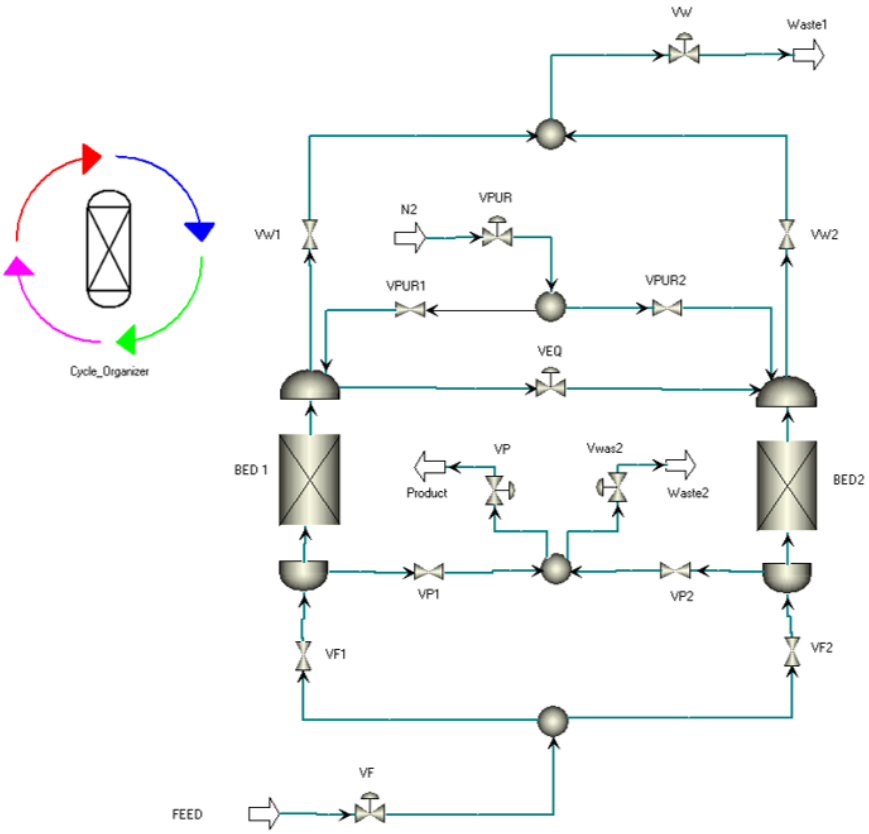

Figure 37 Flowsheet of the two beds six steps PSA cycle.

With this two-bed six steps cycle, CO_2 purity is increased to 97.5%$_{mols}$, but there is a significant decrease in the CO_2 recovery compared to the two-bed two steps cycle. The CO_2 recovery is decreased to 59.5%. For this model, other performance indicators such as energy demand, numbers of trains needed, or total feed gas to be processed and others were not considered.

Table 29 The composition and conditions of the feed, CO_2 rich and CO_2 lean streams as shown in the flowsheet of Figure 37.

		FEED	*N_2*	*Product*	*Waste 1*	*Waste 2*
T [K]		288	288	287	284	288
P [bar]		15.0	2.0	0.1	1.0	1.0
Flowrate [kmol/s]		0.0077[5]	0.0147	0.0025	0.0118	0.0124
Molar composition	CO_2	0.2535	0.0000	0.9750	0.0192	0.0988
	CO	0.2954	0.0000	0.0181	0.3743	0.0008
	H_2	0.0525	0.0000	0.0002	0.0691	0.0011
	N_2	0.3687	1.0000	0.0063	0.5147	0.8974
	O_2	0.0066	0.0000	0.0003	0.0086	0.0010
	CH_4	0.0109	0.0000	0.0001	0.0141	0.0009

[5] The feed gas flow rate is the average of the feed gas flow rate during the pressurisation and adsorption step because both steps have the same time frame of 1962 seconds.

Due to the purging step, the CO_2 working capacity in the bed is increased to 7.26%. This increase in the bed CO_2 working capacity has caused the high CO_2 purity. The cause for the dramatic drop in the recovery is the purging step. During the purging step, part of the CO_2 is purged and becomes essential in the second CO_2 lean stream. In addition, there is also a loss of CO_2 in the first CO_2 lean stream during the adsorption step. So, more CO_2 is lost than in the case of the two-bed two steps model where there was only CO_2 loss in the CO_2 leans stream.

The addition of the purging steps, therefore, has two effects in this PSA system; it increases the purity (+3.13 $\%_{mols}$), and on the other, it decreases the CO_2 recovery (-24.87%).

An advantage of this six steps model is that the addition of the purging steps increases the CO_2 purity. In addition, during the pressure equalisation step, the pressure of one bed is used to pressurise the other bed, and less electrical energy is needed for the compression and vacuum of the gases. In the six steps model described above, the pressure of both beds after the pressure equalisation step equals 3.4 bar. This means there are as many energy savings during the pressure increase step (compressing from 3.4 to 15 bar) as during the pressure reduction step (drawing vacuum from 3.4 to 0.1). Furthermore, this model needs further optimisation to increase the recovery of CO_2.

A final and essential drawback of this system is that the total cycle time is much considerable due to the additional steps in the cycle, so the constant feed flow rate that the PSA system will have with this six steps model will be lower than the two-step model. That means that more of the PSA unit as shown in Figure 37 is required for all the feed gas to be processed with the additional increase in construction, operating and maintenance costs.

The analysis for the 6 steps cycle needs further optimization. This could be a good starting point for a study that would follow this study. In the last section of the results chapter, we looked at further improvements to the model in a six steps PSA cycle. This model requires further optimisation.

6 CONCLUSION

In this study, a PSA adsorption model was built in aspen adsorption. For the physical adsorption of CO_2, in a literature study, Zeolites and activated carbon were found to be the best performing and most stable adsorbents considering the conditions of the crude BFG and BOFG mixture as the feed gas.

Zeolite 13X was chosen as an adsorbent for this study, where the adsorption isotherms are defined in Sips and Langmuir adsorption isotherm models. Using the Langmuir model as the isothermal model, the lumped resistance model as the kinetic model and the Ergun equation as the momentum model, a dynamic model has been built in Aspen Adsorption™ that assumes that for the material balance, there is no radial dispersion and for the energy balance it is assumed that no conduction takes place.

The dynamic adsorption model has been validated with experimental data from the literature in which the breakthrough curves of the different gas components in the gas mixture were simulated. The breakthrough curves were in good agreement with the experimental data.

The parameter study showed that the highest CO_2 purity and recovery is achieved at a pressure range of 15 to 0.1 bar. The number of discretisation volumes in the bed was found not to affect the performance of the adsorption bed. Particles of 2 mm in size, bed length and diameter of 9m and 0.75m, respectively, gave the best results regarding CO_2 adsorption and recovery.

The optimised model can handle 2.3 million tons of CO_2 annually with a feed flow rate of 6.7 kmol/s. The PSA unit can capture 84% of this feed gas with a purity of 94%$_{mols}$. This is about 2.0 million tons of captured CO_2 annually. For this performance and scale, 780 adsorption beds of the size mentioned above are needed. These are 390 trains of PSA units consisting of two parallel adsorption beds. The entire PSA system will have an energy demand of 0.12 GW_e and 0.08 GW_t of cooling duty only for its compression and vacuum. Expressed per unit of CO_2 capture, this is 1.9 GJ_e, and 1.3 GJ_t per tonne of CO_2 captured. These concluding numbers are listed in Table 30.

Table 30 List of the values of the essential performance indicators from the optimal two-bed two steps PSA cycle.

		Unit	*Value*
CO_2 purity		[%$_{mols}$]	94.37
CO_2 recovery		[%]	84.37
Operating pressure range			
	High pressure	[bar]	15
	Low pressure	[bar]	0.1
Column sizing			
	Length	[m]	9
	Diameter	[m]	0.75
Nr of trains required (2 columns per train)		[-]	390
Pressure drop		[kPa/m]	0.88
Energy required			
	Net work required	[GW_e]	0.118
	Net cooling duty	[GW_t]	0.084

7 APPENDICES

7.1 Appendix A –Experimental Adsorption Isotherm data

The experimental adsorption isotherm data of CO_2, CO, H_2, N_2 and CH_4 were taken from Park et al. [122] and were used to determine the adsorption equilibrium parameters. This data is presented in Table 31.

Table 31 Experimental data of CO_2 adsorption isotherm on zeolite 13X.

293 K		**308 K**		**323 K**	
P (kPa)	*q (mol kg^{-1})*	*P (kPa)*	*q (mol kg^{-1})*	*P (kPa)*	*q (mol kg^{-1})*
0.567	0.53	0.101	0.281	0.203	0.285
0.78	0.79	0.304	0.543	0.573	0.551
1.02	1.05	0.607	0.805	1.15	0.811
1.35	1.30	1.05	1.06	1.99	1.06
1.81	1.56	1.69	1.32	3.17	1.31
2.47	1.81	2.56	1.57	4.73	1.55
3.34	2.06	3.70	1.82	6.72	1.78
4.40	2.30	5.15	2.05	9.18	2.00
5.70	2.54	6.94	2.28	12.17	2.22
7.33	2.77	9.18	2.51	15.70	2.42
9.37	3.00	11.95	2.72	19.87	2.62
11.95	3.22	15.24	2.93	24.61	2.79
15.12	3.42	19.23	3.12	29.93	2.96
19.11	3.61	23.97	3.29	35.91	3.11
23.90	3.78	29.42	3.46	42.66	3.25
29.47	3.93	35.54	3.60	49.88	3.38
35.99	4.06	42.40	3.73	57.56	3.49
43.23	4.18	50.11	3.85	65.86	3.59
51.12	4.29	58.24	3.95	74.42	3.68
59.71	4.38	66.87	4.04	83.44	3.77
68.49	4.46	75.97	4.13	91.45	3.84
77.79	4.53	85.29	4.20	99.92	3.90
87.33	4.59	93.75	4.26	108.2	3.95
96.57	4.64	102.8	4.31	135.6	4.10
105.4	4.69	131.9	4.45	163.1	4.21
133.0	4.80	161.5	4.56	192.0	4.31
165.2	4.91	191.5	4.65	223.8	4.40
196.7	4.99	221.3	4.72	254.1	4.47
196.7	4.99	252.2	4.79	285.3	4.54
227.3	5.05	283.3	4.85	316.7	4.60
258.4	5.11	315.0	4.90	348.9	4.65
289.9	5.16	347.0	4.94	381.1	4.70
321.8	5.20	379.6	4.98	413.7	4.74
353.8	5.24	412.2	5.03	446.6	4.78
386.3	5.28	445.0	5.06	479.6	4.81
418.7	5.31	477.9	5.09	512.7	4.84
451.6	5.34	510.9	5.13	546.0	4.87
484.2	5.36	544.0	5.15	579.2	4.90
517.0	5.39	577.4	5.18	612.8	4.93
550.0	5.41	610.8	5.21	646.4	4.95
583.2	5.43	644.1	5.23	680.2	4.98

616.3	5.46	678.0	5.25	714.2	5.00
649.8	5.47	711.8	5.27	748.0	5.02
683.0	5.50	745.6	5.29	781.7	5.04
716.5	5.51	779.3	5.31	815.7	5.06
749.9	5.53	813.4	5.33	849.8	5.07
783.5	5.54	847.1	5.34	884.0	5.09
817.1	5.55	880.6	5.36	917.8	5.11
850.5	5.56	914.5	5.38	952.0	5.12
884.3	5.57	948.5	5.39	986.3	5.13
918.1	5.58	981.9	5.41	1021.00	5.15
951.9	5.59	1016.00	5.42		
985.4	5.60				
1019.00	5.61				

Table 32 Experimental data of CO adsorption isotherm on zeolite 13X.

293 K		**308 K**		**323 K**	
P (kPa)	*q (mol kg^{-1})*	*P (kPa)*	*q (mol kg^{-1})*	*P (kPa)*	*q (mol kg^{-1})*
0.414	0.007	0.665	0.007	0.592	0.004
4.134	0.069	5.405	0.056	5.874	0.039
8.035	0.130	10.27	0.103	11.28	0.073
12	0.187	15.11	0.147	16.66	0.106
16.06	0.241	20.04	0.190	21.95	0.137
20.16	0.292	25.11	0.232	27.45	0.169
24.44	0.343	30.09	0.271	33.09	0.200
28.72	0.390	35.17	0.310	38.48	0.228
33.12	0.436	40.25	0.346	43.86	0.256
37.58	0.48	45.29	0.381	49.26	0.284
41.88	0.521	49.95	0.412	54.54	0.309
46.33	0.560	54.88	0.444	59.84	0.334
50.92	0.600	60.01	0.476	65.22	0.359
59.83	0.671	70.06	0.535	75.68	0.406
64.33	0.705	75.1	0.563	80.78	0.428
68.81	0.738	79.96	0.590	85.71	0.449
73.34	0.77	84.97	0.616	90.7	0.469
77.78	0.8	89.9	0.642	94.93	0.485
82.28	0.83	94.75	0.667	99.27	0.505
86.75	0.858	98.8	0.687	103.7	0.521
91.39	0.887	102.9	0.707	132.2	0.624
95.48	0.908	130.3	0.829	161.3	0.721
99.61	0.933	158.3	0.939	190.8	0.811
103.5	0.956	187.0	1.04	220.8	0.892
129.7	1.09	216.2	1.13	251.0	0.969
156.7	1.22	245.8	1.22	281.7	1.04
184.4	1.33	275.9	1.30	312.7	1.11
213.0	1.43	306.5	1.37	344.1	1.17
241.9	1.52	337.3	1.44	375.5	1.23
271.4	1.61	368.4	1.51	407.1	1.29
301.2	1.69	399.4	1.57	439.1	1.34
331.4	1.76	430.7	1.63	471.2	1.40
361.7	1.83	462.1	1.68	503.3	1.44
392.6	1.89	493.8	1.74	535.4	1.49
423.6	1.95	525.4	1.78	567.9	1.54
454.8	2.01	557.2	1.83	600.2	1.58
486.2	2.06	589.2	1.87	633.2	1.62
517.8	2.11	621.3	1.91	699.3	1.69
549.5	2.16	686.3	1.99	732.3	1.72
613.8	2.25	719.2	2.03	765.1	1.76

646.1	2.29	752.1	2.07	798.3	1.79
678.2	2.33	784.9	2.10	831.2	1.83
710.4	2.37	817.5	2.13	864.3	1.86
742.9	2.40	850.4	2.16	897.5	1.89
775.2	2.43	883.2	2.20	930.5	1.92
807.9	2.47	915.9	2.22	963.7	1.94
840.3	2.50	948.9	2.25	996.9	1.97
873.3	2.53	981.8	2.28		
906	2.56	1015	2.30		
938.7	2.59				
971.4	2.61				
1004	2.64				

Table 33 Experimental adsorption isotherm data for H_2 on zeolites 13X

293 K		**308 K**		**323 K**	
P (kPa)	*q (mol kg^{-1})*	*P (kPa)*	*q (mol kg^{-1})*	*P (kPa)*	*q (mol kg^{-1})*
0.693	0.000	0.67	0.000	0.78	0.000
7.67	0.002	7.71	0.001	8.00	0.001
14.43	0.003	14.67	0.003	15.10	0.002
20.96	0.004	21.68	0.004	22.11	0.003
27.49	0.006	28.26	0.005	28.82	0.004
33.80	0.007	34.90	0.006	35.44	0.006
40.07	0.009	40.89	0.007	41.78	0.007
46.01	0.010	46.81	0.008	48.10	0.008
52.15	0.011	52.73	0.010	54.36	0.009
57.92	0.012	58.37	0.011	60.37	0.010
63.61	0.014	63.96	0.012	65.64	0.010
68.64	0.015	68.87	0.013	70.85	0.011
74.27	0.016	74.19	0.014	76.03	0.012
78.97	0.017	78.95	0.015	80.69	0.013
83.58	0.018	96.55	0.017	97.33	0.016
88.06	0.019	100.1	0.019	100.6	0.016
92.62	0.020	134.4	0.025	135.1	0.021
96.65	0.020	168.6	0.031	169.7	0.027
99.29	0.021	202.7	0.038	204.4	0.032
102.2	0.022	237.3	0.044	239.1	0.037
136.1	0.029	271.5	0.050	273.5	0.043
170.1	0.037	306.1	0.056	308.2	0.049
204.3	0.044	340.4	0.062	343.1	0.055
238.0	0.052	374.5	0.069	378.0	0.060
272.1	0.059	409.0	0.075	412.5	0.066
306.2	0.066	443.8	0.082	447.5	0.072
340.2	0.074	478.4	0.088	482.3	0.077
374.2	0.082	512.9	0.095	516.8	0.083
408.1	0.089	547.5	0.100	551.5	0.089
442.1	0.095	582.0	0.106	586.3	0.094
476.1	0.102	616.5	0.112	621.1	0.099
510.2	0.109	650.8	0.119	655.7	0.104
544.1	0.116	685.3	0.125	690.3	0.110
578.3	0.124	719.6	0.130	725.2	0.115
612.3	0.132	857.6	0.154	864.6	0.137
646.3	0.139	892.2	0.160	899.4	0.141
680.3	0.145	926.5	0.166	934.1	0.148
714.3	0.152	961.0	0.173	968.8	0.152
748.2	0.160	995.1	0.179	1003.0	0.158
782.5	0.167				

816.5	0.174
850.5	0.181
884.5	0.187
918.5	0.194
952.3	0.201
986.2	0.209
1020.0	0.220

Table 34 Experimental adsorption isotherm data for N_2 on zeolites 13X

293 K		**308 K**		**323 K**	
P (kPa)	*q (mol kg^{-1})*	*P (kPa)*	*q (mol kg^{-1})*	*P (kPa)*	*q (mol kg^{-1})*
0.97	0.004	0.69	0.002	0.89	0.002
7.25	0.028	6.95	0.019	7.70	0.015
13.60	0.053	13.06	0.036	14.45	0.028
19.74	0.076	19.25	0.052	21.18	0.041
26.00	0.099	25.30	0.068	27.92	0.054
32.14	0.121	31.26	0.084	34.49	0.067
38.19	0.143	37.19	0.099	40.86	0.079
44.14	0.164	42.91	0.114	47.16	0.091
49.94	0.184	48.61	0.128	53.37	0.102
55.83	0.204	54.33	0.142	59.52	0.114
61.87	0.224	60.12	0.156	65.46	0.124
67.63	0.243	65.62	0.170	71.46	0.135
73.22	0.261	71.27	0.183	77.37	0.146
78.86	0.279	76.63	0.196	83.43	0.156
84.56	0.296	82.11	0.209	89.20	0.166
89.98	0.313	87.51	0.222	95.11	0.176
95.36	0.330	92.83	0.234	99.94	0.187
99.83	0.349	97.31	0.244	104.80	0.196
104.4	0.362	102.1	0.253	136.7	0.250
133.8	0.445	132.9	0.321	168.6	0.300
163.6	0.527	164.0	0.386	200.8	0.351
193.6	0.602	194.8	0.448	232.8	0.398
223.8	0.672	226.1	0.505	265.0	0.444
254.2	0.740	257.7	0.562	297.7	0.490
285.0	0.804	289.2	0.615	330.3	0.535
316.0	0.868	320.8	0.667	362.9	0.576
347.0	0.928	352.6	0.718	395.6	0.616
378.2	0.983	384.6	0.766	428.4	0.655
409.4	1.040	416.8	0.813	461.1	0.694
441.1	1.090	449.1	0.859	494.2	0.730
472.9	1.140	481.5	0.904	527.2	0.766
504.7	1.190	513.9	0.947	560.2	0.802
536.5	1.230	546.3	0.988	593.1	0.834
568.6	1.280	578.9	1.030	626.4	0.867
600.5	1.320	611.5	1.060	659.7	0.899
632.8	1.360	644.3	1.100	692.6	0.931
665.2	1.400	676.9	1.130	725.8	0.961
697.5	1.440	709.8	1.170	759.3	0.990
730.1	1.470	742.6	1.200	792.5	1.020
762.7	1.510	775.5	1.230	825.8	1.050
795.2	1.540	808.1	1.270	859.4	1.070
827.6	1.580	841.3	1.290	892.9	1.100
860.4	1.610	874.4	1.320	926.4	1.130
893.1	1.640	907.3	1.350	959.8	1.150
925.8	1.670	940.3	1.380	993.2	1.180
958.7	1.700	973.4	1.400		

991.4	1.730	1007.0	1.430		
1024.0	1.750				

Table 35 Experimental data of CH_4 adsorption isotherm on pelletized zeolite 13X.

293 K		**308 K**		**323 K**	
P (kPa)	*q (mol kg^{-1})*	*P (kPa)*	*q (mol kg^{-1})*	*P (kPa)*	*q (mol kg^{-1})*
0.592	0.004	0.553	0.003	0.829	0.003
5,840	0.039	6.164	0.03	6.974	0.024
11.25	0.074	11.72	0.056	13.27	0.045
16.46	0.108	17.31	0.083	19.38	0.066
21.51	0.14	22.82	0.108	25.4	0.086
26.73	0.172	28.39	0.134	31.34	0.106
31.65	0.203	33.72	0.158	37.43	0.126
36.64	0.233	39.05	0.182	43.1	0.145
41.34	0.261	44.22	0.205	48.8	0.163
46.37	0.291	49.57	0.228	54.47	0.181
51.34	0.32	54.92	0.252	59.91	0.198
56.08	0.348	60.09	0.274	65.29	0.215
60.7	0.374	65.04	0.295	70.84	0.233
65.37	0.4	69.8	0.314	75.98	0.249
70.1	0.427	74.74	0.335	81.02	0.264
74.41	0.45	79.59	0.355	85.93	0.279
79	0.475	84.21	0.373	90.79	0.294
83.34	0.499	88.75	0.392	94.74	0.307
87.66	0.522	93.6	0.411	98.48	0.319
91.98	0.545	97.73	0.427	102.4	0.332
95.46	0.562	101.6	0.442	135.3	0.427
98.75	0.58	133	0.56	167.7	0.515
102.2	0.599	163.9	0.669	199.5	0.597
132.3	0.745	194.4	0.77	230.6	0.676
162.1	0.881	224.6	0.864	261.1	0.748
191.6	1.007	254.1	0.951	291	0.815
221	1.122	283.4	1.033	321.8	0.883
249.9	1.231	313.3	1.112	352.8	0.948
278.6	1.328	343.9	1.189	383.7	1.012
307	1.419	374.2	1.261	415.1	1.07
334.9	1.504	404.6	1.33	447.1	1.126
364.4	1.588	435.6	1.397	478.7	1.179
394.6	1.668	466.8	1.461	510.4	1.235
424.9	1.744	497.9	1.522	542.5	1.285
455.7	1.819	529.4	1.58	574.6	1.335
486.5	1.888	560.9	1.637	607.1	1.381
517.5	1.953	592.9	1.691	639.8	1.426
549	2.015	624.5	1.743	672.2	1.473
580.5	2.077	656.4	1.793	704.9	1.512
612.2	2.135	688.8	1.841	737.4	1.551
644	2.19	721.3	1.887	770.3	1.589
675.9	2.243	753.8	1.932	803.2	1.625
708.2	2.292	786.6	1.975	836.3	1.661
740.5	2.344	819.6	2.017	869.4	1.695
772.8	2.399	852.4	2.057	902.5	1.727
805.8	2.441	885.4	2.096	935.7	1.761
838.7	2.484	918.5	2.133	969.2	1.789
871.6	2.527	951.7	2.169	1002	1.819
904.5	2.568	984.5	2.203		
937.7	2.608	1018	2.237		

970.8	2.647		
1004	2.695		

7.2 Appendix B- Compression during PSA

The net work and the net cooling duty of a compression and a vacuum process are modelled in aspen plus. For the compression, a two stage compression is applied using two isentropic compressors each followed by a cooler to reduce the temperature increase which ha happened during the compression. Vacuuming has been assumed to be the same as compression where a vacuum pressure gas (for example 0.1 bar) is pressurized tot for example 15 bar. The is modelled using a four stage compression unit, with three intercoolers. Also for this the same compressors and coolers are used.

- Compressor

A compression is called isentropic if the entropy does not change, as is the case with any reversible adiabatic compression. In such a compression, for an ideal gas the so-called isentropic relationship between the temperature T, pressure p and density.

For the isoentropic compression in aspen plus, the head developed may be obtained by applying $PV^k = constant$ to the head integral, assuming $k = C_p/C_v$ to be constant along the path:

$$HEAD = \frac{p_1 V_1}{\left(\frac{k-1}{k}\right)}\left[\left(\frac{p_2}{p_1}\right)^{k-1/k} - 1\right]$$

The enthalpy change and the head are related by:

$$\Delta h = \frac{HEAD}{h}$$

Where h is the isentropic efficiency, which's value is provided to the compression properties.

- Cooler

The cooling after a compression is modelled using a heater, where the net cooling duty is calculated by:

$$Net\ cooling\ duty = \frac{F_m}{M_W}(H_{out} - H_{in})$$

Where F_m is the mass flow to the heat exchanger, M_W is the molecular mass of the gas entering the heat exchanger, H_{in} and H_{out} are the inlet and outlet molar enthalpies of the entering and exiting gasses.

8 REFRENCES

[1] Anonymous "'Steel and emissions: How can we break the link?", March 25,.

[2] J. Li, Y. Ma, M.C. McCarthy, J. Sculley, J. Yu, H. Jeong, P.B. Balbuena and H. Zhou, "'Carbon dioxide capture-related gas adsorption and separation in metal-organic frameworks," *Coord.Chem.Rev.*, vol. 255, no. 15, pp. 1791-1823.

[3] M.A. Quader, S. Ahmed, R.A.R. Ghazilla, S. Ahmed and M. Dahari, "'A comprehensive review on energy efficient CO_2 breakthrough technologies for sustainable green iron and steel manufacturing," *Renewable and Sustainable Energy Reviews*, vol. 50, pp. 594-614.

[4] E. Blomen, C. Hendriks and F. Neele, "'Capture technologies: Improvements and promising developments," *Energy Procedia*, vol. 1, no. 1, pp. 1505-1512.

[5] X. Wu, Y. Yu, Z. Qin and Z. Zhang, "'The Advances of Post-combustion CO_2 Capture with Chemical Solvents: Review and Guidelines," *Energy Procedia*, vol. 63, pp. 1339-1346.

[6] A. Raksajati, M.T. Ho and D.E. Wiley, "'Reducing the Cost of CO_2 Capture from Flue Gases Using Aqueous Chemical Absorption," *Industrial & engineering chemistry research*, vol. 52, no. 47, Nov 27, pp. 16887-16901.

[7] Z.H. Ban, L.K. Keong and A. Mohd Shariff, "'Physical Absorption of CO_2 Capture: A Review," *Advanced materials research*, vol. 917, Jun 20, pp. 134-143.

[8] H. Zhai and E.S. Rubin, "'Systems Analysis of Physical Absorption of CO_2 in Ionic Liquids for Pre-Combustion Carbon Capture," *Environmental science & technology*, vol. 52, no. 8, Apr 17, pp. 4996-5004.

[9] R. Ben-Mansour, M.A. Habib, O.E. Bamidele, M. Basha, N.A.A. Qasem, A. Peedikakkal, T. Laoui and M. Ali, "'Carbon capture by physical adsorption: Materials, experimental investigations and numerical modeling and simulations – A review," *Applied energy*, vol. 161, Jan 1, pp. 225-255.

[10] A. Cormos, S. Dragan, L. Petrescu, V. Sandu and C. Cormos, "'Techno-Economic and Environmental Evaluations of Decarbonized Fossil-Intensive Industrial Processes by Reactive Absorption & Adsorption CO_2 Capture Systems," *Energies (Basel)*, vol. 13, no. 5, Mar 9, pp. 1268.

[11] C. Castel, R. Bounaceur and E. Favre, "'Membrane Processes for Direct Carbon Dioxide Capture From Air: Possibilities and Limitations," *Frontiers in Chemical Engineering*, vol. 3, Apr 29,.

[12] Keshavarz A., Ebrahimzadeh Sarvestani M., Rahimpour M.R., "'Cryogenic CO_2 Capture,", 02 January, pp. 251-277.

[13] C. Song, Q. Liu, S. Deng, H. Li and Y. Kitamura, "'Cryogenic-based CO_2 capture technologies: State-of-the-art developments and current challenges," *Renewable and Sustainable Energy Reviews*, vol. 101, pp. 265-278.

[14] M.A. Vale, A. Ferreira, J.C.M. Pires and A.L. Gonçalves, "'Chapter 17 - CO_2 capture using microalgae,", pp. 381-405.

[15] Singh Jyoti, Dhar Dolly Wattal, "'Overview of Carbon Capture Technology: Microalgal Biorefinery Concept and State-of-the-Art ," *Frontiers in Marine Science*, vol. 6.

[16] R. Sayre, "'Microalgae: The Potential for Carbon Capture," *Bioscience*, vol. 60, no. 9, Oct, pp. 722-727.

[17] M. Zaman and J.H. Lee, "'Carbon capture from stationary power generation sources: A review of the current status of the technologies," *Korean J. Chem. Eng*, vol. 30, no. 8, Jul 28, pp. 1497-1526.

[18] A.I. Osman, M. Hefny, Abdel Maksoud, M. I. A, A.M. Elgarahy and D.W. Rooney, "'Recent advances in carbon capture storage and utilisation technologies: a review," *Environ Chem Lett*, vol. 19, no. 2, Nov 22, pp. 797-849.

[19] R.T. Yang, "'Adsorbents,", 2003.

[20] D.H. Everett, "'Manual of Symbols and Terminology for Physicochemical Quantities and Units, Appendix II: Definitions, Terminology and Symbols in Colloid and Surface Chemistry," *Pure and applied chemistry*, vol. 31, no. 4, Jan 1, pp. 577-638.

[21] M. Sai Bhargava Reddy, D. Ponnamma, K.K. Sadasivuni, B. Kumar and A.M. Abdullah, "'Carbon dioxide adsorption based on porous materials," *RSC advances*, vol. 11, no. 21, Mar 31, pp. 12658-12681.

[22] R.T. Yang, "'Adsorbents,", 2003.

[23] M. Sultana, M.H. Rownok, M. Sabrin, M.H. Rahaman and S.M.N. Alam, "'A review on experimental chemically modified activated carbon to enhance dye and heavy metals adsorption," *Cleaner Engineering and Technology*, vol. 6, Feb, pp. 100382.

[24] L. MENG and S. PARK, "'Effect of heat treatment on CO_2 adsorption of KOH-activated graphite nanofibers," *Journal of colloid and interface science*, vol. 352, no. 2, pp. 498-503.

[25] S. Park, Y. Jang, J. Shim and S. Ryu, "'Studies on pore structures and surface functional groups of pitch-based activated carbon fibers," *Journal of colloid and interface science*, vol. 260, no. 2, pp. 259-264.

[26] S. Park, J. Shin, J. Shim and S. Ryu, "'Effect of acidic treatment on metal adsorptions of pitch-based activated carbon fibers," *Journal of colloid and interface science*, vol. 275, no. 1, pp. 342-344.

[27] C. PEVIDA, M.G. PLAZA, B. ARIAS, J. FERMOSO, F. RUBIERA and J.J. PIS, "'Surface modification of activated carbons for CO_2 capture," *Applied surface science*, vol. 254, no. 22, pp. 7165-7172.

[28] A. Arenillas, T.C. Drage, K. Smith and C.E. Snape, "'CO_2 removal potential of carbons prepared by co-pyrolysis of sugar and nitrogen containing compounds," *Journal of analytical and applied pyrolysis*, vol. 74, no. 1-2, Aug, pp. 298-306.

[29] K. Kim and S. Park, "'Synthesis of nitrogen doped microporous carbons prepared by activation-free method and their high electrochemical performance," *Electrochimica acta*, vol. 56, no. 27, Nov 30, pp. 10130-10136.

[30] M. Seo and S. Park, "'Influence of air-oxidation on electric double layer capacitances of multi-walled carbon nanotube electrodes," *Current applied physics*, vol. 10, no. 1, pp. 241-244.

[31] B. Kim, K. Cho and S. Park, "'Copper oxide-decorated porous carbons for carbon dioxide adsorption behaviors," *Journal of colloid and interface science*, vol. 342, no. 2, pp. 575-578.

[32] L. Meng and S. Park, "'MgO-templated porous carbons-based CO_2 adsorbents produced by KOH activation," *Materials chemistry and physics*, vol. 137, no. 1, Nov 15, pp. 91-96.

[33] M. Nandi, K. Okada, A. Dutta, A. Bhaumik, J. Maruyama, D. Derks and H. Uyama, "'Unprecedented CO_2 uptake over highly porous N-doped activated carbon monoliths prepared by physical activation," *Chemical communications (Cambridge, England)*, vol. 48, no. 83, Oct 25, pp. 10283-10285.

[34] B. Petrovic, M. Gorbounov and S. Masoudi Soltani, "'Influence of surface modification on selective CO_2 adsorption: A technical review on mechanisms and methods," *Microporous and mesoporous materials*, vol. 312, Jan.

[35] D. Lin, X. Zhang, X. Cui and W. Chen, "'Highly porous carbons with superior performance for CO_2 capture through hydrogen-bonding interactions," *RSC advances*, vol. 4, no. 52, pp. 27414.

[36] D.P. Bezerra, Silva, Francisco W. M. da, de Moura, Pedro A. S, K. Sapag, R.S. Vieira, E. Rodriguez-Castellon and D.C.S. de Azevedo, "'Adsorption of CO_2 on Amine-Grafted Activated Carbon," *Adsorption science & technology*, vol. 32, no. 2-3, Mar, pp. 141-151.

[37] H. Wang, X. Li, Z. Cui, Z. Fu, L. Yang, G. Liu and M. Li, "'Coffee grounds derived N enriched microporous activated carbons: Efficient adsorbent for post-combustion CO_2 capture and conversion," *Journal of colloid and interface science*, vol. 578, Oct 15, pp. 491-499.

[38] M. Sultana, M.H. Rownok, M. Sabrin, M.H. Rahaman and S.M.N. Alam, "'A review on experimental chemically modified activated carbon to enhance dye and heavy metals adsorption," *Cleaner Engineering and Technology*, vol. 6, Feb, pp. 100382.

[39] M. Sai Bhargava Reddy, D. Ponnamma, K.K. Sadasivuni, B. Kumar and A.M. Abdullah, "'Carbon dioxide adsorption based on porous materials," *RSC advances*, vol. 11, no. 21, Mar 31, pp. 12658-12681.

[40] A.W. Chester, "'Zeolite characterization and catalysis,", 2009.

[41] D. Barthomeuf, "'Framework induced basicity in zeolites," *Microporous and mesoporous materials*, vol. 66, no. 1, pp. 1-14.

[42] R.V. Siriwardane, M. Shen, E.P. Fisher and J. Losch, "'Adsorption of CO_2 on Zeolites at Moderate Temperatures," *Energy & fuels*, vol. 19, no. 3, May 18, pp. 1153-1159.

[43] Q. Wang, J. Luo, Z. Zhong and A. Borgna, "'CO_2 capture by solid adsorbents and their applications: current status and new trends," *Energy & environmental science*, vol. 4, no. 1, Dec 21, pp. 42-55.

[44] L. Hauchhum and P. Mahanta, "'Carbon dioxide adsorption on zeolites and activated carbon by pressure swing adsorption in a fixed bed," *Int J Energy Environ Eng*, vol. 5, no. 4, Aug 2, pp. 349-356.

[45] D. Ko, R. Siriwardane and L.T. Biegler, "'Optimization of Pressure Swing Adsorption and Fractionated Vacuum Pressure Swing Adsorption Processes for CO_2 Capture," *Industrial & engineering chemistry research*, vol. 44, no. 21, Oct 12, pp. 8084-8094.

[46] P. Xiao, J. Zhang, P. Webley, G. Li, R. Singh and R. Todd, "'Capture of CO_2 from flue gas streams with zeolite 13X by vacuum-pressure swing adsorption," *Adsorption*, vol. 14, no. 4-5, May 29, pp. 575-582.

[47] Z. Liang, M. Marshall and A.L. Chaffee, "'Comparison of Cu-BTC and zeolite 13X for adsorbent based CO_2 separation," *Energy Procedia*, vol. 1, no. 1, Feb, pp. 1265-1271.

[48] E. Díaz, E. Muñoz, A. Vega and S. Ordóñez, "'Enhancement of the CO_2 Retention Capacity of Y Zeolites by Na and Cs Treatments: Effect of Adsorption Temperature and Water Treatment," *Industrial & engineering chemistry research*, vol. 47, no. 2, Jan 16, pp. 412-418.

[49] N. Djeffal, M. Benbouzid, B. Boukoussa, H. Sekkiou and A. Bengueddach, "'CO_2 adsorption properties of ion-exchanged zeolite Y prepared from natural clays," *MRX*, vol. 4, no. 3, Mar 23,.

[50] L. Feng, Y. Shen, T. Wu, B. Liu, D. Zhang and Z. Tang, "'Adsorption equilibrium isotherms and thermodynamic analysis of CH_4, CO_2, CO, N_2 and H_2 on NaY Zeolite," *Adsorption*, vol. 26, no. 7, Feb 8, pp. 1101-1111.

[51] Y. Kamimura, M. Shimomura and A. Endo, "'CO_2 adsorption–desorption properties of zeolite beta prepared from OSDA-free synthesis," *Microporous and mesoporous materials*, vol. 219, Jan 1, pp. 125-133.

[52] Y. Wang, T. Du, Z. Qiu, Y. Song, S. Che and X. Fang, "'CO_2 adsorption on polyethylenimine-modified ZSM-5 zeolite synthesized from rice husk ash," *Materials chemistry and physics*, vol. 207, Mar 1, pp. 105-113.

[53] A. Kalantarifard, A. Ghavaminejad and G.S. Yang, "'High CO_2 adsorption on improved ZSM-5 zeolite porous structure modified with ethylenediamine and desorption characteristics with microwave," *J Mater Cycles Waste Manag*, vol. 19, no. 1, Sep 22, pp. 394-405.

[54] H.G.T. Nguyen, L. Espinal, R.D. van Zee, M. Thommes, B. Toman, M.S.L. Hudson, E. Mangano, S. Brandani, D.P. Broom, M.J. Benham, K. Cychosz, P. Bertier, F. Yang, B.M. Krooss, R.L. Siegelman, M. Hakuman, K. Nakai, A.D. Ebner, L. Erden, J.A. Ritter, A. Moran, O. Talu, Y. Huang, K.S. Walton, P. Billemont and G. De Weireld, "'A reference high-pressure CO_2 adsorption isotherm for ammonium ZSM-5 zeolite: results of an interlaboratory study," *Adsorption*, vol. 24, no. 6, Jul 26, pp. 531-539.

[55] T.D. Pham, M.R. Hudson, C.M. Brown and R.F. Lobo, "'Molecular Basis for the High CO_2 Adsorption Capacity of Chabazite Zeolites," *ChemSusChem*, vol. 7, no. 11, Nov, pp. 3031-3038.

[56] M. Miyamoto, Y. Fujioka and K. Yogo, "'Pure silica CHA type zeolite for CO_2 separation using pressure swing adsorption at high pressure," *Journal of materials chemistry*, vol. 22, no. 38, pp. 20186.

[57] R.H. Huesca, J.P. Arcos, D.V. Hernandez and M.A.P. Cruz, "'ADSORPTION KINETICS OF N_2O ON NATURAL ZEOLITES," *Revista internacional de contaminación ambiental*, vol. 32, no. 2, May 1, pp. 237-242.

[58] K.S. WALTON, M.B. ABNEY and M.D. LEVAN, "'CO_2 adsorption in Y and X zeolites modified by alkali metal cation exchange," *Microporous and mesoporous materials*, vol. 91, no. 1-3, pp. 78-84.

[59] E. Díaz, E. Muñoz, A. Vega and S. Ordóñez, "'Enhancement of the CO_2 Retention Capacity of Y Zeolites by Na and Cs Treatments: Effect of Adsorption Temperature and Water Treatment," *Industrial & engineering chemistry research*, vol. 47, no. 2, Jan 16, pp. 412-418.

[60] P.J.E. HARLICK and F.H. TEZEL, "'An experimental adsorbent screening study for CO_2 removal from N_2," *Microporous and mesoporous materials*, vol. 76, no. 1-3, pp. 71-79.

[61] M.R. Mello, D. Phanon, G.Q. Silveira, P.L. Llewellyn and C.M. Ronconi, "'Amine-modified MCM-41 mesoporous silica for carbon dioxide capture," *Microporous and mesoporous materials*, vol. 143, no. 1, pp. 174-179.

[62] J. Wu, X. Zhu, F. Yang, T. Ge and R. Wang, "'Easily-synthesized and low-cost amine-functionalized silica sol-coated structured adsorbents for CO_2 capture," *Chemical engineering journal (Lausanne, Switzerland : 1996)*, vol. 425, Dec 1, pp. 131409.

[63] E.S. Sanz-Pérez, M. Olivares-Marín, A. Arencibia, R. Sanz, G. Calleja and M.M. Maroto-Valer, "'CO_2 adsorption performance of amino-functionalized SBA-15 under post-combustion conditions," *International journal of greenhouse gas control*, vol. 17, Sep, pp. 366-375.

[64] D.V. Quang, A. Dindi, A.V. Rayer, N.E. Hadri, A. Abdulkadir and M.R.M. Abu-Zahra, "'Impregnation of Amines Onto Porous Precipitated Silica for CO_2 capture," *Energy Procedia*, vol. 63, pp. 2122-2128.

[65] Y. Liu, X. Lin, X. Wu, M. Liu, R. Shi and X. Yu, "'Pentaethylenehexamine loaded SBA-16 for CO_2 capture from simulated flue gas," *Powder technology*, vol. 318, Aug, pp. 186-192.

[66] N. Rao, M. Wang, Z. Shang, Y. Hou, G. Fan and J. Li, "'CO_2 Adsorption by Amine-Functionalized MCM-41: A Comparison between Impregnation and Grafting Modification Methods," *Energy & fuels*, vol. 32, no. 1, Jan 18, pp. 670-677.

[67] S. Loganathan, M. Tikmani and A.K. Ghoshal, "'Pore-expanded MCM-41 for CO_2 adsorption: Experimental and isotherm modeling studies," *Chemical engineering journal (Lausanne, Switzerland : 1996)*, vol. 280, Nov 15, pp. 9-17.

[68] M.G. Yıldız, T. Davran-Candan, M.E. Günay and R. Yıldırım, "'CO_2 capture over amine-functionalized MCM-41 and SBA-15: Exploratory analysis and decision tree classification of past data," *Journal of CO_2 utilization*, vol. 31, May, pp. 27-42.

[69] X. Wang, W. Zeng, H. Zhang, D. Li, H. Tian, X. Hu, Q. Wu, C. Xin, X. Cao and W. Liu, "'The dynamic CO_2 adsorption of polyethylene polyamine-loaded MCM-41 before and after methoxypolyethylene glycol codispersion," *RSC advances*, vol. 9, no. 46, Aug 28, pp. 27050-27059.

[70] S. Kim, J. Ida, V.V. Guliants and Y.S. Lin, "'Tailoring Pore Properties of MCM-48 Silica for Selective Adsorption of CO_2," *The journal of physical chemistry. B*, vol. 109, no. 13, Apr 7, pp. 6287-6293.

[71] A.R.D. Nascimento, G.P. Figueredo, T.R.D. Costa, M.A.F. Melo, D.M.A. Melo and M.J.B. Souza, "'Thermodynamics of CO_2 adsorption on mesoporous materials impregnated with nickel,", Dec 1,.

[72] E.S. Sanz-Pérez, M. Olivares-Marín, A. Arencibia, R. Sanz, G. Calleja and M.M. Maroto-Valer, "'CO_2 adsorption performance of amino-functionalized SBA-15 under post-combustion conditions," *International journal of greenhouse gas control*, vol. 17, Sep, pp. 366-375.

[73] N. Gargiulo, A. Peluso, P. Aprea, F. Pepe and D. Caputo, "'CO_2 Adsorption on Polyethylenimine-Functionalized SBA-15 Mesoporous Silica: Isotherms and Modeling," *Journal of chemical and engineering data*, vol. 59, no. 3, Mar 13, pp. 896-902.

[74] A. Zhao, A. Samanta, P. Sarkar and R. Gupta, "'Carbon Dioxide Adsorption on Amine-Impregnated Mesoporous SBA-15 Sorbents: Experimental and Kinetics Study," *Industrial & engineering chemistry research*, vol. 52, no. 19, May 15, pp. 6480-6491.

[75] F. Zheng, D.N. Tran, B.J. Busche, G.E. Fryxell, R.S. Addleman, T.S. Zemanian and C.L. Aardahl, "'Ethylenediamine-Modified SBA-15 as Regenerable CO_2 Sorbent," *Industrial & engineering chemistry research*, vol. 44, no. 9, Apr 27, pp. 3099-3105.

[76] H. Furukawa, K.E. Cordova, M. O'Keeffe and O.M. Yaghi, "'The Chemistry and Applications of Metal-Organic Frameworks," *Science*, vol. 341, no. 6149, Aug 30, pp. 974.

[77] H. FURUKAWA, N. KO, O.M. YAGHI, YONG BOK GO, N. ARATANI, SANG BEOM CHOI, E. CHOI, A. ÖZGÜR YAZAYDIN, R.Q. SNURR, M. O'KEEFFE and J. SKIM, "'Ultrahigh Porosity in Metal-Organic Frameworks," *Science (American Association for the Advancement of Science)*, vol. 329, no. 5990, Jul 7, pp. 424-428.

[78] K.C. Stylianou, J.E. Warren, S.Y. Chong, J. Rabone, J. Bacsa, D. Bradshaw and M.J. Rosseinsky, "'CO_2 selectivity of a 1D microporous adenine-based metal-organic framework synthesised in water," *Chemical communications (Cambridge, England)*, vol. 47, no. 12, Mar 28, pp. 3389-3391.

[79] J. An and N.L. Rosi, "'Tuning MOF CO_2 Adsorption Properties via Cation Exchange," *Journal of the American Chemical Society*, vol. 132, no. 16, Apr 28, pp. 5578-5579.

[80] J. An, S.J. Geib and N.L. Rosi, "'High and Selective CO_2 Uptake in a Cobalt Adeninate Metal−Organic Framework Exhibiting Pyrimidine- and Amino-Decorated Pores," *Journal of the American Chemical Society*, vol. 132, no. 1, Jan 13, pp. 38-39.

[81] A.R. Millward and O.M. Yaghi, "'Metal−Organic Frameworks with Exceptionally High Capacity for Storage of Carbon Dioxide at Room Temperature," *Journal of the American Chemical Society*, vol. 127, no. 51, Dec 28, pp. 17998-17999.

[82] Z. Zhao, Z. Li and Y.S. Lin, "'Adsorption and Diffusion of Carbon Dioxide on Metal−Organic Framework (MOF-5)," *Industrial & engineering chemistry research*, vol. 48, no. 22, Nov 18, pp. 10015-10020.

[83] B. Arstad, H. Fjellvåg, K.O. Kongshaug, O. Swang and R. Blom, "'Amine functionalised metal organic frameworks (MOFs) as adsorbents for carbon dioxide," *Adsorption*, vol. 14, no. 6, Jul 17, pp. 755-762.

[84] E. Stavitski, E.A. Pidko, S. Couck, T. Remy, E.J.M. Hensen, B.M. Weckhuysen, J. Denayer, J. Gascon and F. Kapteijn, "'Complexity behind CO_2 Capture on NH_2-MIL-53(Al)," *Langmuir*, vol. 27, no. 7, Apr 5, pp. 3970-3976.

[85] S. Couck, J.F.M. Denayer, G.V. Baron, T. Rémy, J. Gascon and F. Kapteijn, "'An Amine-Functionalized MIL-53 Metal−Organic Framework with Large Separation Power for CO_2 and CH_4," *Journal of the American Chemical Society*, vol. 131, no. 18, May 13, pp. 6326-6327.

[86] T.M. McDonald, D.M. D'Alessano, R. Krishna and J.R. Long, "'Enhanced carbon dioxide capture upon incorporation of N,N '-dimethylethylenediamine in the metal-organic framework CuBTTri," *Chemical science (Cambridge)*, vol. 2, no. 10, pp. 2022-2028.

[87] A. Demessence, D.M. D'Alessandro, M.L. Foo and J.R. Long, "'Strong CO_2 Binding in a Water-Stable, Triazolate-Bridged Metal−Organic Framework Functionalized with Ethylenediamine," *Journal of the American Chemical Society*, vol. 131, no. 25, Jul 1, pp. 8784-8786.

[88] A. Phan, C.J. Doonan, F.J. Uribe-Romo, C.B. Knobler, M. O'Keeffe and O.M. Yaghi, "'Synthesis, Structure, and Carbon Dioxide Capture Properties of Zeolitic Imidazolate Frameworks," *Accounts of chemical research*, vol. 43, no. 1, Jan 19, pp. 58-67.

[89] R. Banerjee, A. Phan, B. Wang, C. Knobler, H. Furukawa, M. O'Keeffe and O.M. Yaghi, "'High-Throughput Synthesis of Zeolitic Imidazolate Frameworks and Application to CO_2 Capture," *Science*, vol. 319, no. 5865, Feb 15, pp. 939-943.

[90] R. Banerjee, H. Furukawa, D. Britt, C. Knobler, M. O'Keeffe and O.M. Yaghi, "'Control of Pore Size and Functionality in Isoreticular Zeolitic Imidazolate Frameworks and their Carbon Dioxide Selective Capture Properties," *Journal of the American Chemical Society*, vol. 131, no. 11, Mar 25, pp. 3875-3877.

[91] H. Deng, C.J. Doonan, H. Furukawa, R.B. Ferreira, J. Towne, C.B. Knobler, B. Wang and O.M. Yaghi, "'Multiple Functional Groups of Varying Ratios in Metal-Organic Frameworks," *Science*, vol. 327, no. 5967, Feb 12, pp. 846-850.

[92] J.A. Mason, K. Sumida, Z.R. Herm, R. Krishna and J.R. Long, "'Evaluating metal-organic frameworks for post-combustion carbon dioxide capture via temperature swing adsorption," *Energy & environmental science*, vol. 4, no. 8, pp. 3030-3040.

[93] S. Chui, S. Lo, J. Charmant, A. Orpen and I. Williams, "'A chemically functionalizable nanoporous material," *Science (American Association for the Advancement of Science)*, vol. 283, no. 5405, Feb 19, pp. 1148-1150.

[94] S. Bordiga, L. Regli, F. Bonino, E. Groppo, C. Lamberti, B. Xiao, P.S. Wheatley, R.E. Morris and A. Zecchina, "'Adsorption properties of HKUST-1 toward hydrogen and other small molecules monitored by IR," *Physical Chemistry Chemical Physics*, vol. 9, no. 21, May 23, pp. 2676-2685.

[95] E.D. Bloch, D. Britt, C. Lee, C.J. Doonan, F.J. Uribe-Romo, H. Furukawa, J.R. Long and O.M. Yaghi, "'Metal Insertion in a Microporous Metal−Organic Framework Lined with 2,2′-Bipyridine," *Journal of the American Chemical Society*, vol. 132, no. 41, Oct 20, pp. 14382-14384.

[96] S. Dutta, "'A review on production, storage of hydrogen and its utilization as an energy resource," *Journal of industrial and engineering chemistry (Seoul, Korea)*, vol. 20, no. 4, Jul 25, pp. 1148-1156.

[97] D. Sahu, P. Mishra, S. Edubilli, A. Verma and S. Gumma, "'Hydrogen Adsorption on Zn-BDC, Cr-BDC, Ni-DABCO, and Mg-DOBDC Metal–Organic Frameworks," *Journal of chemical and engineering data*, vol. 58, no. 11, Nov 14, pp. 3096-3101.

[98] M. Anbia and S. Sheykhi, "'Preparation of multi-walled carbon nanotube incorporated MIL-53-Cu composite metal–organic framework with enhanced methane sorption," *Journal of industrial and engineering chemistry (Seoul, Korea)*, vol. 19, no. 5, Sep 25, pp. 1583-1586.

[99] Y. He, W. Zhou, T. Yildirim and B. Chen, "'A series of metal–organic frameworks with high methane uptake and an empirical equation for predicting methane storage capacity," *Energy & environmental science*, vol. 6, no. 9, Aug 1, pp. 2735-2744.

[100] X. Wu, Z. Bao, B. Yuan, J. Wang, Y. Sun, H. Luo and S. Deng, "'Microwave synthesis and characterization of MOF-74 (M=Ni, Mg) for gas separation," *Microporous and mesoporous materials*, vol. 180, Nov 1, pp. 114-122.

[101] M. Sai Bhargava Reddy, D. Ponnamma, K.K. Sadasivuni, B. Kumar and A.M. Abdullah, "'Carbon dioxide adsorption based on porous materials," *RSC advances*, vol. 11, no. 21, Mar 31, pp. 12658-12681.

[102] J. Wang, L. Huang, R. Yang, Z. Zhang, J. Wu, Y. Gao, Q. Wang, D. O'Hare and Z. Zhong, "'Recent advances in solid sorbents for CO_2 capture and new development trends,", vol. 7, no. 11, Oct 15, pp. 3478-3518.

[103] S.K. Das, P. Bhanja, S.K. Kundu, S. Mondal and A. Bhaumik, "'Role of Surface Phenolic-OH Groups in N-Rich Porous Organic Polymers for Enhancing the CO_2 Uptake and CO_2/N_2 Selectivity: Experimental and Computational Studies," *ACS applied materials & interfaces*, vol. 10, no. 28, Jul 18, pp. 23813-23824.

[104] M. Sai Bhargava Reddy, D. Ponnamma, K.K. Sadasivuni, B. Kumar and A.M. Abdullah, "'Carbon dioxide adsorption based on porous materials," *RSC advances*, vol. 11, no. 21, Mar 31, pp. 12658-12681.

[105] K.K. Han, Y. Zhou, Y. Chun and J.H. Zhu, "'Efficient MgO-based mesoporous CO_2 trapper and its performance at high temperature," *Journal of hazardous materials*, vol. 203-204, Feb 15, pp. 341-347.

[106] M. Liu, C. Vogt, A.L. Chaffee and S.L.Y. Chang, "'Nanoscale Structural Investigation of Cs2CO3-Doped MgO Sorbent for CO_2 Capture at Moderate Temperature," *Journal of physical chemistry. C*, vol. 117, no. 34, Aug 29, pp. 17514-17520.

[107] S. Lee and S. Park, "'A review on solid adsorbents for carbon dioxide capture," *Journal of industrial and engineering chemistry (Seoul, Korea)*, vol. 23, Mar 25, pp. 1-11.

[108] S. Lee and S. Park, "'A review on solid adsorbents for carbon dioxide capture," *Journal of industrial and engineering chemistry (Seoul, Korea)*, vol. 23, Mar 25, pp. 1-11.

[109] L.K.G. Bhatta, S. Subramanyam, M.D. Chengala, S. Olivera and K. Venkatesh, "'Progress in hydrotalcite like compounds and metal-based oxides for CO_2 capture: a review," *Journal of cleaner production*, vol. 103, Sep 15, pp. 171-196.

[110] J. White, "'Development of a Pressure Swing Adsorption (PSA) Cycle for CO_2 Capture From Flue Gas Using a 4-Bed PSA Apparatus,", Jan 1,.

[111] Anonymous "'What is Adsorption?".

[112] R.B. Bird, W.E. Stewart and E.N. Lightfoot, "'Transport phenomena,", 1960.

[113] Y. Park, Y. Ju, D. Park and C. Lee, "'Adsorption equilibria and kinetics of six pure gases on pelletized zeolite 13X up to 1.0 MPa: CO 2 , CO, N 2 , CH 4 , Ar and H 2," *Chemical engineering journal (Lausanne, Switzerland : 1996)*, vol. 292, May, pp. 348-365.

[114] E.J. Shokroo, D.J. Farsani, H.K. Meymandi and N. Yadollahi, "'Comparative study of zeolite 5A and zeolite 13X in air separation by pressure swing adsorption," *Korean J. Chem. Eng*, vol. 33, no. 4, Jan 30, pp. 1391-1401.

[115] S. Steven, "'fitAdsorptionIsotherm,".

[116] L.B.L. Lim, N. Priyantha, D.T.B. Tennakoon, H.I. Chieng, M.K. Dahri and M. Suklueng, "'Breadnut peel as a highly effective low-cost biosorbent for methylene blue: Equilibrium, thermodynamic and kinetic studies," *Arabian Journal of Chemistry*, vol. 10, no. S2, May, pp. S3216-S3228.

[117] S. CAVENATI, C.A. GRANDE and A.E. RODRIGUES, "'Separation of $CH_4/CO_2/N_2$ mixtures by layered pressure swing adsorption for upgrade of natural gas," *Chemical engineering science*, vol. 61, no. 12, pp. 3893-3906.

[118] J. Xiao, C. Li, L. Fang, P. Böwer, M. Wark, P. Bénard and R. Chahine, "'Machine learning–based optimization for hydrogen purification performance of layered bed pressure swing adsorption," *International journal of energy research*, vol. 44, no. 6, May, pp. 4475-4492.

[119] A. Berthelemot, R. Dubettier, V. Gueret and F. Lockwood, "'Adapting existing CO_2 capture technologies to the iron & steel industry,".

[120] Florens Kreuk, "'Optimization of CO_2 Capture using Chemical Solvents from Steel Mill's Works Arising Gases," *Delft University of Technology*, 31/10/.

[121] R. Ben-Mansour, M.A. Habib, O.E. Bamidele, M. Basha, N.A.A. Qasem, A. Peedikakkal, T. Laoui and M. Ali, "'Carbon capture by physical adsorption: Materials, experimental investigations and numerical modeling and simulations – A review," *Appl.Energy*, vol. 161, pp. 225-255.

[122] Y. Park, Y. Ju, D. Park and C. Lee, "'Adsorption equilibria and kinetics of six pure gases on pelletized zeolite 13X up to 1.0 MPa: CO 2 , CO, N 2 , CH 4 , Ar and H 2," *Chemical engineering journal (Lausanne, Switzerland : 1996)*, vol. 292, May, pp. 348-365.